VRIJE
UNIVERSITEIT
BRUSSEL

FACULTY OF ENGINEERING
Department of Toegepaste Natuurkunde
Brussels Photonic team

ROYAL MILITARY ACADEMY
Polytechnical Faculty
Department of Communication,
Information, Systems & Sensors

On the characterization of the photoelastic constant of glass and polymer optical fibers

Thesis submitted in fulfillment of the requirements for the award of the degree of Doctor in Engineering (Doctor in de ingenieurswetenschappen) by

Sophie Acheroy

March 2017

Promoters: Prof. dr. ir. Francis Berghmans (VUB)
Prof. dr. ir. Patrick Merken (RMA)
Prof. dr. ir. Heidi Ottevaere (VUB)

Members of the Jury

Prof. Dr. Ir. Steve VANLANDUIT, chairman
Department of Mechanics of Materials and Constructions,
Vrije Universiteit Brussel, Belgium

Prof. Dr. Ir. Roger VOUNCKX, vice-chairman
Department of Electronics and Informatics,
Vrije Universiteit Brussel, Belgium

Prof. Dr. Ir. Thomas GEERNAERT, secretary
Department of Applied Physics and Photonics,
Vrije Universiteit Brussel, Belgium

Prof. Dr. Ir. Francis BERGHMANS, promotor
Department of Applied Physics and Photonics,
Vrije Universiteit Brussel, Belgium

Prof. Dr. Ir. Heidi OTTEVAERE, co-promotor
Department of Applied Physics and Photonics,
Vrije Universiteit Brussel, Belgium

Prof. Dr. Ir. Patrick MERKEN, co-promotor
Department of Communication, Information, Systems & Sensors,
Royal Military Academy, Belgium

Prof. Dr. Ir Luc RABET
Department of Construction, Engineering & Materials,
Royal Military Academy, Belgium

Prof. Dr. David J. WEBB
Aston Institute of Photonic Technologies,
Aston University, United Kingdom

Dr. Ir Bram VAN HOE
FBGS International NV, Belgium

Summary

Optical fiber based sensors are rapidly gaining popularity. They offer an extensive list of advantages including immunity to electromagnetic interference, small size, low weight, high sensitivity, multiplexing capabilities, etc. and therefore they are increasingly applied in a large variety of industrial sectors. An important category of these sensors targets the measurement of mechanical quantities such as force, pressure and mechanical strain. These mechanical optical fiber sensors typically exploit the photoelastic effect to transduce a mechanical quantity into a measurable variation of the propagation characteristics of the light guided through the fiber. The photoelastic effect is governed by the stress-optic law, with the photoelastic constant as the material dependent parameter that links the applied mechanical stress to the change of refractive index in the material. Accurately predicting the response of optical fiber sensors to particular mechanical loads requires accurate knowledge of all the involved material parameters. In this PhD dissertation, we focus on the characterization of the photoelastic coefficient C of the optical fiber.

We aim to characterize C by carrying out measurements on the fiber itself, instead of relying on the value of C measured using bulk material samples, as this allows taking into account the influence of the fabrication process of the optical fibers on the value of the photoelastic constant. Furthermore, we dare to depart from the common hypothesis that C can be considered constant in the fiber cross-section and we therefore also aim to measure the value of C as a function of the radial position in the cross-section of an optical fiber.

Our approach to achieve these objectives is based on well-known photoelastic theory, and in particular on measuring the birefringence in a transversely illuminated optical fiber to which we have to apply a pre-defined axial tensile stress. This provides us with a projection of the stress-induced birefringence along the fiber diameter.

To do so we designed a setup to determine stress-induced retardance in an optical fiber using a polarizing microscope arrangement. The microscope allows achieving the spatial optical resolution of the order of 1 micrometer that is required to determine the profile of C across the fiber diameter, taking into account the typical dimensions of an optical fiber.

In order to recover the radial dependence of the photoelastic coefficient from the measured projected retardance, we have to use a mathematical transform known as the inverse Abel transform. To calculate this transform we have developed two algorithms relying on Fourier theory. We extensively tested the performance of both algorithms on a known analytical profile, which allowed us to identify the most adequate parameter set that returns the most reliable results. We also added noise to the analytical profile to mimic inevitable measurement noise, which allowed concluding on the robustness of our algorithms when dealing with noisy profiles.

To validate our approach, experimental setup and algorithms, we first carried out measurements of the radial profile of C of glass optical fibers with different core diameters and different doping profiles. We found values for the mean value of C in agreement with results reported in open literature. We demonstrated that the photoelastic coefficient of silica fibers differs from the photoelastic coefficient of bulk silica. We also evidenced that dopants used to modify the refractive index of glass fibers can influence the value of C and that making the assumption that C is constant across the fiber is not always valid.

Finally, we also applied our measurement method to characterize the photoelastic coefficient of polymer optical fibers (POFs), more specifically polymethyl methacrylate (PMMA) based optical fibers. We demonstrated that PMMA POFs drawn from different preforms display different profiles and different mean values of C. We therefore recommend measuring C for each different type of POF. In addition we showed that thermal annealing of the polymer fiber preform and of the fiber itself has a beneficial impact in view of stabilizing the value of C and of increasing the photoelastic response of the optical fiber.

We hope that this PhD research, and our work on characterizing the photoelastic properties of optical fibers in particular, will positively contribute to further developments in the fields of specialty optical fiber and optical fiber sensor design and applications.

Acknowledgements

I would like to thank my promotor Prof. Francis Berghmans who agreed to supervise my PhD research at the Fiber Sensing Group. My knowledge in optical fiber sensing technology grew continuously through our discussions and your scientific advice and support throughout the years.

The opportunity to perform my PhD research at the VUB, at the Fiber Sensing Group, was granted by my co-promotor Prof. Patrick Merken. Thank you Patrick for having built the necessary contacts allowing me to start a PhD research in cotutel with the VUB. You always encouraged me to give the best of myself for my research.

Without your supervision and our discussions, my PhD research would not have been a success. A warm thank to Prof. Heidi Ottevaere for your essential contributions, especially for the elaboration of the measurement methodology. I could always rely on your patience and knowledge to master the microscope and its manipulation at last.

I would like to thank Prof. Geernaert for his time and advice. You always helped me to interpret the measurement results with a critical and scientific mind. Our discussions were always fruitful and provided me with numerous of new ideas to explore further the challenges I was confronted with.

I would like to express my gratitude to the members of the jury that accepted to read and evaluate my work: Prof. Steve Vanlanduit, Prof. Roger Vounckx, Prof. Luc Rabet, Prof. David J. Webb, Dr. Bram Van Hoe.

I want to thank Prof. Webb and Dr. Carlos Marques from the Aston University of Birmingham for welcoming me in their facilities and providing me with polymer fiber samples. Thank you for sharing your expertise and for the helpful discussions.

I spent many hours and days in the cleanroom of the Photonics Innovation center in Gooik. I want to thank Dr Jurgen Van Erps and Dries Rosseel for their availability, help and nice discussions.

I was not often present in the campus of Etterbeek, but I appreciated the nice conversations and encouragements every time I was passing by.

Special thanks to Majorie Jammaers for your help in the organization of my private and public defense.

J'ai toujours pu compter sur l'aide logistique et technique des techniciens du Dept CISS de l'ERM, je pense particulièrement à Pascal De Kimpe et Fabian Filée. Un grand merci pour votre disponibilité, vos idées originales, vos contacts avec les autres départements et votre bonne humeur ! Je n'oublie pas mes collègues et amis du département, toujours là pour m'encourager, discuter des problèmes de programmation en Matlab que je rencontrais, rire un bon coup autour d'une tasse de café ou d'un spaghetti au Wappers.

J'ai également pu compter sur les amis, de Liège à Gand en passant par Bruxelles et ses environs, pour passer de bons moments de détente indispensables ! Merci à vous tous pour les repas agrémentés de discussions passionnantes, délirantes parfois et les soirées mémorables.

Un tout grand merci à ma famille pour leur présence et soutien permanent durant ces années de doctorat. Papa, maman, Isabelle et Cécile, j'ai toujours pu compter sur vos encouragements et vous étiez toujours présents pour me concocter de chouettes moments, en ce aidés par mes beaux-frères et les adorables Astrid et Charles. Je n'oublie pas mes beaux-parents, mon beau-frère Gaël et le petit Jul !

Fred, mon amour, tu as fait en sorte que ces années se passent dans les meilleures conditions pour nous quatre. Grâce à toi, je n'ai jamais perdu le contact avec 'la vraie vie' ! Merci pour ta patience, nous allons pouvoir concrétiser les nombreux petits et grands projets mis en attente ! Mes deux petits amours, Lise et Mathilde, vous avez été extraordinaires ! Très compréhensives et patientes, il est enfin là ce moment tant attendu ! A mon tour de vous faire plaisir et de réaliser certains de vos petits et grands rêves.

Sophie Acheroy

Brussels, 26 February 2017

Table of Contents

Chapter 1. General Introduction

1.1 Thesis rationale

In the early 1970's, Corning Glass Works created the first single mode glass fiber that was able to transmit light with an attenuation below 20 dB/km [1]. This development followed the pioneering work of Charles Kao, who demonstrated in the 1960s that the high optical loss in optical fibers at that time was due to impurities in the silica glass rather than from a problem with the technology itself. In 2009 Charles Kao received the Nobel Prize in Physics 'For groundbreaking achievements concerning the transmission of light in fibers for optical communications' [2, 3]. In the meantime, fused silica fiber fabrication technology continuously evolved yielding optical fibers with extremely low transmission loss in specific wavelength ranges, known as optical communication 'windows', as illustrated in Figure 1-1. Together with the advent and developments in the fields of lasers and semiconductor laser diodes, this enabled the development of long-haul optical communication systems[4, 5] .

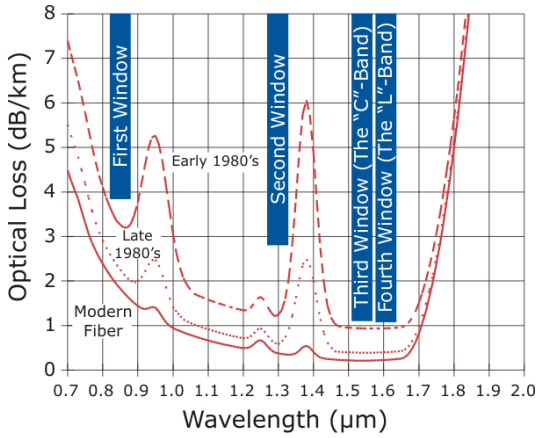

Figure 1-1: Illustration of the evolution of transmission loss in fused silica optical fibers and indication of typical optical communication windows [6].

Although glass optical fibers have always taken the largest share in fiber-optic based technology, plastic optical fibers (POFs) have initially been developed as specialty fibers for lower speed and shorter data links, as well as for illumination and lighting purposes [7]. In the 1970's and the early 1980's, several large-diameter multimode POFs have been developed. A major drawback was their extremely high attenuation (125dB/km). Typical base materials for the POFs included polymethyl methacrylate (PMMA), polycarbonate (PC) or polystyrene (PS). Continuous research and development efforts have also greatly increased the performance of these fibers. For example, the losses in perfluorinated POF are below 60 dB/km in the wavelength range of [800-1340 nm] [8]. Figure 1-2 compares the attenuation in PMMA, CYTOP™ [9] (an amorphous fluoropolymer) and glass fibers. Together with their ease of installation and lower cost, POFs have found their way into local area network, office network and home network connections.

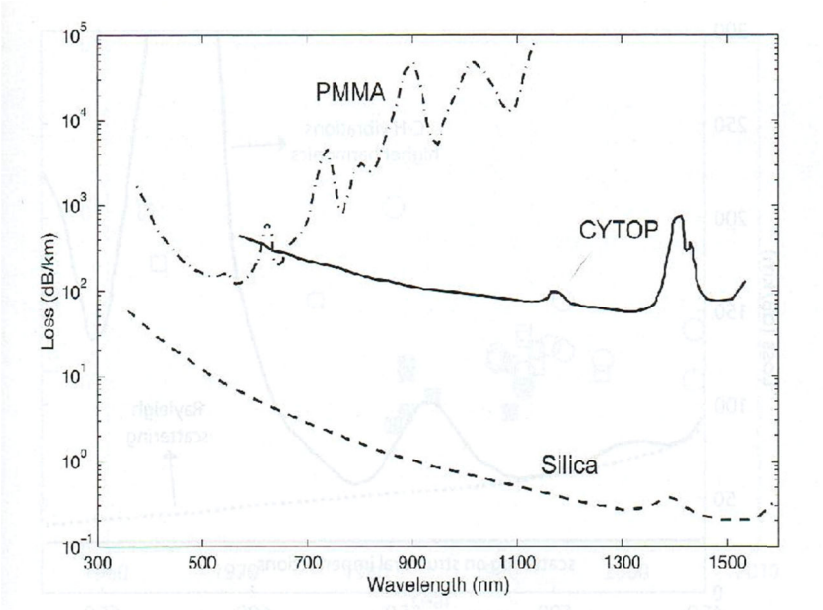

Figure 1-2: Comparison of the attenuation spectrum of PMMA optical fibers, CYTOP and silica fibers [10].

Besides optical communications, optical fiber technology has also largely penetrated other fields of applications owing to the development of dedicated devices based on such optical fibers. Two examples include optical fiber based lasers [11, 12], and optical fiber based sensors [13, 14]. Application domains as diverse as material processing, medicine and healthcare, safety and security, military and aerospace, structural health and asset monitoring, oil and gas, etc. have all welcomed optical fibers owing to the unique features that they convey to the devices and systems made thereof. Whilst telecom and broadband still took topmost positions in the fiber optics market with around 55% share by value in 2013, the fastest growth rate now also comes from applications addressing oil and gas, private data networks, and utilities [15]. A recent market study published in September 2016 projected the global fiber optic components market to exceed USD 23 billion by 2022 with key findings summarized in Figure 1-3 [16]. Two of these key findings also point to the growing demand in the field of fiber optic sensors and the growing use of specialty fiber.

Figure 1-3: Summary of key findings of the Global Fiber Optic Components Market.[16]

Owing to the expansion of possible application segments, the development of fiber optic fabrication technology has gone much further than the quest for obtaining the least attenuating silica fibers or POFs. Developing specialty fibers with characteristics adapted to specific applications has become a hot topic in research and innovation. In this PhD, we essentially target applications requiring optical fiber based sensors (OFS) and as for now, we will focus on this theme.

A fiber optic sensor relies on the principle that the light transmitted through the optical fiber experiences changes or a modulation of one of its properties, e.g. the intensity, phase, state of polarization or wavelength, due to the interaction with a physical quantity that acts either directly on the optical fiber, or on another transducer element connected with the fiber. By relating the magnitude of the modulation to the magnitude of the physical quantity, one can measure or 'sense' said quantity. Optical fiber based sensors can typically be classified as follows. :

1. Intensity or amplitude sensor
   In this type of OFS, the intensity of the optical radiation guided in the optical fiber is modulated by the physical quantity to be measured, i.e. by the so-called 'measurand'. Optical intensity changes are easily detected with a photodetector and such sensors are mostly technically simple and potentially low cost [17]. An intensity based optical fiber sensor can, for example, rely on the principle of 'micro-bending' (Figure 1-4). Microbends cause light to leak out from the fiber and hence the intensity of the guided light will depend on the amplitude of the microbends. The latter can be induced by a transducer acting on the fiber, that is actuated in its turn by measurands such as displacements, force, pressure, strain, vibration or even temperature [18].

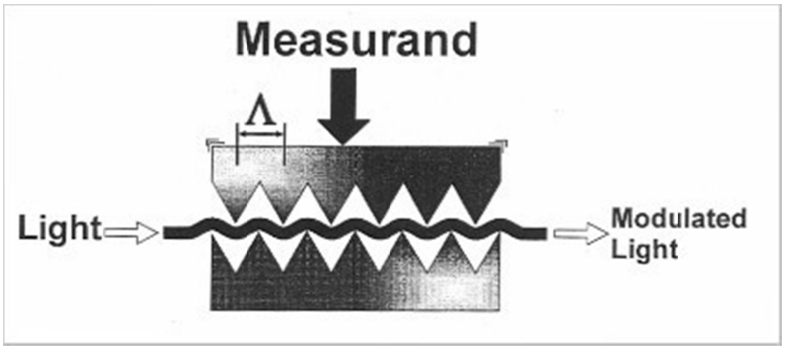

Figure 1-4: Illustration of the principle of a microbend-based optical fiber intensity sensor [19]

2. Phase or interferometric sensor
   The sensing principle relies on the modulation of the phase of an optical carrier. The phase change can be measured by comparing it to the phase of a reference signal in an interferometric setup. A well-known and successful application of this principle is the Interferometric Fiber Optic Gyroscope (I-FOG)[20]. In an I-FOG the phase change results from the Sagnac effect [21], which produces a phase change $\Delta\varphi$ between two optical waves propagating in opposite directions through a coiled optical fiber, that is proportional to the rotation rate Ω of the optical fiber coil. The basic scheme of the I-FOG is illustrated in Figure 1-5. I-FOGs are popular instruments in high quality inertial navigation systems [22, 23].

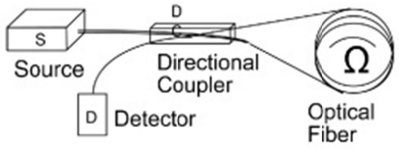

Figure 1-5: Illustration of basic scheme of the interferometric fiber optic gyroscope [20]. Ω is the rotation rate of the fiber coil.

3. Polarimetric sensor
   In this type of sensor, the state of polarization of the light travelling through the fiber is affected by the measurand. The specialty fibers used for such OFS are typically so-called highly birefringent single mode fibers, which guide two orthogonal linear polarization states of the fundamental mode. These two states are characterized by two different propagation constants and hence by two different refractive indices. The difference between these two indices is called the 'birefringence' of the optical fiber. The birefringence of the highly birefringent fiber and thus the polarization of the guided light can be very sensitive to external influences such as temperature, axial and transverse mechanical stress, hydrostatic pressure, etc [14, 24].

Such sensors have been proposed, for example, to measure dynamic strain in composite material and to locate cracks in engineering structures in order to support structural health monitoring applications. They are also used for electric and magnetic measurement based on the Faraday effect [25, 26].

4. Wavelength based sensor
   In a wavelength based OFS one relies on the measurement of the wavelength of light guided by the optical fiber. Since the measurand is encoded in the wavelength instead of the intensity of the optical signal, these sensors do not suffer from spurious effects such as optical source intensity variations or phase jumps. To modulate the wavelength one typically relies on a transducing element fabricated within the optical fiber itself, which acts as a wavelength selective mirror or filter. Examples of such structures include Fabry-Perot cavities [27] or fiber Bragg gratings (FBGs) [28]. A fiber Bragg Grating is a periodic modulation of the refractive index in the core of the optical fiber that is fabricated with laser-based inscription techniques. Such a structure has the property to reflect only a narrow band of wavelengths centered around the so-called resonance or Bragg wavelength. The latter shifts when the grating experiences external perturbations such as temperature changes and strain. This shift is mostly proportional to the magnitude of the perturbation [28] and can be straightforwardly detected using a spectroscopic device.

The four categories of optical sensors enumerated above are typically used as ‘point sensors’, i.e. they allow evaluating the measurand at one specific location [29].

Optical fibers can also be used as ‘distributed sensors’, which allow quantifying a measurand as a function of the position along the fiber length. Such sensors typically rely on detecting the amount of light that is scattered at each position along the fiber by means of different phenomena such as Raman or Brillouin scattering [29].

The versatility and unique features of optical fiber based sensors makes them very attractive for many applications. Their extensive list of advantages includes immunity to electromagnetic interference, small size,

light weight, high sensitivity, suitability for mass production, robustness and long term stability, multiplexing capabilities, etc. [4, 30–32]. This caused the field of optical fiber sensors to experience tremendous growth over the last two decades, and this trend is likely to continue in the years to come, as indicated by various market studies. This is illustrated in Figure 1-6, which gives a market forecast by Global Market Insights for fiber optic sensors up to 2024 and which predicts a compound annual growth rate of 7.5% from 2016 to 2024 for this market [33]. Both continuous distributed systems and point sensors will experience continuous growth in the coming years.

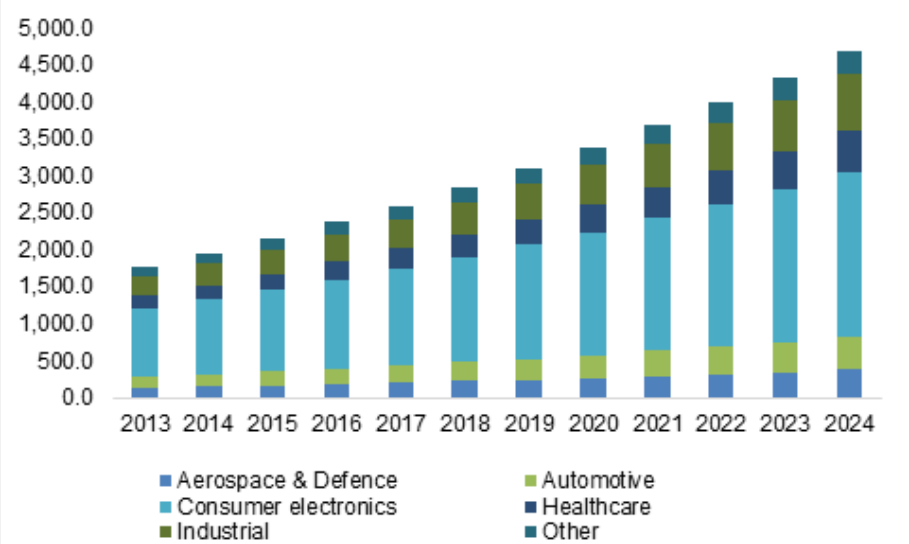

Figure 1-6: Fiber optic sensor market forecast towards 2024. The vertical axis is expressed in Million US Dollars [33].

Besides temperature sensors, so-called mechanical or dynamometric optical fiber sensors cover a major part of this market. These sensors are applied to measure mechanical quantities such as force, mechanical strain, mechanical stress or pressure. Accurate knowledge of these measurands is crucial in many applications. They have to be monitored, for example, for

steering a multitude of industrial processes or for following up on the health of civil engineering structures (bridges, dams, tunnels, aircrafts, …). All of these physical quantities can be measured by the four different OFS types described earlier in this section, i.e. intensity-based sensors, interferometric sensors, polarimetric sensors and wavelength-based sensors [28, 32, 34–36]. **The transduction mechanism that is mostly exploited to enable such a measurement with either one of these sensor types builds on photoelasticity, and this is where we enter the core of this PhD research.**

Photoelasticity allows relating the change in the properties of an optical signal transmitted through a transparent material with the magnitude of the mechanical load applied to said material. It is a well-known experimental technique that has been used for many years to study stress and strain distributions in a material [37] and that relies on the analysis of stress-induced birefringence in a material at wavelengths for which it is transparent. Developing an optical fiber sensor dedicated to the measurement of mechanical quantities and relying on the photoelastic effect requires a good understanding of how mechanical loads influence the material properties of the optical fiber. Before an optical fiber sensor is actually tested and produced, the particular fiber sensor structure has to be optimized using specialty design and simulation tools, for example finite element modelling. Effective use of the latter usually requires accurate knowledge of the fiber material parameters. For mechanical sensor simulation purposes for instance, the knowledge of the Young Modulus E, Poisson coefficient ν, the glass transition temperature T_G and the stress-optic coefficients C_1 and C_2 are required to achieve reliable and precise simulation results [38–42]. The stress-optic coefficients C_1 and C_2 (expressed in Pa^{-1}) and the photoelastic coefficient $C = C_1\text{-}C_2$ define the photoelastic properties of the material and play a crucial role in understanding and predicting the response of an optical fiber to mechanical load, since these parameters link the applied stress to the change of the refractive index in the fiber [43]. **This PhD work focuses on the photoelastic coefficient C of optical fibers.**

Reading the literature on this subject reveals that this material parameter is well-known for bulk silica or polymer material. However, the fabrication process of the optical fibers, typically involving drawing at elevated temperatures as we will discuss further in Chapter 3, can have an

impact on the value of this parameter. **We conclude that there is missing information and knowledge about the value of the photoelastic constant in the optical fibers themselves.**

This brings us to the grand objective of our PhD research. We aim **to characterize the photoelastic coefficient of optical fibers with sufficient accuracy by carrying out measurements directly on the optical fiber itself instead of on bulk material from which the fiber is made, and to investigate whether the value of this photoelastic coefficient can be considered constant in the cross-section of the optical fiber, or not.**

1.2 Thesis objectives and strategy

As stated above, our grand objective is to develop a method to characterize the photoelastic coefficient C by means of measurements on actual optical fiber samples, in such a way that we can also obtain the profile of C in the cross-section of the optical fiber. To do so we have to build on the principles of photoelasticity, which involve C as the material parameter that links the change of the refractive index in the material, and more specifically of the birefringence in the material, to externally applied mechanical stress. Achieving this objective requires addressing the following challenges.

We first need **to build an adequate experimental setup**. To do so our approach is to look first into methods that have been proposed to measure C on bulk material and to investigate how such methods can be adapted to measure C directly in optical fiber samples. Considering that we also want to retrieve the profile of C across the fiber and that silica optical fibers have a typical outer diameter of 125 μm, and a core size that can be a few microns only, we should obtain **a spatial resolution of the order of 1 μm**. This essentially implies that our experimental setup should be suitable for integration in a microscope architecture.

The required ability to carry out the measurements on a fiber portion submitted to a predefined and well-controlled mechanical load that is uniform across its section does not allow carrying out such measurements on a fiber tip. We have to rely instead on a transverse illumination of the fiber to retrieve the birefringence for a particular mechanical load. Considering the cylindrical shape and the axial symmetry of an optical fiber,

a birefringence measurement with transverse illumination results in an actual projection of that birefringence on a plane. The projected function that we obtain should allow us to calculate the radial profile of C. Mathematics enables us to do so by means of an inverse integral transform, known as the 'inverse Abel transform', which allows determining the radial distribution of an axi-symmetric function from a projection of that function. This brings us to the second challenge, which is **to develop an adequate algorithm to calculate the inverse integral with sufficient accuracy, such that C can be determined within a standard deviation of 10% from the mean value**. This should be sufficient to produce radial profiles of the photoelastic coefficient and to draw correct conclusions when interpreting the final measurement results. The calculation should also be sufficiently robust to deal with inevitable measurement noise resulting from imperfections and limitations of the measurement setup and procedure.

The third and final challenge is then **to validate our method based on measurements on actual optical fibers**. We can do so first by comparing the values for C that we obtain with results obtained for either bulk material or optical fibers, as published in open literature. We can also do this by relating the obtained cross-sectional profile of C to our a-priori knowledge about the structure of the optical fiber and about the materials from which it is made. In this respect, an additional challenge is **to extend our method from measurements on conventional silica optical fibers to specialty polymer optical fibers** and to highlight the differences between both types of fibers in the context of potential optical fiber sensor applications.

1.3 Structure of the dissertation

The dissertation addresses the different challenges highlighted above one by one, and is structured as follows. In Chapter 2 we first give an overview of the laws and mechanisms that govern photoelasticity. We focus on the photoelastic law and on the concept of birefringence in a material. We then briefly explain how birefringence in an optical fiber can be exploited to obtain mechanical sensors. We highlight the importance of the accurate knowledge of the photoelastic constant in specialty optical fiber sensors and the impact of an uncertainty on the value of the photoelastic constant on the predicted response of the optical fiber sensor.

Chapter 3 starts with a summary of the information found in open literature on measurement methods that have been applied to determine the photoelastic coefficient in bulk material. We also describe the methods proposed to measure C directly on the fibers. We then explain the manufacturing process of both silica and polymer fibers to illustrate the need to develop an accurate measurement method to determine the photoelastic coefficient and its radial dependence across the fiber cross-section. We end this Chapter with specifying the different challenges we face when attempting to measure the radial profile of the photoelastic coefficient.

Chapter 4 first describes the theoretical basis of our approach and then turns to the explanation of our measurement setup arranged in a polarizing microscope architecture, which allows measuring the retardance of a laterally illuminated fiber to which we apply tensile stress. We also explain the algorithms that we propose to compute the inverse Abel transform of the measured retardance.

Chapter 5 evaluates the inverse Abel transform algorithms and analyses the influence of measurement noise on the results. To do so, we start from a pre-defined semi-elliptical shape of the projected retardance $R(y)$. We first compare the numerical results of the inverse Abel transform of the semi-ellipse with the analytical expression of the inverse Abel transform of the same semi-ellipse. We also study the impact on the result when we add noise to the semi-ellipse to mimic measurement noise. Doing so we obtain the optimal set of parameters that returns the most effective numerical inverse transform.

In Chapter 6 we discuss our results on the radial profile of the photoelastic coefficient in actual silica fibers. We describe the mechanical system that we built to apply tensile stress to a fiber sample while placed in the microscope arrangement. We explain in detail how we determine the retardance profile in one fiber section. We then first determine the mean value of the photoelastic coefficient by approximating the retardance with a semi-elliptical profile. Finally, we compute the radial profile $C(r)$ without any simplifying hypothesis and we compare our results to data that has been reported in open literature.

In Chapter 7 we measure the photoelastic coefficient in polymer fibers. We first recall the unique features of polymer fibers when considering

potential sensing applications. We also discuss thermal annealing treatments of such fibers, as they appear to have a major influence on our measurement results. We then determine and discuss the mean value of the photoelastic coefficient using the semi-elliptical approximation and the radial profile of C without simplifying assumption for a set of pristine and annealed fiber samples.

In the concluding Chapter, we review our main achievements and their importance in the context of the design of tailored mechanical fiber sensors. We also discuss our views about possible future investigations on the photoelastic coefficient of optical fibers.

Bibliography

[1] K. Gerd, *Optical Fiber Communication*. Mc Graw-Hill Education,. 2014.

[2] N. Chinlon Lin, "From G. Marconi to Charles K. Kao: Photonics R and D and the global broadband transformation in the 21st century," in *15th OptoElectronics and Communications Conference*, 2010.

[3] "Nobel Prizes and Laureates." [Online]. Available: https://www.nobelprize.org/nobel_prizes/physics/laureates/2009/.

[4] Z. Guo, Ed., *Progress in optical fibers research*. Nova Science Publishers, Inc, 2007.

[5] S. D. Personick, *Fiber Optics: Technology and Applications*. Media, Springer Science & Business, 2013.

[6] "A brief history of optical fiber." [Online]. Available: http://www.olson-technology.com/mr_fiber/fiber-history.htm.

[7] W. Schnabel, *Polymers and Light: Fundamentals and Technical Applications*. Wiley-VCH, 2007.

[8] M. G. Kuzyk, *Polymer fiber optics: materials, physics, and applications*. CRC Press, 2006.

[9] "CYTOP." [Online]. Available: http://www.agc-chemicals.com/jp/en/fluorine/products/detail/index.html?pCode=JP-EN-F019.

[10] J. Zubia and J. Arrue, "Plastic Optical Fibers: An Introduction to Their Technological Processes and Applications," *Opt. Fiber Technol.*, vol. 7, no. 2, pp. 101–140, 2001.

[11] J. C. Knight, "Photonic crystal fibers and fiber lasers (Invited)," *J. Opt. Soc. Am. B*, vol. 24, no. 8, p. 1661, 2007.

[12] V. Ter-Mikirtychev, "Fundamentals of fiber lasers and fiber amplifiers," *Springer Series in Optical Sciences*, vol. 181. pp. 1–253, 2014.

[13] L. Byoungho, "Review of the present status of optical fiber sensors," *Sci. - Opt. Fiber Technol.*, vol. 9, no. 2, pp. 57–79, 2003.

[14] S. Yin, P. B. Ruffin, and F. T. S. Yu, *Fiber optic sensors*. CRC Press, 2008.

[15] "http://www.dkphotonics.com/blog/fiber-optic-sensors-global-

market-forecast-dk-photonics/." .

[16] "Increase in Fiber Optic Network Deployments to Drive Growth of the Global Fiber Optic Components Market." [Online]. Available: http://www.strategyr.com/MarketResearch/Fiber_Optic_Components_Market_Trends.asp.

[17] J. M. López-Higuera, Ed., *Optical sensors*. Servicio de Publicaciones de la Universidad de Cantabria, 1998.

[18] J. L. Santos and F. Fahari, *Handbook of Optical Sensors*. CRC Press, 2014.

[19] "Periodical microbenders." [Online]. Available: http://www.optique-ingenieur.org/en/courses/OPI_ang_M06_C04/co/Contenu.html.

[20] J. Nayak, "Fiber-optic gyroscopes: from design to production," *Applied Optics*, vol. 50, no. 25. p. E152, 2011.

[21] B. Culshaw, "The optical fibre Sagnac interferometer: an overview of its principles and applications," *Meas. Sci. Technol.*, vol. 17, no. 1, pp. R1–R16, 2006.

[22] H. C. Lefèvre, "Fundamentals of the interferometric fiber-optic gyroscope," *Opt. Rev.*, vol. 4, no. 1, pp. A20–A27, 1997.

[23] H. C. Lefevre, "Ultimate-performance fiber-optic gyroscope: A reality," *16th Opto-Electronics Commun. Conf.*, pp. 75–78, 2011.

[24] A. . Domanski, T. R. Wolinski, and W. J. Bock, "Polarimetric fiber optic sensors: state of the art and future," in *SPIE 2341, Interferometry*, 1994.

[25] F. Briffod, L. Theavnaz, P.-A. Nicati, A. Kueng, and P. Robert, "Polarimetric Current Sensor Using an In-Line Faraday Rotator," *IEICE Trans. Electron.*, vol. E83–C, no. 3, pp. 331–335, 2000.

[26] M. Belal, Z. Song, Y. Jung, G. Brambilla, and T. P. Newson, "Optical fiber microwire current sensor.," *Opt. Lett.*, vol. 35, no. 18, pp. 3045–3047, 2010.

[27] T. Steinmetz, Y. Colombe, D. Hunger, T. W. Hänsch, A. Balocchi, R. J. Warburton, and J. Reichel, "Stable fiber-based Fabry-Pérot cavity," *Appl. Phys. Lett.*, vol. 89, no. 11, p. 111110, 2006.

[28] A. Othonos and K. Kalli, *Fiber Bragg gratings: fundamentals and applications in telecommunications and sensing*. Artech House, INC, 1999.

[29] F. Berghmans and T. Geernaert, “Optical fiber point sensors,” in *Advanced Fiber Optics: Concepts and Technology*, L. Thévenaz, Ed. EPFL Press, 2011.

[30] J. Hecht, *Understanding fiber optic*. Prentice Hall, 2005.

[31] K. Peters, “Polymer optical fiber sensors—a review,” *Smart Mater. Struct.*, vol. 20, no. 1, p. 13002, 2011.

[32] F. Berghmans and H. Thienpont, “Plastic Optical Fibers for Sensing Applications,” *OFC*, pp. 3–5, 2014.

[33] “Optical Sensors Market Size by product.” [Online]. Available: https://www.gminsights.com/industry-analysis/optical-sensor-market.

[34] T. Geernaert, G. Luyckx, and E. Voet, “Transversal load sensing with fiber Bragg gratings in microstructured optical fibers,” *IEEE PHOTONICS Technol. Lett.*, vol. 21, no. 1, 2009.

[35] A. D. Kersey and M. A. Davis, “Fiber grating sensors,” *J. Light. Technol.*, vol. 15, no. 8, pp. 1442–1463, 1997.

[36] K. Peeters, “Polymer optical fibre sensors - A review,” *Smart Mater. Struct.*, vol. 20, no. 13002, 2011.

[37] J. Doyle and J. Phillips, “Manual on experimental stress analysis,” *Soc. Exp.*, 1989.

[38] T. Geernaert and T. Nasilowski, “Fiber Bragg gratings in germanium-doped highly birefringent microstructured optical fibers,” *IEEE Photonics Technol. Lett.*, vol. 20, no. 8, pp. 554–556, 2008.

[39] U. W. Martynkien T., “Modeling of spectral characteristics of Corning PMF-38 highly birefringent fiber,” *Opt.*, vol. 113, no. 1, pp. 25–30, 2002.

[40] T. Martynkien, G. Wojcik, P. Mergo, and W. Urbanczyk, “Highly birefringent polymer side-hole fiber for hydrostatic pressure sensing,” vol. 40, no. 13, pp. 3033–3036, 2015.

[41] S. Sulejmani, “Microstructured optical fiber Bragg grating-based sensors for shear strain measurements,” PhD dissertation, Vrije Universiteit Brussel, 2015.

[42] F. Berghmans, T. Geernaert, M. Napierała, T. Baghdasaryan, C. Sonnenfeld, S. Sulejmani, T. Nasiłowski, P. Mergo, T. Martynkien, W. Urbańczyk, E. Bereś-Pawlik, and H. Thienpont, “Applying optical design

methods to the development of application specific photonic crystal fibres," in *Optical Systems Design 2012*, vol. 8550, 2012.

[43] L. N. Glass Stress Summer School, Tallinn, "Photoelasticity of glass."

Chapter 2. The photoelastic constant and its importance in fiber optics

Photoelasticity is a basic concept that underpins the principle of operation and the transduction mechanism in many mechanical or dynamometric optical fiber based sensors. We therefore start with an overview of the basic principles of photoelasticity in section 2.1. We define the elasticity of a material and we recall the polarization properties of a light wave. We proceed with the presentation of the stress-optic law, which governs the interaction of polarized light with a transparent material. We end this section with the definition of birefringence of a material and the associated relative retardance. In section 2.2, we introduce the notion of birefringence in a classical optical fiber and in highly birefringent fibers or polarization maintaining fibers (PMF). In section 2.3, we give an overview of the sensing mechanism of a PMF based polarimetric sensor and the sensing mechanism associated with a fiber Bragg grating (FBG) based optical fiber sensor (OFS). Such a FBG is a very popular and commercially available sensor device that is commonly used to measure mechanical quantities such as strain, stress and pressure. It is therefore a good illustration that serves our purpose for introducing various sources of birefringence in optical fibers that can impact the operation as mechanical sensor. We also introduce such sensors fabricated in highly birefringent fibers, polarization maintaining fibers and microstructured optical fibers (MOF). The study of these sensors allows highlighting the importance of the accurate knowledge of the photoelastic constant C of the optical fiber. In the last part of this section, we analyze the influence of birefringence on the spectral response of the FBG based OFS and we illustrate the principle with a simulated example. Section 2.4 analyses the impact of an erroneous value of the photoelastic constant on the spectral sensitivity of the sensor subjected to a line load. We end Chapter two with a brief illustration of the importance of C to perform quality prediction in telecommunication applications.

2.1 General principles of photo-elasticity

Photoelasticity can be defined, in general terms, as an analysis of the interaction of a lightwave with a material that experiences a mechanical stress or strain distribution [1, 2]. It reveals that non-crystalline materials that are optically isotropic in absence of any mechanical stress distribution can become optically anisotropic and therefore birefringent when experiencing such stress distribution. Photoelasticity can therefore be used to study the stress distribution in a material by investigating the birefringence properties at wavelengths for which the material is transparent. The mechanical stress can be either residual, i.e. an intrinsic tension or compression in the material that exists without any external load being applied and that can result from the fabrication process of said material, or can result from the application of an external load to the material. A major result of photoelasticity is that the amount of induced birefringence appears to be proportional to the amount of mechanical stress. We develop the concepts pertaining to photoelasticity further in the subsections below, whilst focusing only on those definitions that are important in view of understanding the remaining Chapters of this dissertation.

2.1.1 Elasticity

Elasticity refers to the property of a material to deform when subjected to an external force such that the deformation disappears with the removal of the force and the material returns to its original shape and size [1].

The stress σ due to a resultant internal force δF acting on an elementary area δA is defined as $\sigma = \lim_{\delta A \to 0} \frac{\delta F}{\delta A}$ [3]. The components of stress normal to the area and in the plane of the area are defined as the normal stress components σ and the shear stress components τ, respectively. In an orthogonal axis system x,y and z, there are 3 normal stress components σ_x, σ_y, σ_z and 6 values of shear stress τ_{xy}, τ_{yx}, τ_{xz}, τ_{zx}, τ_{yz}, τ_{zy} with:

$$\tau_{xy} = \tau_{yx}$$
$$\tau_{xz} = \tau_{zx} \quad (2.1)$$
$$\tau_{yz} = \tau_{zy}$$

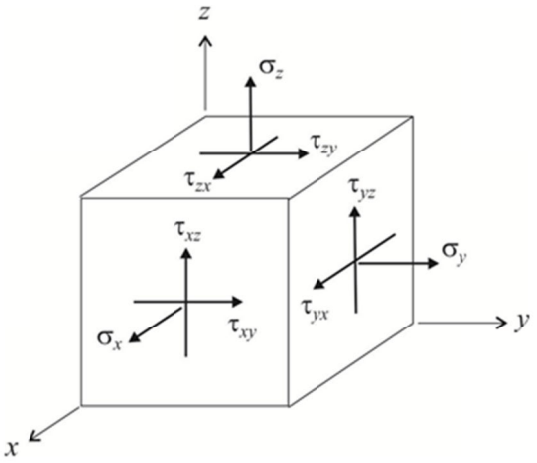

Figure 2-1: Representation of the three-dimensional normal and shear stress components in a Cartesian coordinate system [4].

The stress components are illustrated in Figure 2-1. These six independent components are required to define a three dimensional state of stress [1].

If all stresses lie in one plane, the body is said to be in a state of plane stress or in a two dimensional state of stress. For example, if we assume all stresses to lie in the xy-plane we have $\sigma_z = \tau_{xz} = \tau_{yz} = 0$, i.e. the normal stress and the shear stresses with a component along the z-axis are zero. A plane stress state is therefore defined by three independent stresses σ_x, σ_y and τ_{xy}.

In a plane state of stress, one can therefore always find an angle θ from the orthogonal axis system that defines the principal directions where the

only stresses present are normal stresses. These stress components σ_1 and σ_2 are called the principal stresses and are mutually perpendicular. They correspond to the maximum and minimum normal stresses in the two dimensional plane. Equation (2.2) gives the relation between the principal stresses and the stress components σ_x and σ_y.

$$\sigma_1, \sigma_2 = \frac{\sigma_x + \sigma_y}{2} \pm \sqrt{\left(\frac{\sigma_x - \sigma_y}{2}\right)^2 + \tau_{xy}^2} \tag{2.2}$$

The principal angle θ is given by: $\tan 2\theta = \frac{2\tau_{xy}}{\sigma_x - \sigma_y}$

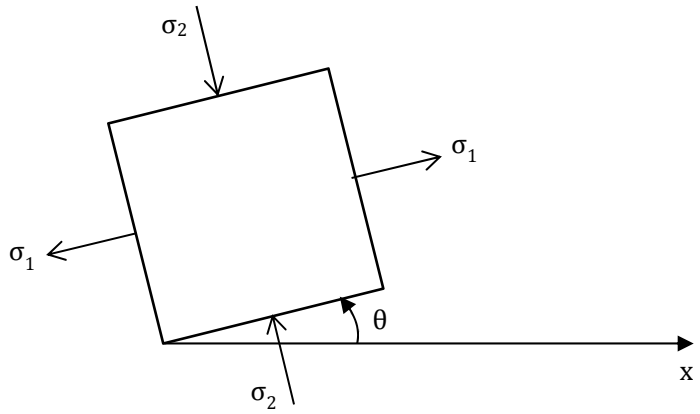

Figure 2-2: Principal stresses on an infinitesimal rectangular element under plane stress conditions. θ defines the direction of the principal stress.

The principal stresses and angle θ are illustrated in Figure 2-2. If σ_x and σ_y correspond with the principal stresses σ_1 and σ_2, we have $\tau_{xy} = 0$.

2.1.2 Polarization properties of light

Light is an electromagnetic (EM) wave. The electrical field vector $\overline{E}$ associated with the light wave vibrates perpendicularly to the propagation direction. When the wave is constrained to vibrate in a systematic manner in the plane perpendicular to the direction of propagation, the light wave is said to be polarized. Let us consider the components of the electrical field vector associated to a monochromatic polarized plane wave propagating along the z direction in a Cartesian system of axes x, y, z which can be written as given in equation (2.3).

$$\begin{aligned} E_x &= E_{0x}\cos(\omega t - kz + \Delta) \\ E_y &= E_{0y}\cos(\omega t - kz) \end{aligned} \tag{2.3}$$

with E_{0x} and E_{0y} the amplitude of the x and y components of $\overline{E}$, $k = 2\pi/\lambda$ the wavenumber and ω the angular frequency. The time is measured from the instant that the component E_y crosses the x-axis, the initial phase of this component is zero and the corresponding phase of E_x at that time is Δ. Eliminating $(\omega t - kz)$ from equation (2.3) yields equation (2.4). The latter is the equation of an ellipse drawn in the plane perpendicular to the direction of propagation by the electrical field vector. The pattern drawn by the evolution in time of the electric field vector in this plane allows distinguishing between different states of polarization (SOP).

$$\frac{E_x^2}{E_{0x}^2} + \frac{E_y^2}{E_{0y}^2} - 2\frac{E_x E_y}{E_{0x}E_{0y}}\cos\Delta = \sin^2\Delta \tag{2.4}$$

From equation (2.4) one realizes indeed that the SOP of a polarized wave is described by two parameters:

- The ratio $\frac{E_{0y}}{E_{0x}}$;
- The phase difference Δ between the two components of $\overline{E}$.

We can identify two particular states of polarization:

- The *linear polarization* state, i.e. $\Delta = \pm(l \times \pi)$;

- The *circular polarization state*, i.e. when $E_{0x} = E_{0y}$ and $\Delta = \pm(2l+1) \times \frac{\pi}{2}$.

The parameter l is a positive integer. Any polarized state in between these two cases is referred to as *elliptical polarization state*. Figure 2-3 illustrates the linear, circular and elliptical state of polarization.

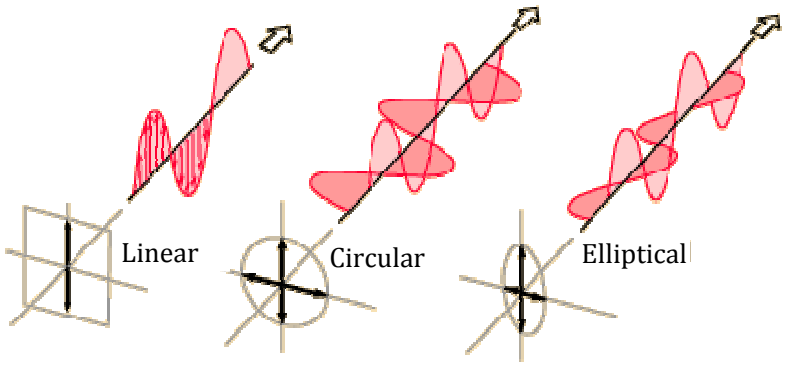

Figure 2-3: Illustration of the vibration of the components of the electric field vector in a plane perpendicular to the direction of propagation of the associated light wave for linearly, circularly and elliptically polarized light. [5]

To mathematically describe the SOP of a light wave, one usually relies on either the Stokes or Jones formalisms [6–8]. The Stokes formalism allows describing partially polarized light and relies on the use of field intensities. The Jones formalism, on the other hand, mathematically describes the polarization state of a wave by considering this state as a complex two-dimensional vector that contains the polarization dependent parameters of the electrical field vector. This formalism allows straightforwardly calculating the effect of a series of polarizing linear optical elements on the polarization state of an input wave. Since we will always consider fully polarized light and since we will have to look at how a

sequence of optical elements influences the SOP, we will proceed by using the Jones formalism. Equation (2.5) shows the polarization vector $\overline{P}$ associated to the electrical field vector $\overline{E}$:

$$\overline{P} = \begin{bmatrix} E_{0x} e^{i\Delta} \\ E_{0y} \end{bmatrix} \tag{2.5}$$

The time-dependent term ωt does not contain information about the SOP of the wave and hence it is disregarded in this notation. In the Jones formalism, an optical element traversed by the light wave such that it influences the SOP of the wave can be associated with a 2×2 matrix. The Jones matrix linking the input SOP represented by $\overline{P}_{in}$ to the output SOP represented by $\overline{P}_{out}$ is given in equation (2.6).

$$\overline{P}_{out} = \begin{bmatrix} J_{11} & J_{12} \\ J_{21} & J_{22} \end{bmatrix} \overline{P}_{in} \tag{2.6}$$

For example, the Jones matrices of a linear polarizer aligned with the y-axis, of a quarter-wave plate and of a general phase retarder plate are given by equations (2.7), (2.8) and (2.9), respectively.

$$M_{LP} = \begin{bmatrix} 0 & 0 \\ 0 & 1 \end{bmatrix} \tag{2.7}$$

$$M_{QWP} = \begin{bmatrix} e^{-i\pi/4} & 0 \\ 0 & e^{i\pi/4} \end{bmatrix} \tag{2.8}$$

$$M_{PR} = \begin{bmatrix} e^{i\varepsilon_x} & 0 \\ 0 & e^{i\varepsilon_y} \end{bmatrix} \tag{2.9}$$

The quarter-wave plate induces a phase retardance of π/2. Such a quarter wave plate oriented at 45° with respect to the vertical axis converts vertically linearly polarized light into circularly polarized light. In section 2.1.3.3. we will further clarify the mechanism of a quarter wave plate.

2.1.3 Retardance and birefringence

2.1.3.1 Absolute retardance

Consider two rays of light representing two light waves, a first (ray_1) passing through a parallel plate with thickness d and refractive index n_1 and a second undisturbed ray (ray_2), as illustrated in Figure 2-4. The refractive index of the surrounding medium is n_0. The phase velocity of light in the plate is $v_1 = c / n_1$. It takes a time $t_d = d / v_1$ for the light to traverse the plate. Meanwhile and in the same time t_d ray_2 travels a distance $d_0 = v_0 \times \frac{d}{c / n_1}$.

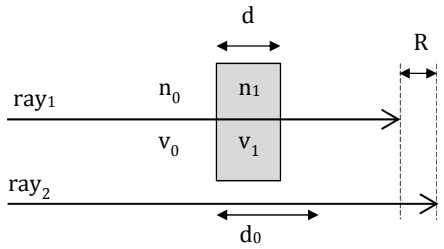

Figure 2-4: Absolute retardance R of a light ray caused by a parallel plate.

As a consequence ray_1 will lag behind ray_2 with an amount that can be represented by the distance R given in equation(2.10). That distance R is called the *absolute retardance* of the light caused by the plate.

$$R = d_0 - d = \left(\frac{n_1 - n_0}{n_0} \right) d \tag{2.10}$$

2.1.3.2 Birefringence

In a birefringent or optically anisotropic material, the refractive index experienced by a light wave depends on the polarization and on the direction of propagation of said light wave. An extensive treatment of birefringent materials can be found for example in [9]. One can show that a transverse electromagnetic plane wave can propagate through anisotropic

materials, but for propagation in a general direction two distinct allowed linear polarizations specified by the direction of propagation can exist for the wave. These two allowed polarizations are orthogonal and each of these propagates with a different phase velocity. A wave of arbitrary polarization entering such an anisotropic material will be decomposed into the two linearly polarized components polarized along the allowed directions. To determine the allowed orthogonal polarization directions and their corresponding refractive indices (and hence phase velocities) for a wave propagating in a given direction, one calls upon an ellipsoidal surface known as the 'indicatrix' or 'index ellipsoid' [10].

The index ellipsoid is a geometrical construction that allows determining the refractive index and thus the wave velocity experienced by the wave component vibrating along a particular direction for a given direction of propagation. If the ellipsoid is aligned with the orthogonal axes system x, y and z, the values n_x, n_y and n_z correspond to the principal axis of the ellipsoid illustrated in Figure 2-5. In the most general case, the three refractive indexes are different. The crystals of that category are named biaxial crystals.

Uniaxial crystals are characterized by $n_x = n_y \neq n_z$. We define the direction of the symmetry axis, the z-direction, as the optical axis of the crystal. The refractive index ellipsoid becomes an ellipsoid of revolution. A wave entering a uniaxial crystal is split into 2 waves: the ordinary wave, which is linearly polarized perpendicular to the optical axis and experiences the refractive index n_x and the orthogonally linearly polarized extraordinary wave, with refractive index and thus velocity depending on the angle between the wave normal and the optical axis. A uniaxial crystal can be used to make a quarter wave plate. The plate is cut parallel to the optical axis in such a way that the thickness of the plate generates a phase difference between the ordinary and extraordinary ray equal to a quarter of a wavelength. The axis corresponding to the fastest and the slowest components of the quarter wave plate is called, respectively, the fast and the slow axis.

In an optically isotropic material, $n_x = n_y = n_z$ and the index indicatrix is a sphere. The polarization of a wave entering such a material will not be

altered. Unperturbed and homogeneous silica glass can usually be considered to be an isotropic material.

The birefringence in materials is either natural (e.g. in uniaxial or biaxial crystals) or can be induced by the existence of stress in the material. In a material with stress-induced birefringence, the principal axes of the index ellipsoid coincide with the principal stress axes as illustrated in Figure 2-5. The principal indices of refraction n_1, n_2 and n_3 are each a function of the three stress-components σ_1, σ_2 and σ_3.

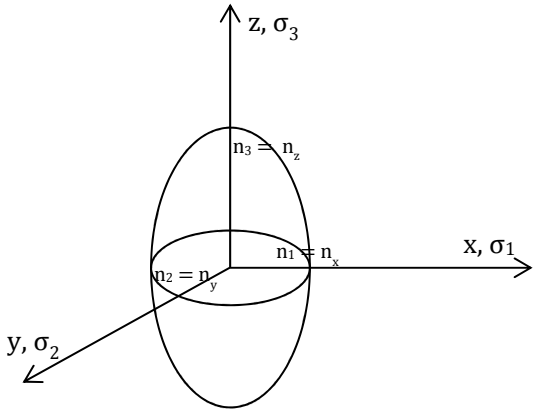

Figure 2-5: The principal axes of the index ellipsoid coincide with the principal stress axes.

The **stress-optic law** describes the relation between the three principal refractive indices and the three principal stresses (equation (2.11)):

$$\begin{cases} n_1 = n_0 + C_1\sigma_1 + C_2(\sigma_2 + \sigma_3) \\ n_2 = n_0 + C_1\sigma_2 + C_2(\sigma_1 + \sigma_3) \\ n_3 = n_0 + C_1\sigma_3 + C_2(\sigma_1 + \sigma_2) \end{cases} \tag{2.11}$$

with n_0 the index of refraction of the unstressed material. C_1 and C_2 are the so-called stress-optic constants. The stress-optic constants are material

dependent. They govern the photoelastic behavior of glass and other transparent materials [2, 10].

If we consider a plate in a two-dimensional or plane stress state, the principal stress σ_3 equals zero. If polarized light travels through the plate along the z-axis, the incident wave splits into two orthogonally linearly polarized components oscillating in the yz and xz planes. Because of the stress-induced birefringence, each component will experience a different refractive index in accordance with the stress-optic law. The relative retardance δ between the components emerging from the plate can then be given by equation (2.12).

$$\begin{aligned} \delta = n_1 d - n_2 d &= (C_1\sigma_1 + C_2\sigma_2 - C_1\sigma_2 - C_2\sigma_1)d \\ &= (C_1 - C_2)(\sigma_1 - \sigma_2)d \\ &= C(\sigma_1 - \sigma_2)d \end{aligned} \tag{2.12}$$

where d is the thickness of the plate and $C=C_1-C_2$ is the photoelastic constant used to analyze the photoelastic behavior of transparent material [2].

Another example that we will use later in this dissertation, is an isotopic material with a refractive index n_0 submitted to a tensile stress $\sigma_3 = \sigma_z$ along the z-direction, and with stresses σ_1 and σ_2 equal to zero. The value of the refractive index tensor seen by an incoming wave will change in accordance with equation (2.11).

$$\begin{aligned} n_1 = n_2 &= n_0 + C_2\sigma_3 \\ n_3 &= n_0 + C_1\sigma_3 \end{aligned} \tag{2.13}$$

The spherical indicatrix changes into an ellipsoid of revolution. Since we can conclude from (2.13) that $n_1 = n_2 \neq n_3$, the direction of the tensile stress coincides with the optical axis. Let us now consider a wave travelling perpendicularly to that direction, for instance along the x-axis. The wave will split in two components due to the stress-induced birefringence caused by σ_3. One component is linearly polarized along the y direction, whilst the second is linearly polarized along the z direction. The relative retardance δ between these two components emerging from the material sample with thickness d is then expressed by equation(2.14) .

$$\delta = n_3 d - n_2 d = (C_1 - C_2)\sigma_3 d = C\sigma_3 d \quad (2.14)$$

We note that the retardance is solely dependent of the applied tensile stress and of the thickness of the material sample.

2.1.3.3 Experimental photoelasticity

At this stage, we combine the polarization characteristics of light and the elastic properties of a transparent material submitted to stress. We have explained that polarized light passing through a stress-induced birefringent material will be decomposed into two orthogonal linearly polarized components experiencing a different refractive index and hence propagating at a different phase velocity. The stress-optic law (equation(2.11)) gives the relation between the stress in the material and the value of the refractive index.

Experimental photoelastic stress analysis relies precisely on the determination of the birefringence in material specimens using polarized light. For example, a circular polariscope arrangement allows accurately determining the relative retardance in one specific point of the specimen. It can also be used to perform a full field analysis of the sample. Such a polariscopic arrangement is illustrated in Figure 2-6. Two linear polarizers, a polarizer (P) and an analyzer (A) with perpendicularly oriented polarization axes, are placed at the two extremities of the setup. Their polarization directions are respectively vertically and horizontally oriented. The setup also contains two quarter wave retarders or plates (QWP), with crossed axes as well, and oriented at 45° with respect to the polarizer transmission axis.

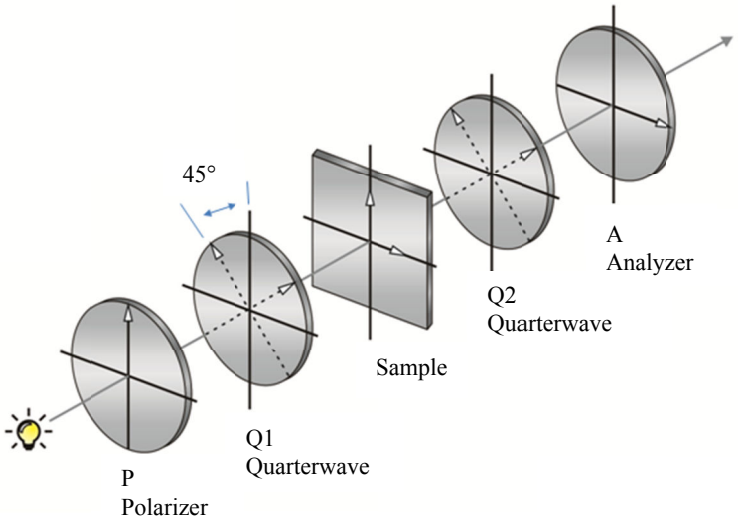

Figure 2-6: Arrangement of the optical elements in a circular polariscope. The polarizer and the analyser have crossed polarization axes. The fast axes of the quarter wave plates are crossed as well [11].

The sample to be analyzed is placed in the middle of the polariscope. This sample, if birefringent, will induce a phase retardance φ between the two allowed orthogonal linearly polarized waves that can propagate in the material. The relationship between the phase retardance φ and the relative retardance is given in equation (2.15) with λ the wavelength of the light wave.

$$\delta = \varphi \frac{\lambda}{2\pi} = C(\sigma_1 - \sigma_2)d \tag{2.15}$$

The Jones calculus associated with this setup to determine the Jones vector of the light wave emerging from the analyzer is given in equation(2.16) [12].

$$\overline{P}_{out} = M_A M_{QWP(-45°)} M_{Specimen} M_{QWP(+45°)} M_P \overline{P}_{in} \tag{2.16}$$

The corresponding matrix calculus is given in equation (2.17)

$$\begin{aligned} \overline{P}_{out} &= \begin{bmatrix} 1 & 0 \\ 0 & 0 \end{bmatrix} \begin{bmatrix} 1 & -i \\ -i & 1 \end{bmatrix} \begin{bmatrix} e^{i\varphi} & 0 \\ 0 & 1 \end{bmatrix} \begin{bmatrix} 1 & i \\ i & 1 \end{bmatrix} \begin{bmatrix} 0 & 0 \\ 0 & 1 \end{bmatrix} \overline{P}_{in} \\ \overline{P}_{out} &= \frac{1}{2} \begin{bmatrix} e^{i\varphi} - 1 \\ 0 \end{bmatrix} \end{aligned} \tag{2.17}$$

The intensity of the output vector can be written as in equation (2.18) [12].

$$I = \overline{P}_{out}^{*} \overline{P}_{out} = \sin^2 \frac{\varphi}{2} \tag{2.18}$$

This last equation shows that extinction of light in the polariscope setup is obtained when $\sin^2(\varphi/2) = 0$ and thus when $\varphi = 2n\pi$, i.e. when the relative retardance δ equals an integer number of wavelengths. Consequently, we get extinction when:

$$\varphi = 2\pi n = \frac{2\pi}{\lambda} C(\sigma_1 - \sigma_2) d \tag{2.19}$$

When carrying out a full field measurement of the specimen, the extinction creates dark interference fringes called 'isochromatics', i.e. loci of those points where the relative retardance is an integer multiple of the radiated wavelength. These lines coincide with locations where the principal stress difference $\sigma_1 - \sigma_2$ is constant [2, 8]. We illustrate such a full field circular polariscope analysis in Figure 2-7. It visualizes the isochromatic pattern of a disk under uniaxial tension. Each isochromatic fringe corresponds to an order n. The principal stress difference is found by counting the fringe order n and applying equation (2.19). We can also see from equation (2.19) that the zero-order fringe is wavelength-independent. Using a white light source yields colored fringes as for $n > 0$ extinction does not occur for all the wavelengths at the same time. Only the zero-order fringe will be dark. Using white light to obtain a colored isochromatic pattern is not an accurate method to determine the principal stress difference values as it relies on human judgment of colors. However, it allows locating the zero-order fringes before illuminating the sample with monochromatic light to determine the higher order fringes.

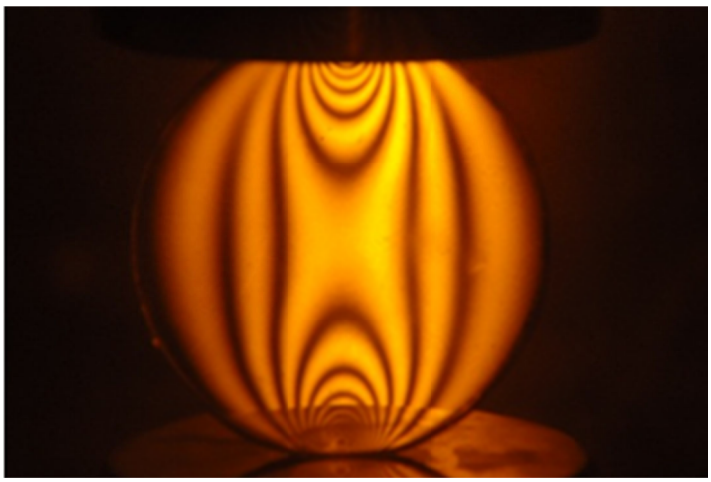

Figure 2-7: Isochromatic fringe pattern of a disk under diametral compression [13].

To illustrate the principle of colored isochromatics, Figure 2-8 shows the photoelastic stress-distribution for dental implants. It allows visualizing the distribution and the variation pattern of the principal stress differences.

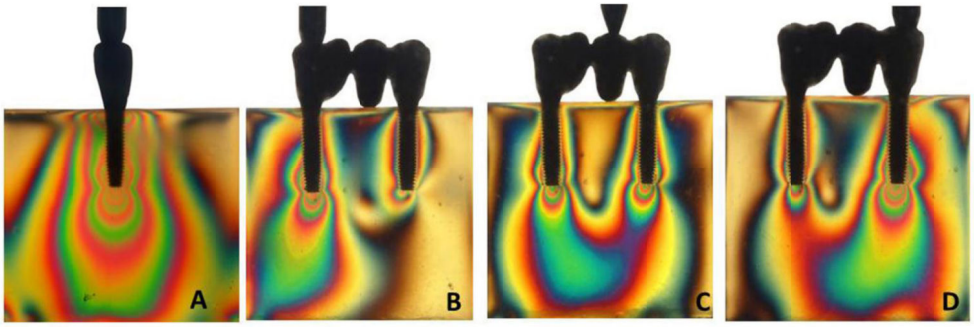

Figure 2-8: Photoelastic stress distribution analysis in dental implants by means of a circular polariscope [14]

2.2 Birefringence in optical fibers

2.2.1 Birefringence in a classic single mode fiber

In regular single mode optical fibers, only the fundamental core mode LP_{01} propagates through the core. The fundamental mode is the combination of the two degenerated propagation modes HE_{11}^{x} and HE_{11}^{y} [15]. The total electrical field associated to the light wave propagating in the core of the optical fiber is the superposition of the two polarization modes called the x and y modes. These modes are degenerated only if the optical fiber is perfectly circularly symmetric. If the circular symmetry is broken for any reason, the fiber core becomes birefringent and both modes will have different propagation constants, respectively $\beta_y = \frac{2\pi}{\lambda} n_y$ and $\beta_x = \frac{2\pi}{\lambda} n_x$. The birefringence is defined as $B = \frac{\lambda}{2\pi}\left|\beta_x - \beta_y\right| = \left|n_x - n_y\right|$. The difference in propagation constants results, for example, in the undesired spreading of an optical pulse launched in the fiber. Moreover, the polarization of light propagating through the fiber can change in an uncontrolled manner due to small asymmetries in the fiber due to errors introduced in the fabrication process and to external factors such as temperature variations or bend-induced birefringence.

The use of polarization-maintaining fibers helps to fix this issue. Birefringence is intentionally induced to increase the difference between the propagation constants of the two orthogonally polarized modes of propagation. We briefly discuss the principle of operation of polarization maintaining fibers (PMF) below.

2.2.2 Polarization maintaining optical fibers (PMF)

The total birefringence in the fiber is a combination of material birefringence and waveguide birefringence [16, 17]. The waveguide birefringence B_W is induced when the circular geometry of the fiber is broken. By producing an anisotropic refractive index distribution around the fiber core, one enhances the waveguide birefringence. In conventional optical fibers, this is achieved by using for example an elliptically shaped

core, as illustrated in Figure 2-9 (a). The material birefringence B_M results from an asymmetric transverse stress which produces birefringence through elasto-optic refractive index changes in the core [17]. By adding doped silica inclusions, symmetrically located at either side of the core and having different thermal expansion coefficients, thermal stress is internally frozen in the fiber during its cooling down in the production process. The fabrication process of the optical fibers will be addressed in Chapter 3.

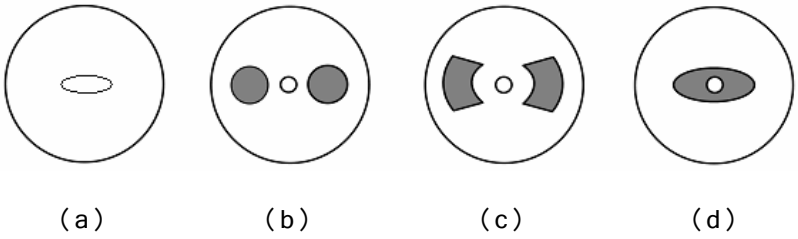

Figure 2-9: Cross-section of different polarization maintaining fibers; (a) elliptical core fiber, (b) Panda fiber, (c) bow-tie fiber and (d) elliptical cladding fiber. The dark zones are called 'inclusions'.[18]

Typical examples of material birefringent fibers are illustrated in Figure 2-9 (b) to (d), respectively the panda fiber, bow-tie fiber and elliptical cladding fibre that have inclusions of Boron-doped material. The level of birefringence achieved with such PMFs is about 5×10^{-4} [18]. PMF fibers are also called Hi-Bi fibers (Highly Birefringent fibers). Such fibers are used in applications where the preservation of the polarization is important, for example to connect a laser source to a modulator [19].

2.3 Polarimetric and Fiber Bragg grating sensors in a nutshell

2.3.1 Polarimetric sensors

PMFs typically exploit the photo-elastic effect for transducing a mechanical action into a measurable change of the PMF beat length [20–22]. The beat length L_B is the fiber length required to create a phase change of 2π. The relation between L_B and the birefringence B of a PMF is expressed in equation (2.20).

$$\Delta\varphi = \frac{2\pi}{\lambda} \times B \times L_B = 2\pi$$
$$L_B = \frac{\lambda}{B} \tag{2.20}$$

Consider linearly polarized light is launched into the fiber at 45° with respect to the principal polarization directions of the PMF. If the fiber is subjected to an external induced stress or strain, the birefringence or the beat length will change, leading to a phase shift between the two orthogonal components at the exit of the PMF fiber. Consequently, the PMF-based sensor is a polarimetric sensor transducing a mechanical quantity such as pressure, temperature or tensile stress into a measurable phase-shift between the two orthogonal polarized components of the wave vector traversing the fiber sensor.

2.3.2 Fiber Bragg grating sensors

The sensor principle of FBGs is also based on the photo-elastic effect for transducing a mechanical quantity into a change of the so-called Bragg wavelength.

Sensing principle of FBG in classical optical fibers

A FBG is an all-fiber component that can perform functions such as wavelength selective reflection and filtering. An FBG consists of a periodic modulation of the refraction index along the fiber core as illustrated in Figure 2-10. The distance between the grating planes Λ and the amplitude of the modulated refractive index n_{eff} are constant. The light guided along the core of the optical fiber will be scattered by each grating plane. The contributions of the reflected light from each grating plane satisfying the Bragg condition will add constructively in the backward direction and will form a reflected peak with a specific central wavelength λ_B defined by the grating parameters as described in equation (2.21). The grating acts as a mirror for that specific wavelength.

$$\lambda_B = 2 \times n_{eff} \times \Lambda \tag{2.21}$$

The mass-manufacturability of reliable Bragg gratings along with the advantages offered by the optical fibers such as low loss transmission, immunity to electromagnetic interference, light weight and small size makes FBG technology very attractive for telecommunication and sensing applications [21, 23–25]. Note that one FBG in a fiber is classified as a point-sensor. It is able to quantify a measurand at one specific location, i.e. at the location of the FBG along the fiber. Current fabrication processes also allow concatenating FBGs at multiple locations along the fiber. Using a different period Λ for each FBG allows associating a different Bragg wavelength with each sensing point. This is the basis for multiplexing many FBG point sensors in one optical fiber and enables quasi-distributed sensor networks to cover large areas with a minimum amount of optical fiber leads [26–29].

When the grating experiences thermal or mechanical perturbations, the effective refractive index changes according to the stress-optic law (equation (2.11)) and the period of the grating will be affected by changes in strain, stress and temperature in the fiber. As a consequence the Bragg condition is modified and the reflected wavelength λ_B will shift in amounts that are proportional (within certain limits) to the physical perturbation. Monitoring the Bragg wavelength shift resulting from the strain applied to the fiber or from a temperature change allows deriving the magnitude of these measurands. Typical sensitivities of λ_B to longitudinal strain and to temperature are of the order of 1 pm/μstrain and 10 pm/°C, respectively, at an operation wavelength of 1550 nm [30]. Note that a FBG in a classical optical fiber is not able to distinguish between simultaneous temperature and strain induced perturbations. The reflected Bragg peak shift returns an integrated response to both measurands.

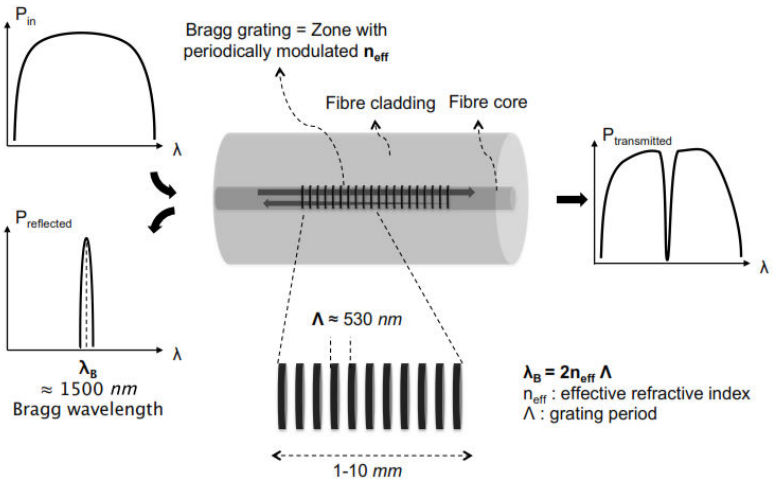

Figure 2-10: Illustration of a fiber with a Bragg grating. The period of the grating is Λ, the effective refractive index is n_{eff}. [31]

Let us consider a perfectly symmetric single mode fiber with two degenerated fundamental modes. A FBG in that fiber will reflect a single Bragg wavelength. If the fiber is subjected to pure axial stress, $\sigma_1 = \sigma_2 \neq \sigma_3$, the two degenerated modes will experience the same wavelength shift $\Delta\lambda_B$. The 1 and 2-axis refer to the transverse directions in the fiber, the 3-axis refer to the axial direction as represented in Figure 2-11.

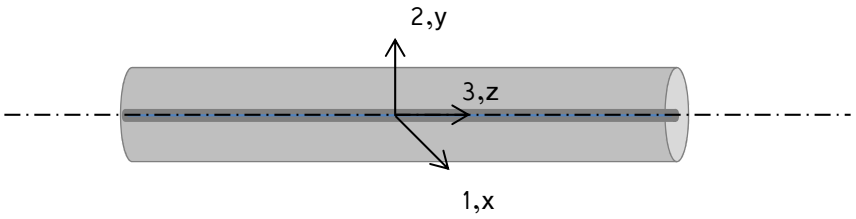

Figure 2-11: Coordinate system of the optical fiber. The 1 and 2 axes coincide with the transverse directions in the fiber, axis 3 refer to the axial direction. We assume the axis x,y and z correspond to the principal stress axis 1, 2 and 3.

If the fiber is subjected to an anisotropic load for which $\sigma_1 \neq \sigma_2 \neq \sigma_3$, the refractive indices along the transverse axes in the x and y direction will be different due to the stress-induced birefringence in the fiber. The refractive index variation seen by each orthogonal linearly polarized mode is governed by the stress-optic law. As a consequence the two propagation modes are no longer degenerated and the FBG reflection spectrum will show peak splitting. This phenomenon is illustrated in Figure 2-12. In that example the cladding of the FBG fiber sensor is subjected to a perpendicular line load. This causes the Bragg peak to split into two distinct peaks linked to the presence of stress in the core of the fiber. These two Bragg peaks are referred to as $\lambda_{B,fast}$ and $\lambda_{B,slow}$.

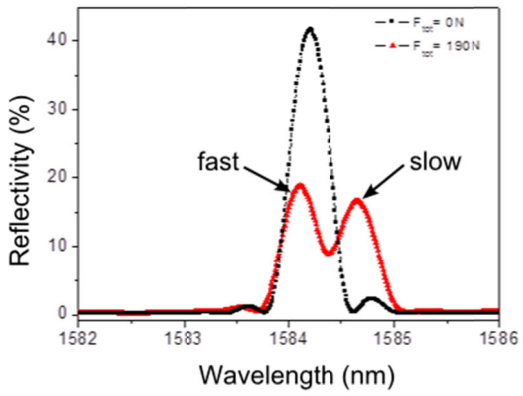

Figure 2-12: Simulated reflection spectrum of an FBG submitted to a uniform vertical line load inducing birefringence that causes peak splitting. [32]

These Bragg peaks are referred to as 'fast' and 'slow' in accordance with the naming of the polarization modes originating from their different phase velocity $v_{fast} = c/n_{eff,fast}$ and $v_{slow} = c/n_{eff,slow}$, with c the speed of light in vacuum and $n_{eff,fast}$ and $n_{eff,slow}$ the effective refractive indices of the fibre core experienced by the corresponding orthogonally polarized modes. We can derive the peak separation from equation (2.12) given in section 2.1.3.2:

$$\Delta\lambda_B = 2 \times \Delta n_{eff} \times \Lambda = 2 \times C \times \sigma_y \quad (2.22)$$

Equation (2.22) emphasizes the importance of the photoelastic coefficient C when dealing with a FBG sensor. In this specific example the knowledge of C allows predicting the amount of splitting of the reflected Bragg peak when the fiber sensor is subjected to anisotropic load.

FBG inscription methods

High quality FBGs can now be fabricated at relatively low cost. Several techniques exist to create a periodic interference pattern in the core of an optical fiber. A most common technique for 'inscribing' a FBG is to use a photosensitive fiber and illuminate it from the side with a pattern of UV-light to induce a permanent modulation of the refractive index in the core of the fiber [24, 31, 33]. The UV-light pattern can be obtained with a phase mask technique. This method is very stable and simple as it uses solely one optical component, a diffraction grating. The principle of this method is illustrated in Figure 2-13. Ultraviolet light that is incident normal to the phase is diffracted by the periodic corrugations in the mask. The phase mask is designed to suppress the 0 diffracted order such that most of the diffracted light is contained into the +1 and -1 diffracted orders. These two orders will interfere to give a sinusoidal intensity pattern, which photo-imprints a corresponding refractive index pattern into the fibre core. The optical fiber is placed directly behind the phase mask in the near field of the diffracted beams which reduces the sensitivity of the system to mechanical vibrations. This FBG fabrication technique is well-suited to mass production of gratings since it provides excellent manufacturing repeatability. The main disadvantage of this FBG inscription technique is that different masks are necessary for writing gratings with different Bragg wavelengths.

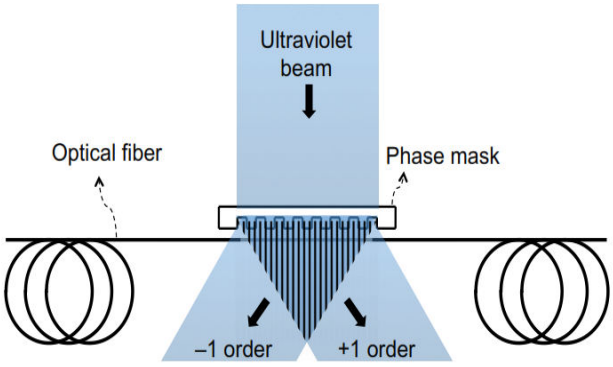

Figure 2-13: Illustration of the phase mask technique for the inscription of FBGs [31].

For applications where multiplexed FBGs are needed at different Bragg wavelengths, the interferometric FBG inscription technique is more suitable, as it allows tuning the Bragg wavelength by modifying the angle between the two interfering UV light beams [21]. Several other inscription techniques exist to inscribe FBGs in optical fibres. We refer to [34] for an overview.

2.3.3 FBG sensors in highly birefringent fibers

The total initial birefringence in a conventional highly birefringent fiber such as the PMF described in section 2.2.2, is the phase-modal birefringence B_{m0} defined as the difference between the initial effective refraction indices n_{x0} and n_{y0}, according to equation (2.23), with β the propagation constant and λ the wavelength of the light.

$$B_{m0} = \frac{\lambda}{2\pi}\left|\beta_x - \beta_y\right| = \left|n_{x0} - n_{y0}\right| \tag{2.23}$$

Since the fiber is highly birefringent, unpolarized light that is launched into the fiber yields two Bragg peaks, λ_{B1} and λ_{B2}, one for each orthogonally polarized mode propagating in the fiber as illustrated in Figure 2-14.

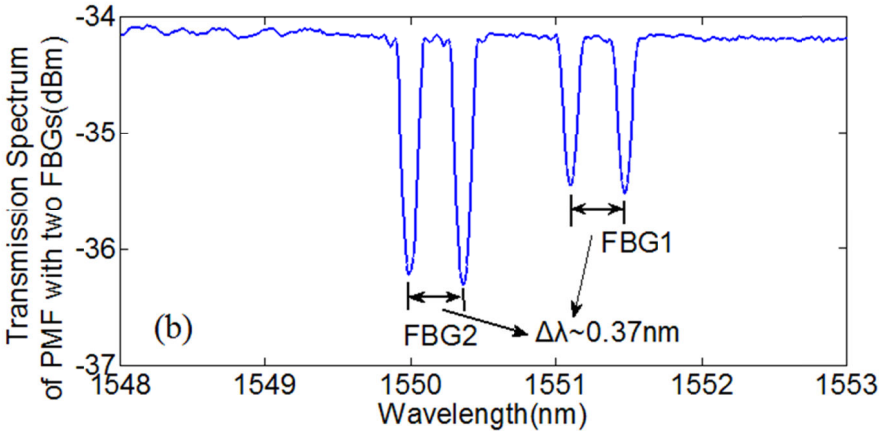

Figure 2-14: Illustration of the reflected spectrum of a PMF based sensor with two FBGs. The initial Bragg peak separation Δλ is indicated in the figure [35].

The spectral distance $\Delta\lambda_B$ between these two peaks is proportional to the phase modal birefringence B_{m0} and the grating periodicity Λ as expressed in equation (2.24).

$$\Delta\lambda_{B_0} = \lambda_{B1} - \lambda_{B2} = 2 \times \Lambda \times B_{m0} \tag{2.24}$$

In a HiBi fiber, we consider the variation of $\Delta\lambda_B$ rather than the position of individual Bragg wavelength λ_{B1} and λ_{B2}. It simplifies the wavelength detection as there is no need for an absolute wavelength measurement [22]. The additional stress-induced birefringence in the fiber is governed by the stress-optic law (equation (2.11)), which is repeated here for the sake of clarity. If the x, y and z axes correspond with the principal stress axes 1, 2 and 3 in the fiber (Figure 2-11), and if we consider a plane stress state, we can write:

$$\begin{cases} n_x - n_{x0} = C_1\sigma_x + C_2\sigma_y \\ n_y - n_{y0} = C_1\sigma_y + C_2\sigma_x \end{cases} \tag{2.25}$$

Subtracting the second expression from the first one yields equation (2.26):

$$\begin{aligned} B_m &= n_x - n_y = n_{x0} - n_{y0} + C(\sigma_x - \sigma_y) = B_{m0} + C(\sigma_x - \sigma_y) \\ B_m &= B_{m0} + B_s \end{aligned} \tag{2.26}$$

We designate B_S as the stress-induced birefringence. The variation of the modal birefringence will affect the Bragg peak separation $\Delta\lambda_{B0}$. This clearly shows how the sensing mechanism of FBG based sensors in birefringent optical fibers relies on the principle of photoelasticity, with the photoelastic constant C as unique material dependent parameter.

2.3.4 Microstructured Optical Fibers (MOF)

Another type of specialty fiber has emerged in the last two decades, i.e. the microstructured optical fibers (MOFs) or photonic crystal fibers (PCFs). They offer an interesting alternative to conventional optical fibers in the scope of specific applications [36–40]. A MOF is an optical fiber with an air hole structure that is running along the entire length of the waveguide. We distinguish two main classes of MOFs: the index guiding fibers and the bandgap guiding fibers. The index guiding principle is similar to that of the conventional fibers. The core region has a higher refractive index than the surrounding cladding region as the presence of air holes lower the average refractive index. In photonic bandgap fibers the light guidance is achieved by the presence of a two-dimensional photonic bandgap that confines the light in the low-index or hollow core. Figure 2-15 shows an example of both classes of MOFs.

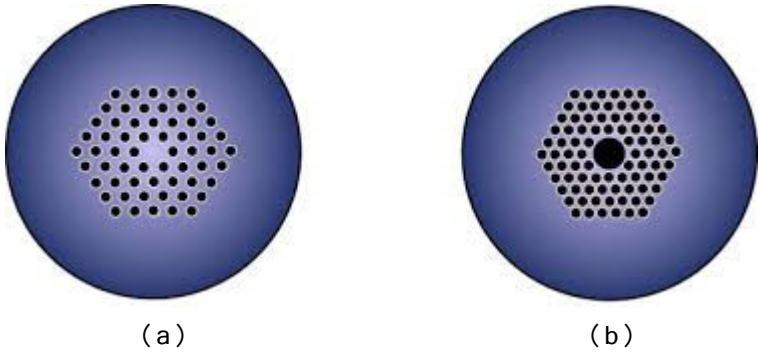

Figure 2-15: Illustration of MOFs with a hexagonal lattice: (a) index-guiding microstructured optical fiber and (b) bandgap guiding hollow core microstructured optical fiber [39].

The ability to control the number of air holes, to choose their diameter and their arrangement in the fiber cross-section opens the possibility to design MOFs with a wide range of properties that cannot be obtained with conventional optical fibres [12]. The development of MOF technology is driven by the opportunity to obtain fiber structures tailored to specific applications.

The introduction of asymmetries in the air hole arrangement of a MOF, for example by departing from the hexagonal lattice or by enlarging some air holes, introduces controlled birefringence. An example is the highly birefringent 'butterfly' MOF, depicted in Figure 2-16, which was designed by the B-PHOT research group at Vrije Universiteit Brussel (VUB) [41, 42]. The fiber and the shape of the microstructure were designed such that a FBG based sensor fabricated with that fiber features a high sensitivity of the Bragg peak separation to hydrostatic pressure and to transverse strain, whilst at the same time being minimally sensitive to temperature changes. The two reflected Bragg peaks respond in an opposite way to hydrostatic pressure and transverse load.

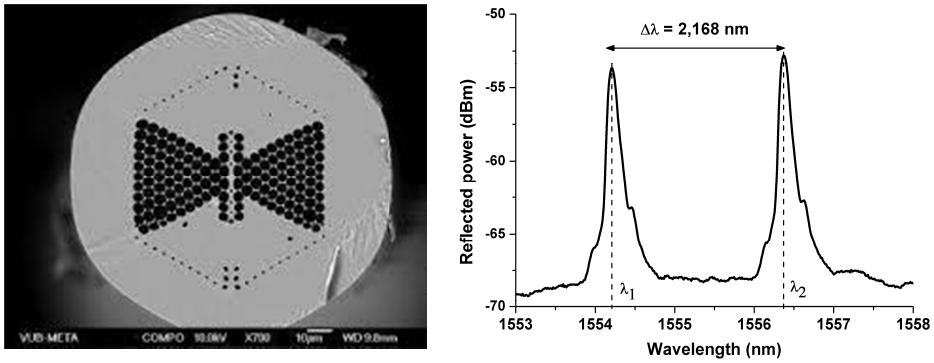

Figure 2-16: The butterfly MOF: (a) The asymmetric air hole lattice induces large deformation in the core region. (b) FBG reflection spectrum of a butterfly MOF sensor with the indication of the initial Bragg peak separation [41].

When the birefringent MOF structure is mechanically loaded, an anisotropic stress distribution will be induced in the fiber core, along with a deformation of the microstructure. Both mechanisms will affect the modal birefringence B_{m0} of the MOF.

2.3.5 Illustration of operation with a highly birefringent MOF FBG sensor

We determine the evolution of the reflected Bragg peak separation of a highly birefringent MOF. The cross-section of the MOF design we consider is illustrated in Figure 2-17. The internal microstructure is composed of 3 rows of air holes surrounding a doped core region (7 mol% GeO_2). The outer silica diameter is 125 μm [22, 43].

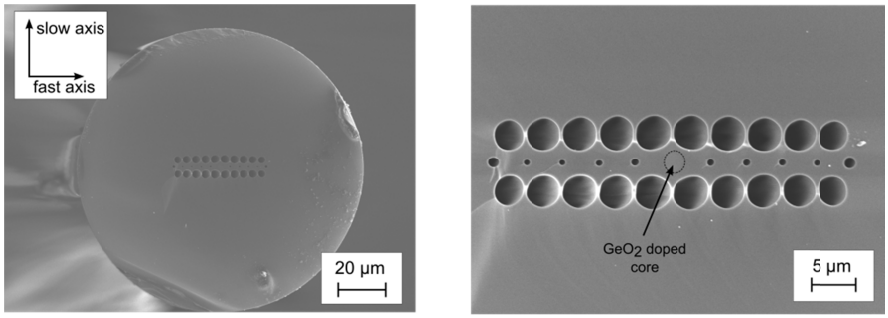

Figure 2-17: Cross section of the MOF we utilize in our simulations. (a) Scanning electron micrograph image of the cross-section of a highly birefringent MOF developed at Vrije Universiteit Brussel for transverse strain sensing applications and manufactured at University Marie Curie-Sklodowska (Poland). (b) Close-up of the central microstructure of the MOF. [32, 44]

We consider a line load F_y [N/mm] along the optical axis (taken along z) of the fiber, orthogonal to the x and z direction but parallel to the y-axis. The transversal line-load will induce a mechanical stress-concentration σ_y in the core region that will modify the refractive index distribution experienced by the two orthogonally polarized modes. Equation (2.25) becomes:

$$B_m = n_x - n_y = n_{x0} - n_{y0} - (C_1 - C_2)\sigma_y = B_{m0} - C\sigma_y \qquad (2.27)$$

We compute the change of the Bragg wavelength $\Delta\lambda_{Bm}$ using the commercially available finite element analysis software COMSOL Multiphysics [40, 45]. The response of the Bragg peak separation is given in Figure 2-19. The Bragg grating periodicity is chosen to be 530nm. We also derive the sensitivity the fiber sensor to perpendicular line load according to equation (2.28).

$$\frac{d\Delta\lambda_{Bm}}{dF} = 2 \times \frac{dB_m}{dF} \times \Lambda \qquad (2.28)$$

The average sensitivity of the simulated FBG MOF to a perpendicular line load equals 150 pm/(N/mm). This sensitivity is close to the values reported for conventional birefringent fibers [18]. Note that the butterfly MOF presented in [46–48] is almost four times more sensitive (-370 pm/(N/mm)).

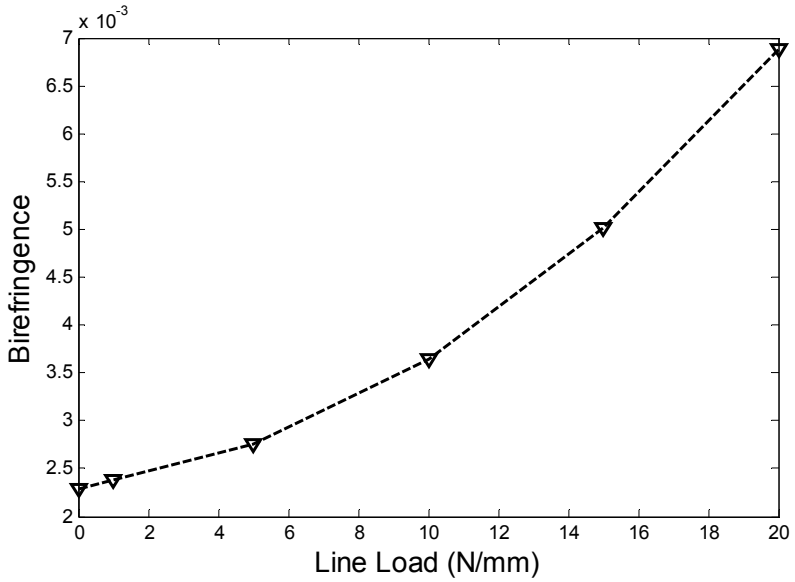

Figure 2-18: Birefringence B_m evolution for an increasing vertical line-load. The initial phase-modal birefringence of the MOF is 0,0023. The simulated sensitivity of the MOF to perpendicular line load equals 150 pm/(N/mm).

2.4 Impact of the photoelastic constant on a FBG based sensor response

We have learnt from the previous sections that the photoelastic coefficient is an important material parameter of the optical fiber as it impacts the transduction mechanisms in polarization based optical fiber sensors and in FBG based sensors.

When designing dedicated mechanical optical fiber sensors or when predicting the response of such sensors that exploit photoelasticity, one should therefore have accurate knowledge of the value of the photoelastic constant. To illustrate the impact of the uncertainty on the value of C, we have simulated the variation of the birefringence B_m in the MOF sensor discussed in section 2.3.4 as a function of the uncertainty on C [49]. The birefringent MOF has a phase-modal birefringence B_{m0} of 2.3×10^{-3}. We apply a vertical line load of 15 N/mm to the grating and we compute the resulting change of the birefringence B_m using the finite element analysis software COMSOL Multiphysics [45]. The results of the simulation are shown in Figure 2-19. The central point of the graph corresponds to the nominal value of $C_{nom} = -3.52\times10^{-12}$ Pa^{-1} measured on bulk silica taken from [50]. That value is still commonly used for simulating silica optical fibers.

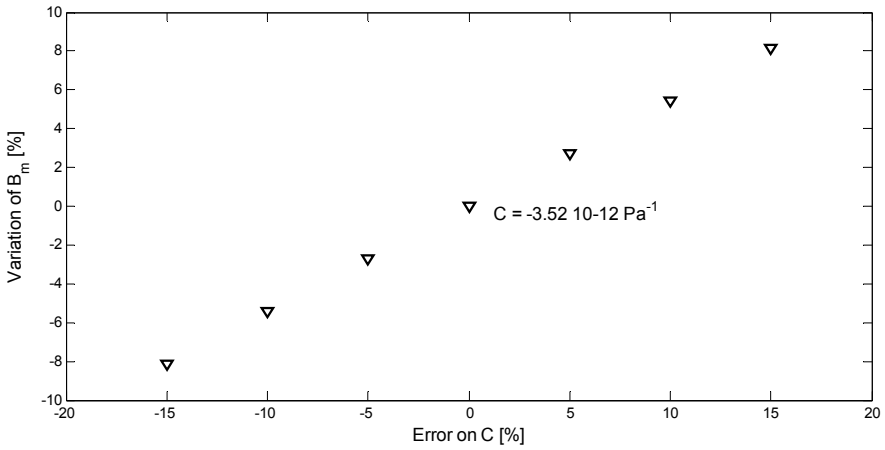

Figure 2-19: Variation of the total birefringence B_m for a maximal error of $\pm15\%$ on C_1 and C_2, with $C = C_1 - C_2$. The applied vertical line load is 15 N/mm.

We then change the value of C by modifying the values of C_1 and C_2 with $\pm15\%$ from their nominal values and we calculated B_m for the same applied transverse line load of 15 N/mm. We conclude from Figure 2-19 that an uncertainty on the knowledge of the stress-optic parameters leads to an

uncertainty of a similar amplitude on the simulated deviation of the birefringence and hence that the uncertainty on C may lead to significant deviations between calculated and measured responses of a fiber Bragg grating exposed to mechanical load. Note that the initial birefringence B_{m0} is not dependent on the variation of C as it is a constant term in the expression of the total birefringence B_m. This explains that the variation of B_m has a smaller amplitude than the error on C. Considering solely the term of the stress-induced birefringence, the deviation on B_S has the same amplitude as the error on C.

To further illustrate the impact of the uncertainty on C, we simulate the birefringence in the same fiber for an increasing vertical line load for different values of C. The results are presented in Figure 2-20.

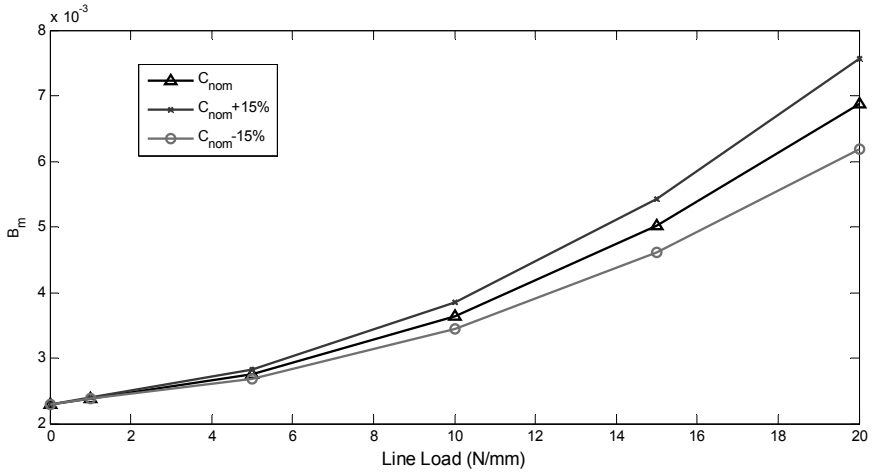

Figure 2-20: Evolution of the birefringence B_m for an increasing value of the vertical line-load for 3 values of C.

We can clearly see the impact of an error on the photoelastic constant on the total birefringence predicted by the simulations. Simulating with an erroneous value of the photoelastic constant C leads to an error in the predicted sensitivity of the FBG sensor. In our example, the sensitivity varies from 133 pm/(N/mm) to 180 pm/(N/mm). The use of an erroneous

value of C thus generates a mismatch between the simulated - and therefore expected - response of the sensor and the effective response and sensitivity of the manufactured fiber sensor fabricated based on the simulated design. This stresses the importance of the ability to measure the photoelastic coefficient of an optical fiber with adequate accuracy.

2.5 Impact of the photoelastic constant on applications in telecommunications

To end this Chapter and with the only aim to extend a little on the scope of this research, we shortly discuss how the accurate knowledge of C is not only crucial for the development of tailored sensing applications, but can also be important for optical fiber telecommunications.

In the telecommunication area, the increasing need for a high performance network requires fibers that minimally degrade signal transmission. Effects including chromatic dispersion (CD), polarization-dependent-loss (PDL), polarization-mode dispersion (PMD), and fiber non-linearities should be avoided [51].

The random varying asymmetries in the fiber core along the fiber length induce some unwanted birefringence that results in PMD. A perfect single mode fiber guides only one mode at a defined optical wavelength. This fundamental mode consists of two degenerated polarization states. However, the imperfections of a real fiber cause the optical light to split between the two orthogonal polarization states of the fiber. Each polarization component travels at a different speed and creates a differential group delay (DGD), which results in pulse spreading and hence limits the data transmission rate. The mean or expected value of the DGD is defined as the PMD. The impact on the telecommunication system performance of the PMD is not negligible, especially in older fiber networks. For each binary symbol '0' or '1', a light pulse is sent within the timeslot T_B of the binary symbol. The PMD induced delay stretches the duration of each individual pulse. Distortion arises when the tail of the leading pulse overlaps with the leading edge of the next pulse, provoking inter symbol interference (ISI). As a result the optical receiver may not always be able to decide whether it sees a '1' or a '0'. At a low data rate (~2,5Gbit/s) the bit

period T_B is long compared to the added delay of PMD and distortion does not occur. However, as the demand for increasing data rates is a reality, the bit period is drastically shortened to obtain data rates well above 40 Gbits/s. In that case, the PMD becomes an issue. ITU standards (e.g. G691 and G657 [52, 53]) now define requirements for a fiber system to enable multi-vendor compatibility. For instance, the maximum DGD of an entire optical path should not exceed DGD_{max}, defined as 30% of the bit period T_B. So let us illustrate the influence of optical fiber material parameters on the determination of the differential group delay (DGD) caused by a non-circular core of the fiber. A non-circular core results in undesired birefringent effects: first in a geometrical birefringence inducing a $DGD_{GEOMETRICAL}$ solely function of the waveguide parameters [54], and second in the appearance of non-symmetrical stress-fields that will induce stress birefringence and hence a DGD_{STRESS}. The latter is function of the material parameters of the optical fiber [55, 56] as described in equation (2.29).

$$DGD_{STRESS} = -\frac{\varepsilon}{c}\frac{\Delta\alpha\Delta T}{2(1-\upsilon)} \times E \times C \times G(W_p) \qquad (2.29)$$

The parameters of equation (2.29) are defined as follow:

- ε : ellipticity of the core,
- c : speed of light in vacuum,
- Δα: difference between the thermal expansion coefficients of respectively the core and the cladding of the fiber,
- ΔT: difference between the high softening temperature of the doped core and the room temperature,
- ν: Poisson coefficient,
- E: Young modulus,
- C: photoelastic constant
- $G(W_p)$: a function of the waveguide parameters (core and cladding diameter, refractive index, ellipticity, wavelength)

Predicting whether the DGD remains within the specified and severe limits defined by international optical communication specifications therefore also calls for accurate knowledge of C.

2.6 Summary

In this introductory Chapter we have introduced the basic principles of photoelasticity. We have provided an overview of how elasticity of a material is linked with the polarization properties of a light wave traversing the material. Next, we explained the birefringence in classical optical fibers and polarization maintaining fibers. The latter are highly birefringent and are convenient in polarimetric sensing applications where they act as transducers for mechanical quantities based on the photoelastic effect.

Afterwards we presented another sensing mechanism exploiting the photoelastic effect with the inscription of FBG in the optical fibers. The sensing mechanism is based on the periodic change of the refraction index over a given distance in the optical fiber. The wavelength satisfying the Bragg condition is reflected by the grating. Due to external mechanical perturbations, the effective refractive index in the fiber changes according the stress-optic law and eventually the grating period changes as well. As a consequence the Bragg condition is modified and the reflected Bragg wavelength will shift.

To proceed with specialty fiber based sensors, we introduced the concept of a FBG in a polarization maintaining fiber yielding two reflected Bragg peaks as a consequence of the highly birefringent nature of the PMF. The sensing mechanism is based on the relative variation of the two reflected peaks resulting from additional stress-induced birefringence in the PMF fiber under external mechanical loads. We also introduced sensors fabricated in highly birefringent microstructured optical fibers. For all those cases we have shown that photoelasticity plays a crucial role in the transduction mechanism and that accurate knowledge of the material parameters, and of the photoelastic coefficient in particular, is required if we want to correctly predict the response of the optical fiber sensor to mechanical load.

In a last section we briefly illustrated that accurate knowledge of C is also important for optical fiber telecommunication applications.

In Chapter 3 we will give an overview of the measurement techniques to determine C in bulk silica and in polymer material and further comment on the necessity to measure this value preferably directly on the fiber.

Bibliography

[1] A. Kuske and G. Robertson, *Photoelastic stress analysis*. 1974.

[2] G. L. Cloud, *Optical methods of engineering analysis*. Cambridge University Press, 1998.

[3] J. Javornicky, *Photoplasticity*. Prague: Publishing House of the Czechoslovak Academy of Sciences, 1974.

[4] J. Doyle and J. Phillips, "Manual on experimental stress analysis," *Soc. Exp.*, 1989.

[5] "Polarization concepts." [Online]. Available: http://hyperphysics.phy-astr.gsu.edu/hbase/phyopt/polclas.html.

[6] F. L. Pedrotti and L. S. Pedrotti, "Introduction to optics 2nd edition," *Introduction to Optics 2nd Edition by Frank L. Pedrotti, SJ, Leno S. Pedrotti New Jersey: Prentice Hall, 1993*, vol. 1. 1993.

[7] P. Hariharan, *Optical interferometry, second edition*. London: Academic Press, Elsevier, 2003.

[8] K. J. Gadvik, *Optical metrology*, Third Edit. Wiley & Sons, LTD, 2002.

[9] A. Yariv and P. Yeh, *Optical Waves in Crystals Propagation and Control of Laser Radiation*. Wiley Interscience Publication, 2002.

[10] M. Born and E. Wolf, "Principles of optics," *Principles of Optics Electromagnetic Theory of Propagation INterference and Diffraction of Light 2nd edition by Max Born Emil Wolf New York NY Pergamon Press 1964*. pp. 1–952, 1999.

[11] "Optics Thoeries." [Online]. Available: http://support.moldex3d.com-/r14/moldex3d/module-introduction/standard-injectionmolding/-material/material-models/optics-theories/.

[12] P. S. Theocaris and E. E. Gdoutos, *Matrix Theory of Photoelasticity*. Springer, 2013.

[13] R. Uddanwadiker, "Effect of Rim Thickness on Load Sharing in the Rotating Elements." [Online]. Available: http://pubs.sciepub.com/ajme/1/5/4/.

[14] M. Coelho Goiato, A. A. Pesqueira, D. M. Dos Santos, M. F. Haddad, and A. Moreno, "Photoelastic stress analysis in prosthetic implants of different diameters: mini, narrow, standard or wide.," *J. Clin. Diagn. Res.*, vol. 8, no. 9, p. ZC86-90, 2014.

[15] A. W. Snyder and J. D. Love, *Optical waveguide theory*. London: Chapman & Hall, 1991.

[16] S. C. Rashleigh, W. K. Burns, R. P. Moeller, and R. Ulrich, "Polarization holding in birefringent single-mode fibers.," *Opt. Lett.*, vol. 7, no. 1, pp. 40–42, 1982.

[17] J. Noda, K. Okamoto, and Y. Sasaki, "Polarization-maintaining fibers and their applications," *J. Light. Technol.*, vol. 4, no. 8, pp. 1071–1089, 1986.

[18] E. Chehura, C.-C. Ye, S. E. Staines, S. W. James, and R. P. Tatam, "Characterization of the response of fibre Bragg gratings fabricated in stress and geometrically induced high birefringence fibres to temperature and transverse load.," *Smart Mater. Struct.*, vol. 13, pp. 888–895, 2004.

[19] A. Krischke, U. Oechsner, C. Knothe, and A. Lamott, "Components and Tools for Polari- zation-maintaining Fiber Optics: Technology for industrial and scientific applications," *Laser Tech. J.*, vol. 9, no. 1, pp. 30–34, 2012.

[20] A. D. Kersey and M. A. Davis, "Fiber grating sensors," *J. Light. Technol.*, vol. 15, no. 8, pp. 1442–1463, 1997.

[21] A. Othonos and K. Kalli, *Fiber Bragg gratings: fundamentals and applications in telecommunications and sensing*. Artech House, INC, 1999.

[22] T. Geernaert, G. Luyckx, and E. Voet, "Transversal load sensing with fiber Bragg gratings in microstructured optical fibers," *IEEE PHOTONICS Technol. Lett.*, vol. 21, no. 1, 2009.

[23] K. O. Hill, B. Malo, F. Bilodeau, D. C. Johnson, and J. Albert, "Bragg gratings fabricated in monomode photosensitive optical fiber by UV exposure through a phase mask," *Appl. Phys. Lett.*, vol. 62, no. 10, pp. 1035–1037, 1993.

[24] K. O. Hill and G. Meltz, "Fiber Bragg grating technology fundamentals

and overview," *J. Light. Technol.*, vol. 15, no. 8, pp. 1263–1276, 1997.

[25] A. Othonos, "Fiber Bragg gratings," *Rev. Sci. Instrum.*, vol. 68, no. 12, p. 4309, 1997.

[26] X. Bao and L. Chen, "Recent progress in Brillouin scattering based fiber sensors," *Sensors*, vol. 11, no. 4, pp. 4152–4187, 2011.

[27] W. Zou, Z. He, and K. Hotate, "Complete discrimination of strain and temperature using Brillouin frequency shift and birefringence in a polarization-maintaining fiber.," *Opt. Express*, vol. 17, no. 3, pp. 1248–1255, 2009.

[28] D. P. Zhou, W. Li, L. Chen, and X. Bao, "Distributed temperature and strain discrimination with stimulated brillouin scattering and rayleigh backscatter in an optical fiber," *Sensors (Switzerland)*, vol. 13, no. 2, pp. 1836–1845, 2013.

[29] C. Crunelle, C. Caucheteur, M. Wuilpart, and P. Mégret, "Quasi-distributed temperature sensor combining Fibre Bragg Gratings and temporal reflectometry technique interrogation," *Opt. Lasers Eng.*, vol. 47, no. 3–4, pp. 412–418, 2009.

[30] M. Ramakrishnan, G. Rajan, Y. Semenova, and G. Farrell, "Overview of Fiber Optic Sensor Technologies for Strain/Temperature Sensing Applications in Composite Materials.," *Sensors (Basel).*, vol. 16, no. 1, p. 99, 2015.

[31] F. Berghmans and T. Geernaert, "Optical fiber point sensors," in *Advanced Fiber Optics: Concepts and Technology*, L. Thévenaz, Ed. EPFL Press, 2011.

[32] C. Sonnenfeld, "Microstructured Optical Fibre Bragg Grating Sensors for Production and Health Monitoring of Carbon Fibre Reinforced Polymer Materials and Structures," PhD dissertation, Vrije Universiteit Brussel, 2013.

[33] F. Berghmans, T. Geernaert, T. Baghdasaryan, and H. Thienpont, "Challenges in the fabrication of fibre Bragg gratings in silica and polymer microstructured optical fibres," *Laser and Photonics Reviews*, vol. 8, no. 1. pp. 27–52, 2014.

[34] K. Sudgen and V. Mezentsev, "Fiber Bragg Gratings: Advances in

Fabrication Process and Tools," in *Fiber Bragg Grating Sensors: Recent Advancements, Industrial Applications and Market Exploitation*, Bentham Sc., vol. chap. 2, pp. 9–34, A. Cusano, A. Cutolo, and J. Albert, Eds. 2011,.

[35] Y. Zhao, B. Sun, Y. Liu, J. Ren, J. Zhang, J. Yang, J. Canning, G. D. Peng, and L. Yuan, "Polarization mode coupling and related effects in fiber Bragg grating inscribed in polarization maintaining fiber," *Opt. Express*, vol. 24, no. 1, p. 611, 2016.

[36] A. Bjarklev, J. Broeng, and A. S. Bjarklev, *Photonic Crystal Fibres*. Kluwer Acadmic Publisher, 2003.

[37] J. C. Knight, "Photonic crystal fibers and fiber lasers (Invited)," *J. Opt. Soc. Am. B*, vol. 24, no. 8, p. 1661, 2007.

[38] P. S. J. Russell, "Photonic-crystal fibers," *J. Light. Technol.*, vol. 24, no. 12, pp. 4729–4749, 2006.

[39] O. Frazão, J. L. Santos, F. M. Araújo, and L. a Ferreira, "Optical sensing with photonic crystal fibers," *Laser Photon. Rev.*, vol. 2, no. 6, pp. 449–459, 2008.

[40] F. Berghmans, T. Geernaert, M. Napierała, T. Baghdasaryan, C. Sonnenfeld, S. Sulejmani, T. Nasiłowski, P. Mergo, T. Martynkien, W. Urbańczyk, E. Bereś-Pawlik, and H. Thienpont, "Applying optical design methods to the development of application specific photonic crystal fibres," in *Optical Systems Design 2012*, 2012, vol. 8550.

[41] T. Geernaert, "Microstructured fiber bragg grating sensors: from fiber design to sensor implementation," PhD dissertation, Vrije Universiteit Brussel, 2010.

[42] T. Geernaert, F. Berghmans, T. Nasilowski, H. Thienpont, M. Makara, P. Mergo, K. Poturaj, W. Urbanczyk, T. Martynkien, and J. Olszewski, "Birefringent micro-structured optical fiber for sensor application," WO2011061309 A1, 2011.

[43] T. Geernaert and T. Nasilowski, "Fiber Bragg gratings in germanium-doped highly birefringent microstructured optical fibers," *IEEE Photonics Technol. Lett.*, vol. 20, no. 8, pp. 554–556, 2008.

[44] T. Geernaert, K. Chah, T. Nasilowski, H. Ottevaere, F. Berghmans, and H.

Thienpont, “Fiber Bragg Grating Inscription in Highly Asymmetric HiBi PCF with a Low Intensity UV CW laser,” *Proc. Symp. IEEE*, pp. 31–34, 2007.

[45] “www.comsol.com/products/multiphysics.” .

[46] S. Sulejmani, C. Sonnenfeld, T. Geernaert, F. Berghmans, H. Thienpont, S. Eve, N. Lammens, G. Luyckx, E. Voet, J. Degrieck, W. Urbanczyk, P. Mergo, M. Beckers, and H. Bartelt, “Towards micro-structured optical fiber sensors for transverse strain sensing in smart composite materials,” *IEEE Sensors*, pp. 109–112, 2011.

[47] C. Sonnenfeld, S. Sulejmani, T. Geernaert, S. Eve, N. Lammens, G. Luyckx, E. Voet, J. Degrieck, W. Urbanczyk, P. Mergo, M. Becker, H. Bartelt, F. Berghmans, and H. Thienpont, “Microstructured optical fiber sensors embedded in a laminate composite for smart material applications,” *Sensors*, vol. 11, no. 3, pp. 2566–2579, 2011.

[48] S. Sulejmani, “Microstructured optical fiber Bragg grating-based sensors for shear strain measurements,” Vrije Universiteir Brussel, 2015.

[49] S. Acheroy, P. Merken, H. Ottevaere, T. Geernaert, H. Thienpont, and B. Francis, “Influence of measurement noise on the determination of the radial profile of the photoelastic coefficient in step-index optical fibers,” *Appl. Opt.*, vol. 52, no. 35, pp. 8451–8459, 2013.

[50] W. Primak, “Photoelastic constants of vitreous Silica and its elastic coefficient of refractive index,” *J. Appl. Phys.*, vol. 30, no. 5, pp. 779–788, 1959.

[51] L. Yan, “Performance Monitoring in Advanced Optical Fiber Networks,” in *Progress in Optical Fibers Research*, 1st ed., Z. Guo, Ed. New York: Nova Science Publishers, Inc, 2007, pp. 49–104.

[52] “G.691 : Optical interfaces for single channel STM-64 and other SDH systems with optical amplifiers.” [Online]. Available: https://www.itu.int/rec/T-REC-G.691/en.

[53] “G.657 : Characteristics of a bending-loss insensitive single-mode optical fibre and cable for the access network.” [Online]. Available: https://www.itu.int/rec/T-REC-G.657.

[54] J. Sakai and T. Kimura, “Birefringence and Polarization Characteristics of

Single-Mode Optical Fibers under Elastic Deformations," *IEEE J. Quantum Electron.*, vol. 17, no. 6, pp. 1041–1051.

[55] P. L. Chu, "Analytical method for calculation of stresses and material birefringence in polarization-maintening optical fiber," *J. Light. Technol.*, vol. 2, no. 5, pp. 650–661, 1984.

[56] J. Sakai and T. Kimura, "Birefringence Caused by Thermal Stress in Elliptically Deformed Core Optical Fibers," *IEEE J. Quantum Electron.*, vol. 18, no. 11, pp. 1899–1909, 1982.

Chapter 3. Measurement of the photoelastic constant C: state-of-the art and challenges

The values of the photoelastic constant C of silica glass optical fibers that can be found in literature are mostly consistent. However, many publications dealing with silica optical fiber sensors still use the value of C measured on bulk silica [1]. For polymer optical fibers, the situation is different. The values of C that have been reported for polymethyl methacrylate (PMMA), which is the most common material used to fabricate polymer optical fibers, are very dissimilar. Altogether, this calls for the need to develop an accurate measurement method to determine C of the optical fiber on the fiber itself. In the first section of this Chapter, we describe measurement methods that are mostly used to determine C in bulk material. The second section gives an overview of the methods proposed in the literature to measure C directly on the optical fibers themselves. In the third section, we first summarize the fabrication technologies typically used to fabricate silica and polymer optical fibers. Considering these manufacturing processes, we conclude on the need, not only to develop an accurate measurement method to determine C, but also to determine the radial dependence of C across the fiber section. We close this Chapter by summarizing the specific challenges associated with the measurement of the radial profile of the photoelastic constant.

3.1 Measurement of C in bulk material

3.1.1 C in bulk silica

Several techniques have been developed to measure the individual stress-optic coefficients or the photoelastic coefficient. A first and well-known method is based on interferometric measurements [1–3]. A cube-shaped

silica sample is placed in one arm of a Mach-Zehnder interferometer as illustrated in Figure 3-1. The crystal under test is immersed in index matching liquid to avoid scattering of light at the edges of the silica cube. The laser illuminates the cube with monochromatic light that is linearly polarized along either the x or y direction depending on the setting of the polarizer.

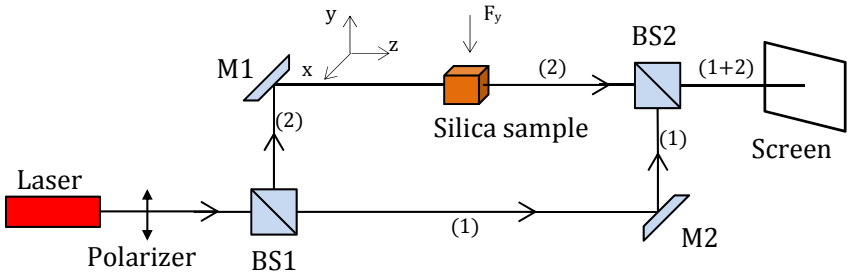

Figure 3-1: Basic Mach-Zehnder interferometer setup for measuring the photoelastic coefficient of silica. The laser beam is linearly polarized in the x or y direction by means of the polarizer. Beamsplitter 1 (BS1) divides the light into two beams, totally reflected by the mirrors M1 and M2. BS2 recombines the two beams. The interference fringes are visualized on the screen.

The incident polarized light beam is divided into two beams at the first beam splitter (BS1). Afterwards, each beam is totally reflected by mirrors M1 and M2. The two light beams will recombine after the second beamsplitter BS2 and produce an interference fringe pattern on the screen. The silica cube is loaded with a uniformly distributed vertical load F_y. The load induces uniaxial stress $\sigma_y = F_y/a^2$ in the sample, with a the length of the silica cube edge. In that particular case the expression of the stress-optic law becomes ((3.1)):

$$\begin{aligned} \Delta n_x &= n_x - n_0 = C_2 \sigma_y \\ \Delta n_y &= n_y - n_0 = C_1 \sigma_y \end{aligned} \tag{3.1}$$

Due to the stress-induced birefringence, the two orthogonal linear polarizations of light allowed to travel through the cube will experience a different refractive index and will therefore travel different optical path

lengths. The difference in optical path length is referred to as the retardance as described in Chapter 2. Equation (3.2) expresses the retardance for both linear polarization directions along x and y, and the ensuing phase-shift of the light beam. λ is the wavelength of the incident light.

$$\begin{cases} \delta_{zx} = \Delta n_x a = C_2 \sigma_y a \\ \delta_{zy} = \Delta n_y a = C_1 \sigma_y a \end{cases} \Rightarrow \begin{cases} \Delta\varphi_{zx} = \dfrac{2\pi}{\lambda} C_2 \sigma_y a \\ \Delta\varphi_{zy} = \dfrac{2\pi}{\lambda} C_1 \sigma_y a \end{cases} \tag{3.2}$$

Measuring the interference fringe shift between the pattern measured with the unloaded sample and the pattern obtained with the loaded sample for both directions of linear polarization therefore allows determining the individual stress-optic coefficients C_1 and C_2. This has resulted in a value of $C = -3{,}52 \times 10^{-12}$ Pa^{-1} for bulk fused silica measured at a wavelength of 644 nm [1] in 1959, which is still used as a reference value in many publications, essentially because the results are considered to feature a low uncertainty of 2%. That reference value is, for example, used by Bertholds et al. [4] to validate their method to measure transverse stress with an optical fiber Bragg grating based sensor. We refer to section 2.2 of Chapter 2 explaining the operation of fiber Bragg grating sensors. The authors of [5–7], for example, rely on that reference value to validate the simulated response of a highly birefringent microstructured optical fiber (see section 2.3) designed to be sensitive to pressure or transverse mechanical load. The authors of [1, 8] also comment on the wavelength dependence of C. The value of C decreases slightly with increasing wavelength, similarly to the refractive index wavelength dispersion [9, 10]. Note that in this PhD thesis, we do not analyze the wavelength dependence of C, but in principle, our method can be applied to measure C at any wavelength for which the sample is transparent.

Other techniques to analyze the optical properties of photoelastic materials have been proposed in literature. One method relies on the measurement of the optical path differences between two plane waves to measure the stress-induced birefringence [11–13]. Others exploit the

caustic effect [14, 15], i.e. the analysis of the path change dictated by the stress field of a specimen illuminated by a monochromatic light beam. The reflected or transmitted rays generate a bright curve on a reference screen, the so-called 'caustic'. The analysis of the caustics yields information on the stress conditions and on the birefringence in the specimen. Other methods rely on birefringence analysis with circular polariscopic arrangements [16–20]. The analysis of the evolution of the isochromatic patterns allows studying the birefringence of transparent material.

3.1.2 C in polymer material

The measurement techniques described in the previous section can be applied to all kinds of transparent material, and therefore also to transparent polymer specimens. In contrast to the case of silica, only a few references exist that report about the measurement of C. In addition, the value of C appears to vary considerably. For example, the values of C measured on bulk and thin film polymethyl methacrylate (PMMA) range from -1.08×10^{-10} Pa^{-1} to 5.3×10^{-12} Pa^{-1} [21–26]. Information about the wavelength dependence of C in polymer material is also available in [27]. There can be several reasons for the large spread in reported values of C in polymers. In [25] the authors demonstrate that PMMA can have a negative, zero or positive birefringence. The sign and the value of the photoelastic constant depend on the presence and on concentration of dopants in the polymer. They also demonstrate that the photoelastic constant depends on the orientational birefringence caused by the orientation of the polymer chains in the cured polymer sample. Furthermore and by carefully selecting the copolymers and their concentration, they are able to achieve a polymer with a photoelastic constant C almost equal to 0 Pa^{-1}[22].

3.2 Techniques proposed to determine C of optical fibers

We can distinguish between two approaches that have been followed to measure the photoelastic coefficient directly on an optical fiber. A first category of methods analyses the light guided through the fiber. The effect of an applied stress (either twist-induced stress or stress resulting from elongation of the fiber) is then analyzed by means of a polarimetric or interferometric measurement. A first of such methods has determined the

mean value of the photoelastic coefficient by twisting the fiber and by measuring the stress-induced birefringence [2, 8, 28]. The birefringence is measured in a polarimetric setup to determine the rotation of linearly polarized light launched in the fiber. The principle is illustrated in Figure 3-2. The advantage of this technique resides in the ease of implementation and it also requires a minimal investment in hardware components. The main issue one faces with this method is to ensure a uniform twist of the fiber without bends. The fiber ends should also be clamped with minimal induced stress. This approach allows measuring one mean value of C but not determining a radial dependence of the photoelastic coefficient. In addition, the measurement technique integrates possible changes in C over the length of the measured fiber portion.

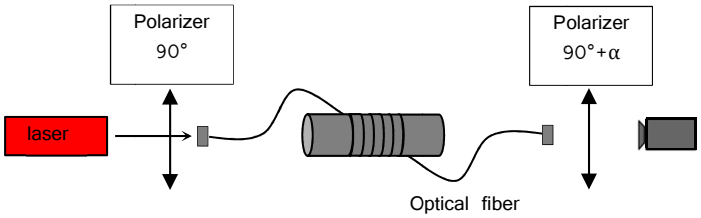

Figure 3-2: Schematic of a polarimetric setup for measuring the rotation angle α of linearly polarized light injected into an optical fiber to determine the twist-induced birefringence [3].

The second category determines the photoelastic constant by measuring the retardance of a linearly polarized light beam that transversely illuminates a portion of the fiber [29, 30]. This approach is similar to the technique proposed in [31, 32] to measure the refractive index profile – and its wavelength dependence – in an optical fiber. The latter would also enable the measurement of the retardance under a microscope arrangement. It essentially inspired our setup to measure the radial profile of C in an optical fiber with adequate radial resolution. However, the relation between the measurement and the eventual determination of C is not straightforward. Several mathematical operations

are necessary to calculate C based on the measurement results. Our setup and measurement principle are discussed in detail in Chapter 4.

3.3 Overview of the production process of optical fibers

The measurement techniques described in section 3.2 essentially rely on the hypothesis that C is constant throughout the optical fiber's cross-section. Due to the particular fabrication process of optical fibers, making such an assumption is not necessarily correct [2]. Fabricating a fiber involves several steps that could potentially alter the value and the radial distribution of the photoelastic constant. To illustrate this we briefly address the most common fabrication processes for glass optical fibers and polymer fibers.

3.3.1 Production of glass optical fibers

Fabricating optical fibers involves fabricating a preform that contains doping elements to form a core and cladding structure and thermal drawing of the fiber from this preform [33].

Doping of glass is essentially required to control the refractive index of the glass, but may also be needed, for example, to provide for the required gain medium when fabricating optical fiber lasers. Various vapor deposition techniques allow the fabrication of preforms with very low impurity levels and controlled doping levels [34]. The most common dopant used to increase the refractive index of the fiber core is germanium. Fluorine, on the other hand reduces, the refractive index of silica and can be added to the cladding to allow the use of pure silica cores. Typically, the refractive index difference between the core and cladding is 0.36%. Once the preform is manufactured, the glass fiber is drawn from this preform using a high-temperature furnace in a tower setup [35, 36]. The main elements of the drawing tower are illustrated in Figure 3-3. During the drawing, the preform is heated to an optimum temperature, typically 1900°C to melt the silica glass. The fiber is pulled and wound around the winding drum. During the draw, the temperature of the preform has to be very stable to ensure a uniform draw tension. For the same drawing tension, higher speeds are obtained with an increase of the temperature of the furnace. The consequence is a change of the frozen-in thermal stress distribution that

will induce undesired birefringence in the fiber. The drawing parameters (temperature, drawing tension) have a direct influence on the quality of the optical fibers and thus have to be chosen properly to avoid dispersion induced by birefringence in the fiber [37]. The draw speed (mostly between 10 and 20 meters per second) depends on the desired final fiber diameter. The cladding diameter of glass optical fibers is typically 125 µm.

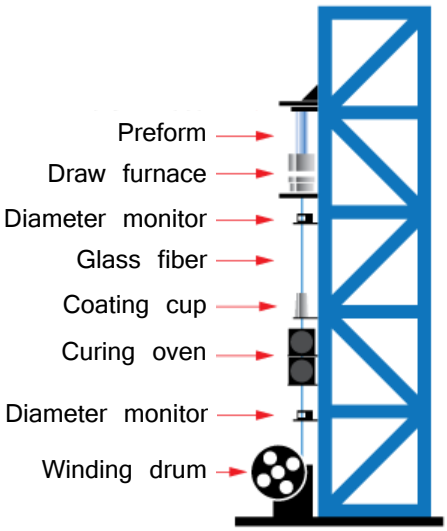

Figure 3-3: Illustration of a drawing tower. The preform is heated in the furnace. The diameter monitor allows fine-tuning the drawing speed to achieve the desired fiber diameter. A protective coating layer is applied as the fiber passes through the coating cup. The curing oven allows to harden the coating around the fiber. Before the fiber is wound around the drum, its diameter is monitored again [38].

To conclude, one can understand that an optical fiber consisting of a core and cladding structure that are essentially made from different materials, which have different coefficients of thermal expansion leading to the existence of a residual stress profile, and which are also different from typical bulk pure silica material, may feature a value of C that is not constant across the section of the fiber and that is likely different from bulk pure silica. In addition, optical fibers are sometimes post-processed to enable them to operate as a sensor, for example by means of inscribing a

fiber Bragg grating, which could potentially locally alter the value of C as well.

3.3.2 Production of polymer optical fibers

POFs are usually made from polymethyl methacrylate (PMMA), polystyrene (PS) or polycarbonate (PC). More recently other polymers such as TOPAS® or CYTOP® have been used as well [39]. We give a short overview of the main differences in characteristics between the polymer fibers and their silica counterparts. Most plastic fibers are large core step-index fibers. The core diameter varies from 85 μm to more than 3mm. This large diameter compared to silica fibers makes them much easier to handle. The major drawback is the high attenuation of the polymer fibers compared to the silica fibers. Each polymer comes with its own advantages and drawbacks [40, 41]. For telecommunication applications, PMMA POFs offer a relatively low loss in visible and near-infrared regions, which makes them the most common POFs on the market. The most commercially available POF is a PMMA based large-core step-index POF, with a minimal attenuation of 70 dB/km at a wavelength of 500nm. The attenuation is much higher in the 1300 nm and 1550 nm windows, corresponding to the most widely used telecommunication windows of silica fibers. Fluorinated graded index plastic fibers allow to operate also in these transmission windows, but these fibers are relatively expensive and less commercially available.

The two main techniques used for making polymer fibers are the thermal drawing process and the extrusion process. Drawing the fiber from the preform relies on the same principle as for the silica fibers. However, obtaining a transparent and homogenous polymer preform is not straightforward. After polymerization, several temperature treatments are necessary to purify the polymer from the remaining volatiles used to initiate the polymerization and to eliminate bubbles from the preform [39]. Afterwards the preform is placed a few days in a 95°C oven to relieve the stresses present in the polymer. This process is called the thermal 'annealing' process. Once the preform is ready, it is heated up to 240°C in the furnace of the drawing tower. The main advantage of the drawing process is its flexibility and the high quality of the produced fibers. The

drawbacks are the low productivity and the high production costs for large quantities [40]. Small-core and specialty polymer fibers such as microstructured POF are fabricated with such a drawing process.

The extrusion process allows making polymer fibers in a more economical way and is also amenable to high volume processing. Compared to the drawing process, the extrusion process produces POFs directly from monomers, either continuously or in batches. The principle of continuous extrusion process is illustrated in Figure 3-4. The raw materials, the monomer and the initiators are pumped continuously into the polymerization reactor. When the composition in the reactor reaches 80% of polymer material, it is directed to the screw extruder, which conveys the polymer material to the spinning nozzle where the fiber core is formed. The cladding is either directly applied in the same spinning nozzle also using an extrusion process, which is called co-extrusion, either the cladding material is applied later in a downstream process.

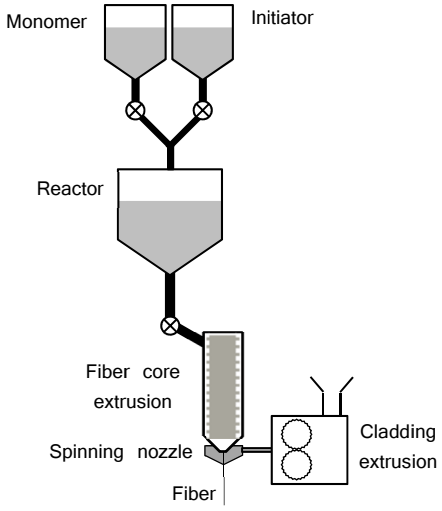

Figure 3-4: Illustration of a continuous extrusion apparatus. The monomer and initiator reservoirs can be continuously fed. The core of the fiber runs into a second chamber and afterwards through a nozzle where the cladding is coated onto the fiber, also using an extrusion process, called co-extrusion [39, 40].

In the batch extrusion process the monomer and reactor vessels are sealed to avoid external contamination. One obtains a closed system that ensures the material remains clean during the fabrication process. However, for the batch extrusion process the amount of fiber that can be drawn is limited by the size of the reactor chamber. This process is typically used in laboratories or in pilot-plants. Most large-core step-index commercially available POFs are produced with the continuous extrusion technique.

To conclude, and similarly to the case of the silica fibers, the production processes of POFs may lead to values of C that differ from that of bulk material and that are not uniform over the POF cross-section. The problem may even be exacerbated in POFs considering the multitude of different materials available, the variety of pre-processing and conditioning methods used, the alignment of polymer chains during fiber drawing leading to an intrinsic form of structural anisotropy, and the peculiar characteristics of polymers themselves, including their visco-elastic properties and their peculiar response to thermal treatments. Furthermore, POFs also feature very different photosensitivity properties than doped glass fibers, which may also affect how their structure and therefore C is altered following exposure to UV light for the fabrication of Bragg gratings in such fibers.

3.4 Challenges towards the determination of C

The previous paragraphs have illustrated that the manufacturing process of both silica end polymer fibers, and sensors made thereof, involves several production steps that can potentially alter the value of the stress-optic constant in comparison with bulk material. The transformation of the material from solid to liquid and back to solid implies large temperature variations. Drawing the fiber can potentially add a random residual stress distribution generating birefringence in the fiber if this operation is not executed carefully. In [42], for example, C has been measured in PMMA fibers and its value has been found to depend both on the drawing conditions and on the annealing of the fiber. The values obtained are between 1.5×10^{-12} Pa^{-1} and 4.5×10^{-12} Pa^{-1}. This may point at the necessity to measure C for every different type of POF. The addition of dopants also influences the material characteristics and conveys different

properties to the core and cladding of the fibers. Therefore, the value of C should not only be measured accurately on the fiber directly, but knowledge of its distribution in the fiber cross-section is equally important in order to allow for accurate predictions of the response of an optical fiber sensor to mechanical load.

This thesis therefore focuses on the two following objectives.

The first objective is to obtain a setup that enables a reliable measurement of the photoelastic coefficient directly on the optical fiber. The method we implement relies on the theory of photoelasticity. We aim to determine the retardance in a laterally illuminated fiber as described in section 3.2. The fiber is installed in a polarimetric setup and the retardance is measured according to the Sénarmont compensation method that we will describe extensively in Chapter 4.

The second objective is to enable the measurement of the radial distribution of C in the cross-section of the optical fiber. To do so we have to build the setup mentioned above in a polarizing microscope arrangement to achieve the optical resolution required to obtain micron-level spatial resolution for the radial profile C(r).

Achieving these objectives requires us to tackle a number of specific challenges.

First, as photoelasticity requires the retardance to be measured for a known applied axial tensile stress, we have to take care when designing the mechanism to apply the tensile stress to the optical fiber under test, more specifically to exclude any radial dependence of the tensile stress in the fiber.

Second, since the fiber experiencing tensile stress is laterally illuminated, we will obtain a projection of the stress-induced retardance along the fiber diameter, without immediate information linking the retardance to a specific position along the fiber radius. To recover that information we need to use a mathematical integral transform known as the 'inverse Abel transform', which allows calculating the radial distribution of an axisymmetric function given the projection of that function. In our specific case, the projection of that function is the measured retardance. We

will demonstrate in Chapter 4 that the inverse Abel transform of the retardance is proportional to the applied tensile stress σ_z multiplied by the radial profile of the photoelastic coefficient C(r). The challenge is then to develop the most suitable algorithm to calculate the inverse Abel transform such that we achieve the most reliable results. The result should be obtained with a sufficient spatial resolution to determine a correct average profile of the photoelastic coefficient C(r). In addition, the algorithm should be able to cope with unavoidable measurement noise. As we will describe, this noise may contribute in significant amounts to the uncertainty with which C(r) can be determined.

The third challenge we face is to validate our measurement method by measuring C and C(r) using actual fiber samples. This requires first finding the appropriate parameters that enable correctly calculating the inverse Abel transform and carrying out the measurements and calculations for different types of silica optical fibers with different core diameters, and second comparing these results with values for the photoelastic coefficient that have been published in literature. If these values are consistent then we will be able to claim that we achieve reliable results and that our method is validated.

Once the technique is validated, the fourth challenge is to adapt and extend our measurement and calculation technique to polymer optical fibers. This implies selecting adequate candidate POFs and adapting the tensile loads enabling the measurements to appropriate levels. Furthermore, and in order to highlight the peculiar properties of POFs compared to their silica counterparts when considering their use in optical fiber sensing, we will have to conduct a study of the effect of thermal treatments on the value of the photoelastic constants of POF.

3.5 Summary and Conclusion

In this Chapter we shortly reviewed the measurement techniques that have been applied to determine the photoelastic coefficient C in bulk silica and polymer material. The majority of these techniques rely on an interferometric measurement setup that allows determining the stress-induced retardance and from there the photoelastic coefficient in

transparent material. The methods proposed in literature to determine the mean value of C directly in optical fibers essentially rely also on interferometric measurement principles using polarized light that is either launched and guided in the optical fiber, or that transversely illuminates the fiber. Whilst the literature proposes methods to determine the residual stress distribution in optical fibers, so far no method has been described in literature to measure the radial profile of the photoelastic constant C(r) across a transverse section of the fiber.

The ability to measure this radial profile C(r) is nevertheless important. Looking briefly into the fabrication methods for both glass and polymer optical fibers, we have illustrated that it is not only important to determine the photoelastic coeffcient directly on the optical fibers instead of using bulk materials, but that it is also not straightforward to assume this photoelastic coefficient to be constant across the fiber.

To enable the measurement of the radial profile C(r), we propose to transversely illuminate the optical fiber in a polariscopic arrangement. The implementation of this arrangement under a microscope should allow us to achieve sufficient spatial optical resolution of the order of a few microns. This setup can then be used to measure the retardance of the light travelling through the fiber when the latter experiences uniform tensile stress and from there calculate C(r), as well as the mean value of C. On the way to do so, we have to tackle the following specific challenges:

- to design and build a setup to measure the radial profile of the photoelastic coeffcient C(r) directly onto the optical fibers providing for sufficient optical resolution while exposing the fiber to a controlled and uniform axial stress state;
- to extract C(r) from the measured retardance profile by means of the inverse Abel transform and to develop adequate algorithms enabling the calculation of this transform with sufficient robustness against the influence of unavoidable measurement noise;
- to validate our method by determining C(r) in actual fiber samples and comparing results with what is available in literature.
- to extend the method to polymer optical fibers and investigate the differences, if any, with silica optical fibers.

The next Chapters describe in detail how we tackled each of these challenges.

Bibliography

[1] W. Primak, "Photoelastic constants of vitreous Silica and its elastic coefficient of refractive index," *J. Appl. Phys.*, vol. 30, no. 5, pp. 779–788, 1959.

[2] A. Bertholds and B. Dändliker, "Determination of the individual strain-optic coefficients in single-mode optical fibers," *J. Light. Technol.*, vol. 6, no. n°1, pp. 17–20, 1988.

[3] A. Bertholds and R. Dändliker, "Deformation of single-mode optical fibers under longitudinal stress," *J. Light. Technol.*, vol. LT-5, no. 7, pp. 895–900, 1987.

[4] R. J. Espejo and S. D. Dyer, "Transverse-stress fiber Bragg grating sensor with high spatial resolution and temperature stability," *J. Light. Technol.*, vol. 25, no. 7, pp. 1777–1785, 2007.

[5] T. Geernaert, G. Luyckx, and E. Voet, "Transversal load sensing with fiber Bragg gratings in microstructured optical fibers," *IEEE PHOTONICS Technol. Lett.*, vol. 21, no. 1, 2009.

[6] S. Sulejmani, C. Sonnenfeld, T. Geernaert, F. Berghmans, H. Thienpont, S. Eve, N. Lammens, G. Luyckx, E. Voet, J. Degrieck, W. Urbanczyk, P. Mergo, M. Beckers, and H. Bartelt, "Towards micro-structured optical fiber sensors for transverse strain sensing in smart composite materials," *IEEE Sensors*, pp. 109–112, 2011.

[7] T. Martynkien, G. Statkiewicz-Barabach, J. Olszewski, J. Wojcik, P. Mergo, T. Geernaert, C. Sonnenfeld, A. Anuszkiewicz, M. K. Szczurowski, K. Tarnowski, M. Makara, K. Skorupski, J. Klimek, K. Poturaj, W. Urbanczyk, T. Nasilowski, F. Berghmans, and H. Thienpont, "Highly birefringent microstructured fibers with enhanced sensitivity to hydrostatic pressure.," *Opt. Express*, vol. 18, no. 14, pp. 15113–15121, 2010.

[8] A. J. Barlow and D. N. Payne, "The stress-optic effect in optical fibers," *IEEE J. Quantum Electron.*, vol. QE-19, no. 5, pp. 834–839, 1983.

[9] J. W. Fleming and D. L. Wood, "Refractive index dispersion and related properties in fluorine doped silica.," *Appl. Opt.*, vol. 22, p. 3102, 1983.

[10] R. Priestley, "Birefringence dispersion in fused silica for DUV

lithography," in *Optical Microlithography XIV, Proceedings of SPIE Vol. 4346*, pp. 1300–1305, 2001.

[11] J. B. Saunders, "Measurement of Wave Fronts Without a Reference Standard : Part 2 . The Wave Front Reversing Interferometer," *J. Res. Natl. Bur. Stand. B.- Math. Math. Phys.*, vol. 66B, no. 1, pp. 29–46, 1962.

[12] J. B. Saunders, "Some Applications of the Wave Front Shearing Interferometer," *J. Res. Natl. Bur. Stand. - B. Math. Math. Phys.*, vol. 69C, no. 4, pp. 245–249, 1965.

[13] S. L. B. Kramer, G. Ravichandran, and K. Bhattacharya, "Transmission wavefront shearing interferometry for photoelastic materials.," *Appl. Opt.*, vol. 48, pp. 2450–2460, 2009.

[14] D. D. Raftopoulos and S. V Kartalopoulos, "Evaluation of the stress-optical coefficients of transparent solid plates using interferometry.," *Appl. Opt.*, vol. 18, no. 17, pp. 2975–8, 1979.

[15] L. Wang, K. Li, and S. Sanusei, "Advancement of Optical Methods in Experimental Mechanics, Volume 3," *Conf. Proc. Soc. Exp. Mech. Ser.*, vol. 3, no. Dic, pp. 289–297, 2014.

[16] A. S. Redner, "Photoelastic measurements by means of computer-assisted spectral-contents analysis," *Exp. Mech.*, vol. 25, no. June, pp. 148–153, 1985.

[17] A. S. Voloshin and A. S. Redner, "Automated Measurement of Birefringence : Development and Experimental Evaluation of the Techniques," no. September, pp. 252–257, 1989.

[18] T. Kihara, "A Measurement Method for Birefringent Plate using Elliptically Polarized Light," pp. 255–263, 2006.

[19] N. Sinha, "Normalised dispersion of birefringence of quartz and stress optical coefficient of fused silica and plate glass," *Phys. Chem. Glas.*, vol. 19, no. 4, pp. 69–77, 1978.

[20] T. Y. Chen and T. F. Chen, "Whole-field digital measurements of isochromatics and isoclinics in photoelastic coatings," *Opt. Lasers Eng.*, vol. 31, pp. 325–338, 1999.

[21] A. Tagaya, L. Lou, Y. Ide, Y. Koike, and Y. Okamoto, "Improvement of the

physical properties of poly(methyl methacrylate) by copolymerization with N-pentafluorophenyl maleimide; zero-orientational and photoelastic birefringence polymers with high glass transition temperatures," *Sci. China Chem.*, vol. 55, no. 5, pp. 850–853, 2012.

[22] A. Tagaya, H. Ohkita, T. Harada, K. Ishibashi, and Y. Koike, "Zero-birefringence optical polymers," *Macromolecules*, vol. 39, pp. 3019–3023, 2006.

[23] R. M. Waxler, D. Horowitz, and A. Feldman, "Optical and physical parameters of Plexiglas 55 and Lexan," *Appl. Opt.*, vol. 18, no. 1, pp. 101–104, 1979.

[24] W. Xu, X. F. Yao, H. Y. Yeh, and G. C. Jin, "Fracture investigation of PMMA specimen using coherent gradient sensing (CGS) technology," *Polym. Test.*, vol. 24, pp. 900–908, 2005.

[25] H. Ohkita, K. Ishibashi, D. Tsurumoto, a. Tagaya, and Y. Koike, "Compensation of the photoelastic birefringence of a polymer by doping with an anisotropic molecule," *Appl. Phys. A*, vol. 81, no. 3, pp. 617–620, 2005.

[26] F. Ay, A. Kocabas, C. Kocabas, A. Aydinli, and S. Agan, "Prism coupling technique investigation of elasto-optical properties of thin polymer films," *J. Appl. Phys.*, vol. 96, no. 12, pp. 7147–7153, 2004.

[27] G. Golojuch, U. Hollenbach, T. Mappes, J. Mohr, A. Urbanczyk, and W. Urbanczyk, "Investigation of birefringence in PMMA channel waveguides inscribed with DUV radiation," *Meas. Sci. Technol.*, vol. 19, no. 2, p. 25304, 2008.

[28] M. P. Varnham, S. B. Poole, and D. N. Payne, "Thermal stress measurements in optical-fibre preforms using preform-profiling techniques," *Electron. Lett.*, vol. 20, no. 25/26, pp. 1034–1035, 1984.

[29] N. Lagakos and R. Mohr, "Stress optic coefficient and stress profile in optical fibers," *Appl. Opt.*, vol. 20, no. 13, pp. 2309–2313, 1981.

[30] F. Berghmans, H. Thienpont, P. Van Daele, P. Dubruel, W. Urbanczyk, J. Rayss, D. J. Webb, J. Vlekken, K. Kalli K. Sugden, "Photonics skins for optical sensing: highlights of the PHOSFOS Project," *presented at the Proc. SPIE, 20th International Conference on Optical Fibre Sensors*, vol.

75030B-1–75030B-4, 2009.

[31] A. D. Yablon, “Multi-wavelength optical fiber refractive index profiling by spatially resolved Fourier transform spectroscopy,” *J. Light. Technol.*, vol. 28, no. 4, pp. 360–364, 2010.

[32] A. D. Yablon, “New transverse techniques for characterizing high-power optical fibers,” *Opt. Eng.*, vol. 50, no. 111603-1–6, 2011.

[33] Chu and Whitbread, “Measurement of stresses in optical fiber and preform,” *Appl. Opt.*, vol. 21, no. 23, pp. 4241–4245, 1982.

[34] L. Tingye, Ed., *Optical Fiber Communications: Fiber Fabrication*. Elsevier, 2012.

[35] A. Bjarklev, *Optical Fiber Amplifiers: Design and System Applications*, First Edit. Boston-London: Artech House, INC, 1993.

[36] A. Bjarklev, J. Broeng, and A. S. Bjarklev, *Photonic Crystal Fibres*. Kluwer Acadmic Publisher, 2003.

[37] M. Tacca, M. Ferrario, P. Boffi, and M. Martinelli, “Drawing parameters optimization for birefringence reduction in optical fibers,” *Opt. Commun.*, vol. 283, no. 9, pp. 1773–1776, 2010.

[38] “Specialty Optical Fiber Manufacturing.” [Online]. Available: https://www.thorlabs.com/NewGroupPage9_PF.cfm?ObjectGroup_ID=6832.

[39] M. G. Kuzyk, *Polymer fiber optics: materials, physics, and applications*. CRC Press, 2006.

[40] M. Beckers, T. Schlüter, T. Vad, T. Gries, and C.-A. Bunge, “An overview on fabrication methods for polymer optical fibers,” *Polym. Int.*, vol. 64, no. 1, pp. 25–36, 2015.

[41] Y. Jin and A. M Granville, “Polymer Fiber Optic Sensors – A Mini Review of their Synthesis and Applications,” *J. Biosens. Bioelectron.*, vol. 7, no. 1, pp. 1–11, 2016.

[42] M. C. Szczurowski, T. Martynkien, G. Statkiewicz-Barabach, L. Khan, D. J. Webb, C. Ye, J. Dulieu-Barton, and W. Urbanzyck, “Measurements of stress-optic coefficient and Young’s modulus in PMMA fibers drawn under different conditions,” in *SPIE Photonic Crystal Fibers IV, Vol*

7714, pp. 1–8, 2010.

Chapter 4. Method for determining the radial profile of the photoelastic coefficient in optical fibers

In this Chapter[1] *we describe the theoretical bases of the method that we have developed to characterize the photoelastic constant directly on the optical fiber. We first demonstrate that measuring the retardance profile of the laterally illuminated fiber as a function of applied mechanical load allows deriving the photoelastic coefficient. In section 4.2 we present the measurement setup to obtain the retardance profile of the optical fiber. Section 4.3 presents the algorithms that we have elaborated to compute the inverse Abel transform of the retardance R(y).*

4.1 Theoretical development

In Chapter 2 we introduced the stress-optic law which gives the relation between the stress distribution in a fiber section and the refractive index in that section. The photoelastic coefficient is the material parameter that relates refractive index and stress distribution. The measurement method is based on [1], which describes how the radial distribution of the refractive index profile can be determined by measuring the phase shift of light traversing the fiber. The fiber, immersed in an index matching liquid, is transversely illuminated with a vertically (linearly) polarized plane wave with a wave vector that is parallel to the x-axis (see Figure 4-1). Since we immerse the fiber in index matching fluid during the measurement, the direction of the wave vector does not change at the boundaries of the optical fiber. Due to the stress-induced birefringence of the fiber, the

[1] The results presented in this Chapter have been partly published in [26, 29, 30]

electric field vector of the associated electromagnetic wave splits into two orthogonal linearly polarized components along the directions of the principal stress axes, i.e. in the y and z direction [2, 3]. Note that if we assume the fiber to be axisymmetric and considering its cylindrical structure, we can state that the principal axes of stress coincide with the cylindrical coordinates of the fiber with unit vectors u_r, u_θ, u_z.

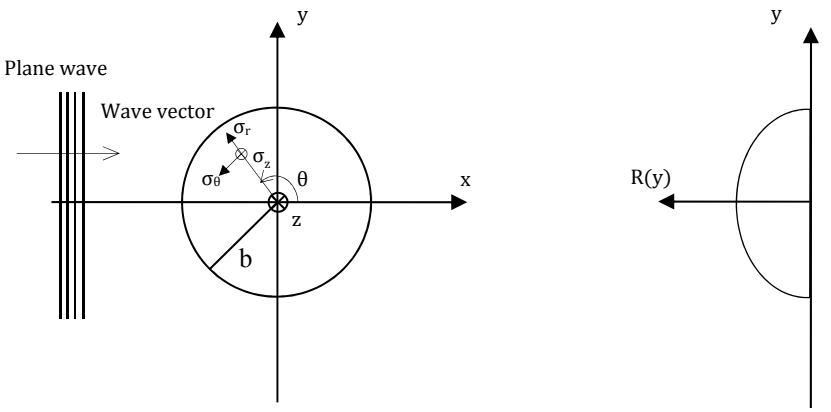

Figure 4-1: Illustration of a transversely illuminated optical fiber (left) and of the resulting retardance profile R(y) (right). b is the radius of the fiber, σ_r, σ_θ and σ_z are respectively the radial, angular and axial principal axes of stress. The z-axis is taken along the fiber length with a direction entering the page.

When exiting the fiber, these components have experienced a different phase-shift and consequently one can observe a retardance R. If σ_y, σ_z are the stress components in the y and z directions, and if one assumes that the ray trajectory is always parallel to the x-axis, the expression of the retardance becomes equation (4.1) according to equation (2.11) from Chapter 2:

$$R = C(\sigma_z - \sigma_y)d \tag{4.1}$$

with d the distance travelled by the ray traversing the fiber. The distance d, and therefore also R, vary along the y-coordinate, i.e. R = R(y). The retardance along the y-axis is expressed as equation (4.2) [4].

$$R(y) = \int_{-\sqrt{b^2-y^2}}^{\sqrt{b^2-y^2}} C(\sigma_z - \sigma_y)dx \tag{4.2}$$

In [5] the authors demonstrate that the second term of equation (4.2) vanishes in long axisymmetric cylinders as a result of the boundary conditions and of the equilibrium in the material in the y direction and therefore equation (4.2) becomes:

$$R(y) = \int_{-\sqrt{b^2-y^2}}^{\sqrt{b^2-y^2}} C\sigma_z dx \tag{4.3}$$

Equation (4.3) can be rewritten in cylindrical coordinates to yield equation (4.4):

$$R(y) = 2\int_{y}^{b} C\frac{\sigma_z(r)rdr}{\sqrt{r^2-y^2}} \tag{4.4}$$

The last expression has the form of the forward Abel transform [6]. The radial distribution of the stress can hence be obtained by using the inverse Abel transform of (4.4):

$$\sigma_z(r) = -\frac{1}{\pi C}\int_{r}^{b} \frac{dR(y)/dy}{\sqrt{y^2-r^2}}dy \tag{4.5}$$

The forward Abel transform allows computing the projection of an axially symmetric radial function onto a plane. The inverse Abel transform can then be used to calculate the axisymmetric radial function from a projection of that function. For instance, in microscopy some stereology models make use of the Abel inversion to acquire 2D structural information from one dimensional measurements [7, 8]. Transforming equation (4.5) in

equation (4.6) shows that C is the regression coefficient linking the axial load $\sigma_z(r)$ and the inverse Abel integral of the retardance R(y).

$$\sigma_z(r).C = -\frac{1}{\pi}\int_r^b \frac{dR(y)/dy}{\sqrt{y^2 - r^2}}\,dy \tag{4.6}$$

Knowledge of the axial load $\sigma_z(r)$ and of the corresponding measured retardance R(y) therefore allows determining the radial profile of the photoelastic coefficient C.

In the following sections of this Chapter we describe the method that we propose to measure the retardance R(y) directly on the fiber. We then introduce the algorithms that we have developed to compute the inverse Abel transform of the retardance R(y).

4.2 Retardance measurement

4.2.1 Sénarmont compensation method

In the previous section we have shown that the first step towards the determination of the photoelastic coefficient is the measurement of the retardance profile of a transversely illuminated optical fiber. Several methods are available to measure the retardance, such as for example the Brace-Köhler compensator or the Two Waveplate Compensation (TWC) method [9, 10]. Both methods are very accurate, but they can only be applied when measuring small retardance values unless the sample can be rotated, which is difficult to implement in our case since we want to apply tensile stress to the fiber. We therefore rather opted for the Sénarmont compensation method to determine the retardance of the fiber [11–13].

The Sénarmont compensation method relies on the circular polariscope measurement setup, but with one quarter-wave plate only inserted between the sample and the analyzer [3, 11]. The arrangement of the optical elements is illustrated in Figure 4-2. The optical fiber sample is placed with its optical axis at 45° with respect to the polarization direction of the polarizer. Initially, the polarizer and analyzer are crossed. A quarter-wave plate parallel with the polarizer is positioned between the sample and

the analyzer. The method consists of finding a minimum of intensity by rotating the analyzer in order to determine the sample retardance [14, 15].

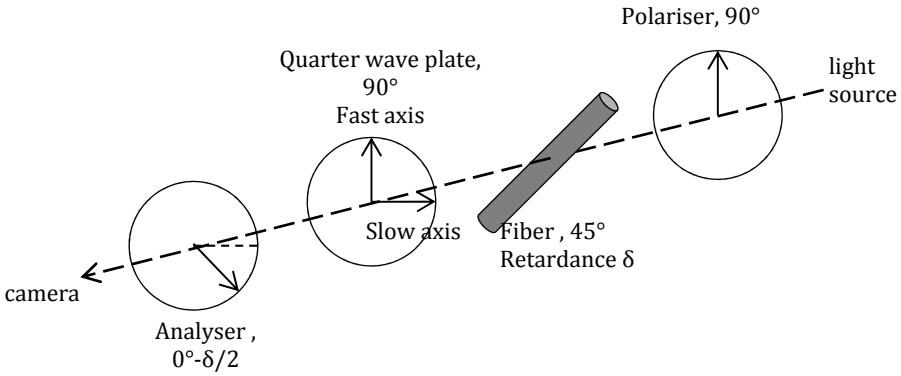

Figure 4-2: Illustration of a basic optical element arrangement for the Sénarmont compensation setup. The orientation of the polarization axes of the elements are mentioned in the figure.

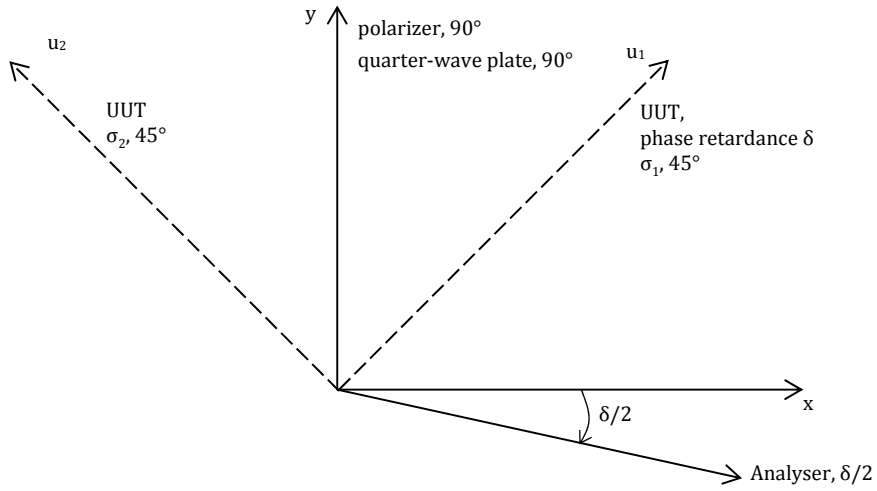

Figure 4-3: The axes system associated with the Sénarmont compensation method. The principal axes of stress of the sample, $u_1$and u_2, (Unit Under Test, UUT) are oriented at an angle of 45° with respect to the polarizer and quarter-wave plate orientation. Initially, the analyser is perpendicular to the polarizer direction.

Figure 4-3 shows the axes system associated with each optical element of the setup. The polarization directions of the polarizer and analyzer are respectively y and x. The quarter-wave plate is parallel with the polarizer. The principal stress-directions of the optical fiber u_1 and u_2, which coincide with the optical axis direction u_z and the radial direction u_r of the fiber section, are aligned at an angle of 45° from the x-axis. The sample produces a phase retardation of δ. Initially the polarization direction of the analyzer is perpendicularly to the polarizer. We utilize Jones calculus to determine the polarization direction and the intensity of the light at the exit of the setup [3, 12, 16, 17], as seen by the analyzer. The Jones vector $\mathbf{j}_A$ is calculated in the axes system of the analyzer, after passing through the optical system (equation (4.7)):

$$\boldsymbol{j}_A = e^{-i\delta/2}\begin{bmatrix} -i & 0 \\ 0 & 1 \end{bmatrix} \times \begin{bmatrix} \cos\frac{\delta}{2} & i\sin\frac{\delta}{2} \\ i\sin\frac{\delta}{2} & \cos\frac{\delta}{2} \end{bmatrix} \times \begin{bmatrix} 0 & 0 \\ 0 & 1 \end{bmatrix} \times \begin{bmatrix} 0 \\ 1 \end{bmatrix} \tag{4.7}$$

$$\boldsymbol{j}_A = e^{-i\delta/2}\begin{bmatrix} \cos(\frac{\pi}{2} - \frac{\delta}{2}) \\ \sin(\frac{\pi}{2} - \frac{\delta}{2}) \end{bmatrix} \tag{4.8}$$

The sequence of the matrices of equation (4.7) is given by the order of the optical elements illustrated in Figure 4-2. The right-most vector of (4.7) corresponds to vertically polarized light passing through the polarizer. The latter ensures that light is perfectly vertically (linearly) polarized before entering the sample. Note that the light entering the system must not be polarized since the polarizer takes care of this. The second matrix of equation (4.7) shows that the sample transforms the linearly polarized input light into elliptically polarized output light. The quarter-wave plate transforms the elliptical polarized light back to linear polarized light. Calculating equation (4.7) yields equation(4.8). The linear polarization direction has rotated with $\delta/2$ radians compared to the original vertically polarization direction. To determine the angle $\delta/2$, the analyzer should be rotated perpendicularly to that direction to obtain extinction of the light behind the analyzer. The retardance R associated to the measured phase retardance δ is then determined using equation (4.9).

$$R = \frac{\lambda \times \delta}{2\pi} \tag{4.9}$$

In conclusion, the Sénarmont compensation method allows determining the retardance R of the sample for monochromatic light with a wavelength λ.

4.2.2 Full-field Retardance measurement

The Sénarmont compensation arrangement in a classical optical setup using a single photodetector placed behind the analyzer allows determining the retardance at a single location defined by the width of the illuminating beam. To achieve a full-field view of the retardance of a transversally illuminated fiber we extended this principle by using a polarization microscope. The setup with the microscope arrangement is illustrated in Figure 4-4. A red filter is used to obtain monochromatic light with a wavelength of 633 nm. The bandwidth of the filter is 26 nm. The fiber is oriented at 0°, the polarizer and λ/4 plate are aligned at 45° relative to the fiber. The analyzer is initially set at 135°. We apply a predefined axial load to the fiber using an external loading system to change the relative retardance. The orientation of the linearly polarized light at the output of the λ/4 plate changes.

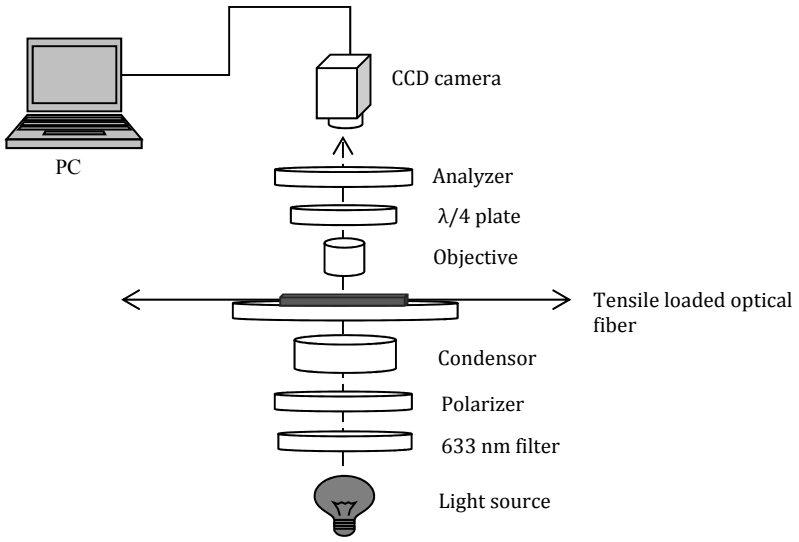

Figure 4-4: Polarization microscope set-up to measure the full-field retardance profile using the Sénarmont compensation method. To obtain a controlled tensile stress, a predefined axial load is applied to the fiber using an external loading system.

The analyzer is then rotated perpendicularly to that direction, which results in the extinction of the light at the output of the analyzer. Due to the high spatial resolution of the microscope, extinction is not obtained for each pixel at the same orientation of the analyzer. The angular range of rotation of the analyzer θ_{Atot} is chosen to achieve extinction for every pixel in the field of view of the microscope. A CCD camera records an image for each position of the analyzer θ_A in that range. For each pixel the recorded intensity is plotted as a function of θ_A. A polynomial fit is performed on the intensity profile to determine the minimal intensity and the corresponding analyzer angle θ_{Amin}. The retardance in the pixel under consideration is determined with equation (4.10) with θ_{Amin} in degrees. Figure 4-5 illustrates the determination of θ_{Amin} for one pixel in the field of view.

$$R(y) = \frac{\theta_{A\min}}{180}\lambda \tag{4.10}$$

The uncertainty on the measurement of R(y) depends first on the spatial resolution of the measurement along the y-axis. We used objective lenses with 40x and 20x magnifications and numerical apertures of 0.90 and 0.50 respectively, resulting in spatial resolutions of 0.43 μm and 0.77 μm. After magnification, the projected size of one spot on the camera is respectively 17.2 μm and 15.4 μm. The Nyquist criterion requires that the sampling interval is at least twice the highest spatial frequency of the specimen to preserve the spatial resolution in the resulting digital image, i.e. at least two pixels to cover one spot [18]. Considering the 6.7 μm pixelsize of the CCD camera (Axiocam MR, 1.3 MPixel resolution), we conclude that our spatial resolution equals the resolving power of the microscope. There is no spatial aliasing introduced by the CCD camera and the spatial resolution of the recorded images remains unchanged. This is sufficient to obtain radial profiles with a micron-level spatial resolution taking into account the typical dimensions of the optical fibers. Second, the uncertainty on R(y) is also influenced by the Sénarmont compensation measurement technique. According to [16] the typical error of the retardance measured with the Sénarmont compensation method is 0.5 nm. From the analysis of the standard deviation of the retardance we measure, we estimate that our measurement uncertainty has the same order of magnitude.

4.3 Inverse Abel transform algorithms

Knowing the retardance R(y), we now have to calculate the inverse Abel transform as given by equation (4.6). This transformation is not trivial. The need to numerically differentiate typically noisy R(y) data leads to large errors in the calculation of the inverse transform data and hence to errors in the determination of C. Literature proposes several algorithms, based on different principles. For example, [19] uses an iterative method based on deconvolution techniques; [8, 20] present recursive methods based on a linear, space-variant state-variable model of the Abel transform; whilst [1, 21–24] all rely on an algorithm based on Fourier theory. Based on the analysis of a series of algorithms, i.e. numerical integration, iterative method and integration with the algorithms proposed by [22] and [24], we decided to use the Fourier based [24] algorithm to compute the inverse Abel transform. The Fourier based algorithm is suited to handle profiles with many data-points; it also implicitly employs a low-pass filter. Additionally, studies comparing several methods mostly recommend using a Fourier based algorithm to compute the inverse Abel transform [21–23]. With this in mind we have developed two algorithms referred to as 'algo 1' and 'algo 2', described in the following subsections.

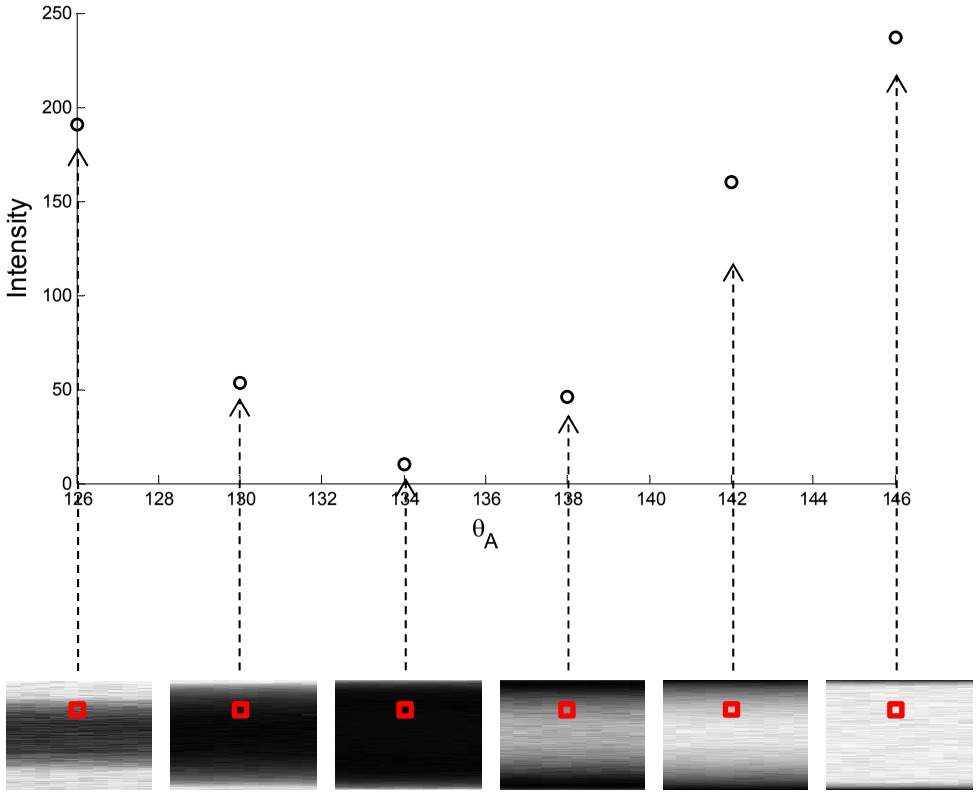

Figure 4-5: Illustration of the full-field Sénarmont compensation principle with microscope arrangement. For each analyser angle between θ_{Amin} and θ_{Amax} we record a picture of the whole field of view. For each pixel we draw the intensity as a function of the analyser angle to determine the angle θ_{min} that corresponds to the minimum intensity in that particular sample.

4.3.1 Original inverse Abel transform algorithm

Our first algorithm 'algo 1' is based on the decomposition in Fourier series of the measured retardance R(y) [25, 26]. This requires the following three assumptions to be valid:

- R(y) should be continuous;
- R(y) should be symmetric around y = 0;
- R(y) should be zero outside the interval [-b,b] with b the radius of the optical fiber.

If the optical fiber under test is axisymmetric and shows no abrupt transitions in the refractive index, then the three hypotheses are valid for the retardance profile R(y). This would not be the case, for example, for hollow-core fibers or for MOFs that show huge discontinuities of the refractive index at the transitions between the air-holes and the core/cladding material and hence R(y) cannot be considered continuous at the transitions in these particular fibers. In classical step-index fibers, the discontinuity between the core and cladding interface depends on the refractive index difference. This difference is usually rather small (typically 0.1 % – 1.1 %) and should have no major impact. Nevertheless, one should be careful when interpreting measurement results at these locations. We conclude that for classical step-index fibers, the assumptions can be considered fulfilled. In that case R(y) can be written as a cosine expansion:

$$R(y)_F = a_0 + \sum_{k=1}^{\infty} a_k \cos\left(\frac{k\pi y}{b}\right) \tag{4.11}$$

a_k is the k^{th} Fourier coefficient of the Fourier series and b is the radius of the fiber. We determine the Fourier coefficients using equation (4.12).

$$\begin{aligned} a_0 &= \frac{1}{b}\int_0^b R(y)dy \\ a_k &= \frac{2}{b}\int_0^b R(y)\cos\left(\frac{k\pi}{b}y\right)dy \end{aligned} \tag{4.12}$$

The derivative of (4.11) leads to:

$$\frac{dR(y)_F}{dy} = -\frac{\pi}{b}\sum_{k=1}^{\infty} a_k k \sin(\frac{k\pi y}{b}) \tag{4.13}$$

Substituting expression (4.13) in (4.5) yields equation (4.14).

$$\sigma_z \times C(r) = -\frac{\pi}{2b}\sum_{k=1}^{\infty} k a_k \times \frac{2}{\pi}\int_{t=0}^{\sqrt{1-\rho^2}} (t^2+\rho^2)^{-1/2} \times \sin(k\pi\sqrt{t^2+\rho^2})dt$$

$$\sigma_z \times C(r) = -\frac{\pi}{2b}\sum_{k=1}^{\infty} k a_k \times g_k(\rho) \tag{4.14}$$

where we define $g_k(\rho) = \frac{2}{\pi}\int_{t=0}^{\sqrt{1-\rho^2}} (t^2+\rho^2)^{-1/2} \times \sin(k\pi\sqrt{t^2+\rho^2})dt$ as basic functions, ρ= r/b is the normalized radius and $t = \frac{\sqrt{y^2-\rho^2}}{b}$. The basic functions $g_k(\rho)$ are independent of the measured data. The incorporation of the basic functions is very convenient. The computation of these functions is time-consuming, but they have only to be computed once since they are valid for all measurements.

4.3.2 Adapted inverse Abel transform algorithm

The inverse Abel transform requires the integration of the derivative of R(y), which implies that measurement noise on R(y) significantly impacts the final result. As we will show in Section 7, the measured retardance profiles for POFs are noisier compared to those measured with silica fibers. This leads to an increased variance in the calculated radial profiles of the photoelastic coefficient, which prompted us to modify the approach to compute the inverse Abel transform. We labeled our new algorithm with 'Algo 2'. It still relies on Fourier theory, but the product $\sigma_z \times C(r)$ is expanded in Fourier series instead of the measured retardance, as inspired by [21]. The forward Abel transform of $\sigma_z \times C(r)$ results in the measured retardance. The expression of the forward Abel transform is given by equation (4.4). The main advantage of the forward Abel transform is that it

does not require the integration of a derivative. Furthermore, 'Algo 2' should converge faster as there is a constant term in the Fourier expansion of $\sigma_z \times C(r)$. In 'Algo 1' we expand the retardance R(y). The inverse Abel transform of R(y) requires differentiating R(y). Consequently, the constant term disappears and more Fourier coefficients are required to allow 'Algo 1' to converge. We thus expect a better and more robust behaviour of 'Algo 2' when dealing with noisy data. The expansion of $\sigma_z \times C(r)$ is shown in equation (4.15).

$$\left[C(r)\times\sigma_z\right]_F = a_0 + \sum_{k=1}^{\infty} a_k \cos(k\pi\frac{r}{b}) \tag{4.15}$$

with a_k the k^{th} coefficient of the Fourier expansion. To obtain the computed retardance $R_F(y)$ from the product $[C(r)\times\sigma_z]_F$ we have to calculate the forward Abel transform of the latter. The analytical expression of the forward Abel transform is given by equation (4.16)

$$R(y) = 2\int_y^b \left[C(r)\times\sigma_z\right]_F \frac{r}{\sqrt{r^2-y^2}}dr \tag{4.16}$$

Substituting (4.15) in equation (4.16) yields the final expression of the retardance, which can be written as expression (4.17)

$$R_F(y) = b\times a_0 \int_0^{\sqrt{1-\rho^2}} dt + b\times\sum_{k=1}^{\infty} a_k \int_0^{\sqrt{1-\rho^2}} \cos(k\pi\sqrt{t^2+\rho^2})dt \tag{4.17}$$

where $\rho=y/b$ is the normalized radius and $t = \frac{\sqrt{r^2-y^2}}{b}$. Here also we isolated basic functions that are independent of the measured optical fiber and we calculate numerically the corresponding values that can be stored on the computer in the form of a matrix (equation (4.18)):

$$f_{k=0} = \int_0^{\sqrt{1-\rho^2}} dt$$
$$f_{k=1\to\infty} = \int_0^{\sqrt{1-\rho^2}} \cos(k\pi\sqrt{t^2-\rho^2})dt \tag{4.18}$$

To compute the amplitude of the k Fourier coefficients a_k we apply the least square criterion [27] and we evaluate the expression given in equation

$$\sum_{i=1}^{N}\left[R_F(y_i) - R(y_i)\right]^2 = Min \tag{4.19}$$

Once we have determined the Fourier coefficients a_k, their insertion in (4.15) allows us to determine $C(r)\times\sigma_z$ and therefore also the radial profile of the photoelastic coefficient.

In Chapter 5 we will carry out an in-depth analysis of both algorithms with the aim to evaluate and validate their effectiveness. To do so we will use pre-defined refractive index profiles, as has been commonly used by other authors to check the validity of inverse Abel transform algorithms [1, 24, 28].

4.4 Summary

In this Chapter we have discussed our method to measure the retardance profile of a laterally illuminated optical fiber and to compute the inverse Abel transform.

To measure the retardance we rely on the Sénarmont compensation method and to obtain a full-field view of the retardance R(y) we use a polarizing microscope that offers sufficient spatial optical resolution.

To determine the inverse Abel transform of the measured retardance profile we propose two algorithms, both relying on Fourier theory. The first algorithm, 'algo 1', expands R(y) in Fourier series and afterwards we compute the inverse Abel transform of the expansion. The second algorithm, 'algo 2', on the other hand, starts from the expansion of the

desired profile in Fourier series and then computes the forward Abel transform. The obtained function is subsequently compared to the measured retardance based on the least squares criterion.

In the next Chapter, we will analyze the behavior of our two inverse Abel transform algorithms in more details and we will discuss the influence of measurement noise on the expected result. We will investigate if – as we would expect – 'algo 2' is more robust than 'algo 1' when dealing with noisy measured R(y) profiles.

Bibliography

[1] K. Tatekura, "Determination of the index profile of optical fibers from transverse interferograms using Fourier theory," *Appl. Opt.*, vol. 22, no. 3, pp. 460–463, 1983.

[2] E. Hecht, *Optics*. Addison Wesley, 2002.

[3] A. Kuske and G. Robertson, *Photoelastic stress analysis*. John Wiley, 1974.

[4] M. P. Varnham, S. B. Poole, and D. N. Payne, "Thermal stress measurements in optical-fibre preforms using preform-profiling techniques," *Electron. Lett.*, vol. 20, no. 25/26, pp. 1034–1035, 1984.

[5] H. Poritsky, "Analysis of thermal stresses in sealed cylinders and the effect of viscous flow during anneal," *Physics (College. Park. Md).*, vol. 5, pp. 406–411, 1934.

[6] E. Stanley, *Transforms and Applications Handbook, Third edition*. CRC Press, Taylor and Francis Group, 2010.

[7] A. J. Jakeman and R. S. Anderssen, "Abel type integral equations in stereology: I. General discussion," *J. Microsc.*, vol. 105, no. 2, pp. 121–133, 1975.

[8] E. W. Hansen and P.-L. Law, "Recursive methods for computing the Abel transform and its inverse," *J. Opt. Soc. Am. A*, vol. 2, no. 4, p. 510, 1985.

[9] C. C. Montarou, "Two-wave-plate compensator method for full-field retardation measurements," *Appl. Opt.*, vol. 45, no. 2, pp. 271–280, 2006.

[10] C. C. Montarou, "Residual stress profiles in optical fibers determined by the two-wave-plate-compensator method," *Opt. Commun.*, vol. 265, pp. 29–32, 2006.

[11] L. N. Glass Stress Summer School, Tallinn, "Photoelasticity of glass."

[12] K. J. Gadvik, *Optical metrology*, Third Edit. Wiley & Sons, LTD, 2002.

[13] P. Kurzynowski and W. A. Woźniak, "Phase retardation measurement in simple and reverse Senarmont compensators without calibrated quarter wave plates," *Opt. - Int. J. Light Electron Opt.*, vol. 113, no. 1, pp.

51–53, 2002.

[14] G. L. Cloud, *Optical methods of engineering analysis*. Cambridge University Press, 1998.

[15] P. Kurzynowski, "Senarmont compensator for elliptically birefringent media," *Opt. Commun.*, vol. 197, no. 4–6, pp. 235–238, 2001.

[16] C. C. Montarou and T. K. Gaylord, "Two-Wave-Plate Compensator Method for Single-Point Retardation Measurements," *Appl. Opt.*, vol. 43, no. 36, pp. 6580–6595, 2004.

[17] F. L. Pedrotti and L. S. Pedrotti, "Introduction to optics 2nd edition," *Introduction to Optics 2nd Edition by Frank L. Pedrotti, SJ, Leno S. Pedrotti New Jersey: Prentice Hall, 1993*, vol. 1. 1993.

[18] "CCD Spatial resolution." [Online]. Available: http://www.andor.com/learning-academy/ccd-spatial-resolution-understanding-spatial-resolution.

[19] Vicharelli, "Iterative method for computing the inverse Abel transform," *Appl. Phys. Lett.*, vol. 50, no. 10, pp. 557–559, 1987.

[20] E. González-Ramírez, E. de la Rosa Miranda, J. G. Arceo-Olague, J. J. Villa-Hernández, I. de la Rosa Vargas, T. Saucedo Anaya, L. R. Berriel-Valdos, and M. A. Araiza-Esquivel, "Abel transform inversion using Kalman filter," vol. 8785, p. 8785B6, 2013.

[21] G. Pretzler, H. Jäger, T. Neger, H. Philipp, and J. Woisetschläger, "Comparison of Different Methods of Abel Inversion Using Computer Simulated and Experimental Side-On-Data," *Zeitschrift für Naturforschung. A, A J. Phys. Sci.*, vol. 47, no. 9, pp. 955–970, 1992.

[22] M. R. Hutsel and C. Montarou, "Algorithm performance in the determination of the refractive-index profile of optical fibers," *Appl. Opt.*, vol. 47, no. 6, pp. 760–767, 2008.

[23] H. Fulge, A. Knapp, C. Eichhorn, R. Wernitz, and L. Stefan, "Improved Abel Inversion Method for Analysis of Spectral and Photo-Optical Data of Magnetic Influenced Plasma Flows,"42nd AIAA Plasmadynamics and lasers conference, pp. 1–11, 2011.

[24] M. Kalal and K. Nugent, "Abel inversion using fast Fourier transforms,"

Appl. Opt., vol. 27, no. 10, pp. 1956–1959, 1988.

[25] S. Acheroy, P. Merken, H. Ottevaere, T. Geernaert, H. Thienpont, and F. Berghmans, "Influence of measurement noise on the determination of the radial profile of the photoelastic coefficient in step-index optical fibers.," *Appl. Opt.*, vol. 52, no. 35, pp. 8451–9, 2013.

[26] S. Acheroy, M. Patrick, G. Thomas, H. Ottevaere, H. Thienpont, and F. Berghmans, "On a possible method to measure the radial profile of the photoelastic constant in step-index optical fiber," in *SPIE: Optical Sensing and Detection III*, 9141, p. 914115, 2014.

[27] L. V. Fausset, *Applied numerical analysis using Matlab*. Prentice Hall, 1999.

[28] M. R. Hutsel, "Algorithm performance in the determination of the refractive-index profile of optical fibers," *Appl. Opt.*, vol. 47, no. 6, pp. 760–767, 2008.

[29] S. Acheroy, P. Merken, H. Ottevaere, T. Geernaert, H. Thienpont, and B. Francis, "Influence of measurement noise on the determination of the radial profile of the photoelastic coefficient in step-index optical fibers," *Appl. Opt.*, vol. 52, no. 35, pp. 8451–8459, 2013.

[30] S. Acheroy, P. Merken, T. Geernaert, H. Ottevaere, H. Thienpont, and F. Berghmans, "Algorithms for determining the radial profile of the photoelastic coefficient in glass and polymer optical fibers," *Opt. Express*, vol. 23, no. 15, p. 18943, 2015.

Chapter 5. The inverse Abel transform algorithms – evaluation of the effectivity and of the influence of measurement noise

For a perfectly cylindrical and homogeneous optical fiber, with axial stress and photoelastic constant that are constant across the fiber, and in case we would not have to deal with measurement artifacts or noise, the shape of the measured retardance R(y) would resemble a perfect semi-ellipse. To assess the effectivity of our inverse Abel transform algorithms, we therefore investigate how the algorithms that we have introduced in the previous Chapter behave along with the various parameters involved when applied to such a semi-ellipse[2]. In section 5.1 we compare the numerical results of the inverse Abel transform with the analytical expression of the inverse transform of the semi-ellipse. In section 5.2 we add noise to the ellipse so as to mimic measurement noise. This allows determining the optimal set of parameters that returns the most effective inverse transform. We will then use this set of parameters in the following Chapters in order to carry out the inverse Abel transform on the actual measurement data.

5.1 Evaluation of the inverse Abel transform algorithms

Prior to applying the inversion algorithms directly on measured retardance profiles R(y), we test it first on a predefined R(y) with a well-known

[2] The results presented in this chapter have been partly published in [6, 12, 13]

analytical expression. This approach allows us to analyze the behavior and effectivity of both algorithms that we have developed and described in Chapter 4, i.e. 'algo 1' and 'algo 2'. Assuming the axial stress to be homogeneously distributed across the fiber and that the photoelastic coefficient is constant, C(r) is a rectangular function with C(r) equal to C for r ∈ [-b,b] and equal to zero outside these boundaries, with b the radius of the fiber. In that particular case, the expression 4.4 from Chapter 4 describing the retardance R(y) as a function of the axial stress becomes:

$$R(y) = 2C\sigma_z \times \int_y^b \frac{rdr}{\sqrt{r^2 - y^2}} = 2C\sigma_z \times b\sqrt{1 - \frac{x^2}{y^2}} \tag{5.1}$$

Consequently, the forward Abel transform $C \times \sigma_z$ yields R(y), which has the shape of half an ellipse or 'semi-ellipse' E(y) that is described in general with equation (5.2).

$$R(y) \approx E(y) = A\sqrt{1 - \frac{y^2}{B^2}} \tag{5.2}$$

The similarity between R(y) and E(y) is illustrated with Figure 5-1, where R(y) is the measurement of the retardance R(y) in a fiber cross-section. A and B are respectively the semi-short and the semi-long axis of the ellipse. The numerical value of A is taken equal to the value of the retardance at y=0: $A = R(0) = C\sigma_z \times 2b$. In the example shown in Figure 5-1, A equals -44.985 nm. B is the radius of the fiber and in our example B = b = 62.5 µm.

The analytical expression of the inverse Abel transform of (5.2) is a constant value as shown in equation (5.3).

$$\sigma_z \times C = \frac{1}{\pi}\int_r^B \frac{yA}{B\sqrt{B^2 - y^2}}(y^2 - r^2)^{-1/2}dy = \frac{1}{2}\frac{A}{B} \tag{5.3}$$

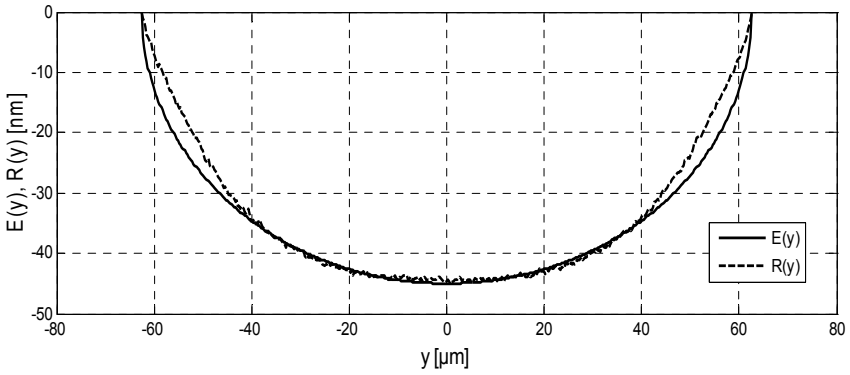

Figure 5-1: Similarity between the elliptical shape E(y) and the retardance R(y) in one fiber section. The numerical values of the semi-short and semi-long axes of E(y) are, respectively: A = -max(abs(Ry)) and B = b, the radius of the fiber.

Using equation (5.3) we easily calculate the analytical inverse Abel transform of E(y) and obtain $-3{,}59\times10^{-4}$. This analytical value will serve as reference to evaluate the numerical result of the inverse Abel transform of E(y) that should be constant along the length of the semi-long axis, in the interval [-b,b], and zero outside that boundary. In the remainder of the manuscript, we will use the definitions enumerated hereafter:

- $\boldsymbol{F(r)=-\frac{1}{2}\frac{A}{B}}$ is the analytical expression of the inverse Abel transform of E(y);
- $\mathbf{F_{IAT1}(r)}$ is the inverse Abel transform of E(y) obtained with 'algo 1', i.e. equation 4.14 from Chapter 4;
- $\mathbf{F_{IAT2}(r)}$ is the inverse Abel transform of E(y) obtained with 'algo 2', i.e. equation 4.17 and 4.18 from Chapter 4;
- **N** is the amount of pixels needed to cover the fiber diameter equal to 2×b, it equals the number of data-points of the retardance R(y);
- **P** is the number of radial points of the reconstructed inverse Abel transforms $F_{IAT1}(r)$. For 'algo 2' we have to compare E(y) with the forward Abel transform of the expected result $F_{IAT2}(r)$ to obtain the

Fourier coefficients a_k of the Fourier expansion of the latest. This implies that for the second algorithm the number of radial points P should equal the amount of data-points N. Thus P is not a parameter in the case of 'algo 2'.

- **k** is the amount of Fourier coefficients taken into consideration;
- **dt** is the integration step.

We use the Matlab [1] environment to program both algorithms and study their effectivity. The half ellipse E(y) is constructed with the same amount of points N as the measured retardance. In this evaluation of the inverse Abel algorithm, we do not yet add noise to E(y). To compute the inverse Abel transform of E(y), three parameters have to be fixed. These are:

- the number of Fourier coefficients k;
- the amount of radial points P ;
- the integration step dt in equations (4.14) and (4.17) given in the previous Chapter.

Matlab proposes two numerical methods to compute a definite integral, the 'quad' and the 'trapz' commands. We evaluate these integration methods with 'algo 1' since it is the first algorithm that we have implemented.

The 'quad' command does not give us the possibility to control the integration step dt. The results using this integration method are not satisfactory; $F_{IAT1}(r)$ contains a large amount of numerical artefacts. On the contrary, the 'trapz' command allows choosing our own integration step dt. According to [2] the 'quad' function provides less accurate results as that function approximates the integral using the quadrature method, i.e. it breaks the area down into rectangles. The 'trapz' function approximates the area with trapezoids. The implementation of the algorithm using the 'trapz' function leads to smoother results, i.e. with less numerical artefacts. This should allow for a better visualization of the eventual transitions in the radial profile of C(r). To illustrate the differences, Figure 5-2 compares F_{IAT1} obtained with the 'trapz' and the 'quad' functions.

Our simulations show that if dt is at least 150 times smaller than the radial point spacing, variations on dt do not longer influence the results. Based on these conclusions the integration step dt for the 'trapz' command

to compute $F_{IAT1}(r)$ of Figure 5-2 is chosen to be 150 times smaller than the radial point spacing, the number of radial points P being fixed at 300 and the amount of Fourier coefficients k taken equal to 100. This prompted us to use the 'trapz' function to compute the definite integrals in 'algo 1' and in 'algo 2'.

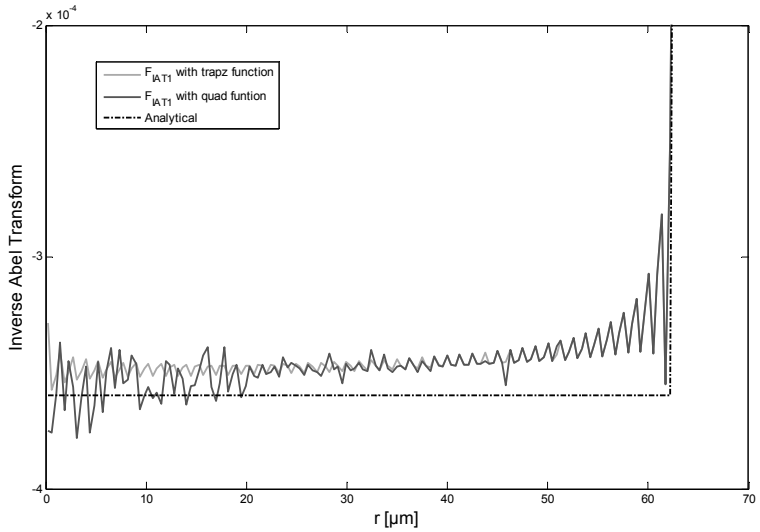

Figure 5-2: The analytical inverse Abel transform F(r) is compared to the numerical result $F_{IAT1}(r)$. $F_{IAT1}(r)$ is alternatively computed with the numerical methods 'trapz' and 'quad' to work out the definite integral. $P = 300$, $k = 100$.

We computed the inverse transform of E(y) for a wide range of coefficients k and radial points P, the latest solely for 'algo 1'. We then calculated the root-mean-square (RMS) error between the numerical results $F_{IAT1}(r)$ and $F_{IAT2}(r)$ on one hand and the constant value of the analytical inverse transform F(r) on the other hand. As the inverse Abel transform of E(y) is a step function, we predict that a large number of Fourier coefficients are required to obtain a result close to the theoretical step function.

It appears that the amount of radial points P taken into consideration for 'algo 1' has a small impact only on the mean RMS error. Figure 5-3 compares the evolution of the RMS error of the inverse Abel transform as a function of k for both algorithms.

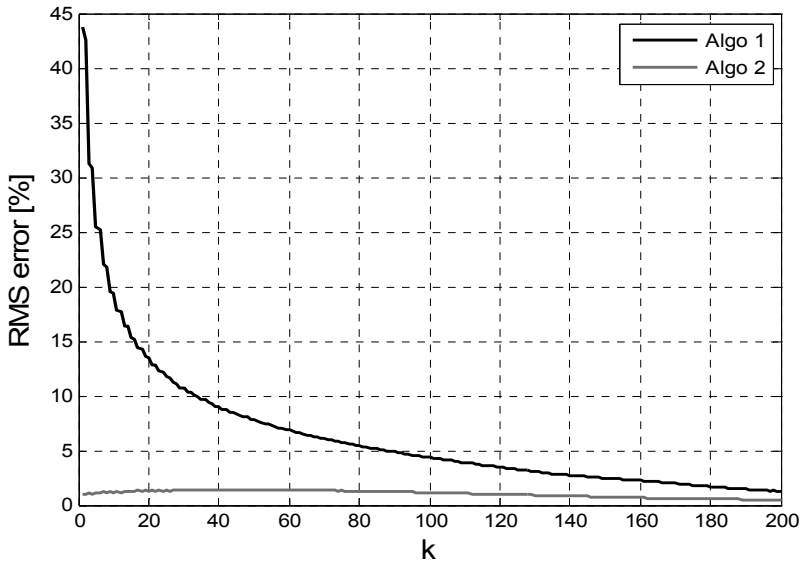

Figure 5-3: RMS error between the numerical results and the analytical expression of the inverse Abel transform of E(y). The RMS error is computed for an increasing amount k of Fourier coefficients a_k in the Fourier expansion. The numerical results are respectively obtained with 'algo 1' and 'algo 2'.

From these results we conclude that the second algorithm 'algo 2' converges faster than 'algo 1'.

To obtain a profile $F_{IAT1}(r)$ close to the theoretical shape F(r), numerous Fourier coefficients need to be considered to achieve a small RMS error, whilst the radial profile of F_{IAT2} will already be close to the ideal profile with a single Fourier coefficient.

Figure 5-4 and Figure 5-5 represent the inverse Abel transform of the E(y) for $k_1 = 20$ and $k_2 = 200$ computed with 'algo 1' and 'algo 2', respectively F_{IAT1} and F_{IAT2}. They illustrate the impact of the number of Fourier coefficients k on the final shape of the inverse Abel transform and the faster convergence of the second algorithm. The results are compared with the analytical expression F(r) of the inverse Abel transform of E(y). These graphs also show that the presence of the constant term a_0 allows F_{IAT2} to converge faster towards the analytical expression.

The RMS-error of F_{IAT1} and F_{IAT2} increases at the edges and in the center of the transform, i.e. at the edges and in the center of the core of the fiber. That phenomenon cannot be avoided; these numerical artefacts are inherent to the inverse Abel transform [3–5]. It is illustrated in Figure 5-4 and Figure 5-5 where F_{IAT1} and F_{IAT2} both exhibit a more oscillatory profile at the edges, i.e. around $r = 0$ µm and $r = 62.5$ µm. To conclude, the Fourier based algorithms give very satisfactory results on the noiseless elliptical shape E(y), provided P and especially k are carefully chosen [6, 7].

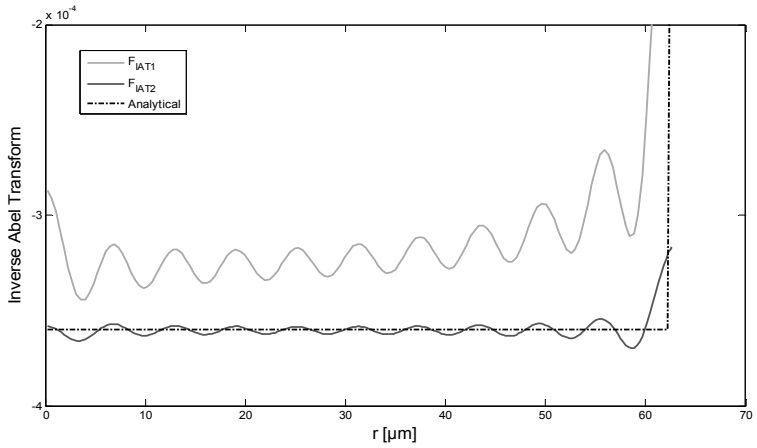

Figure 5-4: The analytical inverse Abel transform F(r) of the ellipse without added noise is compared to the numerical results $F_{IAT1}(r)$ and $F_{IAT2}(r)$. For 'algo 1' and 'algo 2' the amount of radial points P are 300 and 470, respectively. The number of Fourier coefficients k_1 is 20 for each algorithm

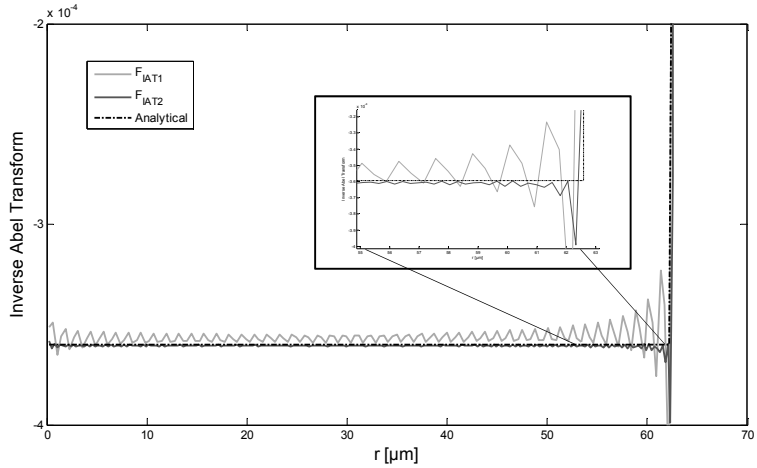

Figure 5-5: The analytical inverse Abel transform F(r) of the ellipse without added noise is compared to the numerical results $F_{IAT1}(r)$ and $F_{IAT2}(r)$. For 'algo 1' and 'algo 2' the amounts of radial points P are 300 and 470, respectively. The number of Fourier coefficients k_2 is 200 for each algorithm. The inset shows a magnified portion at the edge of the ellipse, r = [55µm;62,5µm].

5.2 Influence of noise on the inverse Abel transform algorithms

To continue our evaluation of the inverse Abel transform algorithms, we add Gaussian noise to E(y). This noise is meant to mimic actual measurement noise.

To do so we took three values for the standard deviation of the Gaussian noise, respectively fixed to $\sigma_1 = 0.1\times10^{-9}$, $\sigma_2 = 0.5\times10^{-9}$ and $\sigma_3 = 1\times10^{-9}$. These figures correspond to actual standard deviation levels computed from retardance profiles that we have measured. We pay particular attention to the influence of the parameters k and P on the results. k is chosen in the interval [20-200] and P in the interval [120-600], the latter only for 'algo 1'. For 'algo 2' P should equal N as we have explained previously. The analysis of the behavior of the inverse Abel transform on the noisy profile is performed in several steps.

5.2.1 Inverse Abel transform of the noisy profiles

The first step consists in computing the inverse transform for each noise-level and for each value of the couple (k, P). The operation is repeated several times to enable calculating a mean value. This operation is straightforward but time and memory consuming. Figure 5-6 shows examples of the inverse transform of E(y) for two values of k. To compute the inverse Abel transform we have fixed the amount of Fourier coefficients to $k_1 = 10$ and $k_2 = 50$. The variance of the Gaussian noise added to the E(y) in that particular case was $\sigma_2 = 0.5\times10^{-9}$. The profiles are in line with our conclusion of the previous section, i.e. 'Algo 2' returns a profile close to the analytical profile for the small amount of Fourier coefficients k_1 whilst 'Algo 1' requires a larger amount of Fourier coefficients to get close to the shape of the analytical inverse Abel transform F(r). This goes at the expense of having a very noisy profile. We can conclude, a priori, that 'algo 2' converges faster towards the theoretical profile than 'algo 1'. We will demonstrate later that the faster convergence of 'algo 2' is an essential characteristic when dealing with noisy profiles.

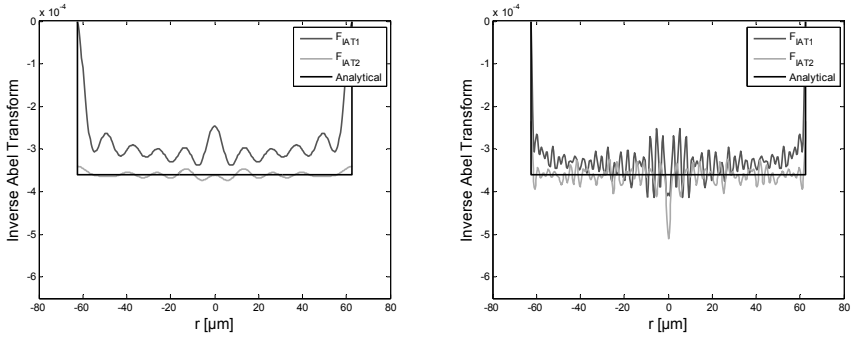

(a) (b)

Figure 5-6: The inverse Abel transform of the noisy ellipse for $k_1 = 10$ (a) and $k_2 = 50$ (b) computed with 'Algo 1' and 'Algo 2'. The standard deviation of the Gaussian noise on the signal is $\sigma_2 = 0.5\times10^{-9}$. The results are compared to the analytical value of the inverse transform of E(y).

5.2.2 Calculation of the RMS error

Minimal mean RMS calculation for 'algo 1'

In a second step we compute the RMS error between the analytical inverse Abel transform and the computed inverse transform of the ellipse for each data-point of the whole set of simulation results. We then calculate the average RMS error on every data-point for the same set of simulation parameters (same σ, k and P). Subsequently we obtain the mean RMS error over the P radial points for each set of parameters (σ, k, P). The inverse Abel transform produces large overshoots at the fiber boundaries. To minimize their influence on the mean RMS error, we also analyze the average in the interval r = [0, b/2] with b the radius of the fiber.

In order to analyze the influence of P and k on the RMS error, we consider the minimal error as a function of P and k respectively. The results are shown in Figure 5-7. The first graph depicts the minimal error as a function of the number of radial points P. The small peaks at 157, 235 and 469 correspond to N/3, N/2 and N. The interpolation of the original noisy ellipse of N data-points to obtain P radial points filters out noise. Care has to

be taken not to lose too much information with this operation. As expected, the RMS error increases with the variance of the original signal. On the other hand, the choice of P has no significant influence on the RMS error. The bottom graph of Figure 5-7 shows the evolution of the minimal error as a function of the chosen amount k of Fourier coefficients. The analysis of the evolution of the minimal error reveals that the choice of k is crucial. For an increasing variance on E(y), k has to be reduced in order to avoid additional errors due to the inverse transform algorithm. However, when the variance of the original signal is sufficiently small, a larger value of k yields more accurate results.

On the other hand, it makes no sense to take into account more than 80 Fourier coefficients, since a larger value does not decrease the minimal error, whilst the computation time increases with k. Additionally, a high value of k generates oscillations with a period inversely proportional to k (Figure 5-6).

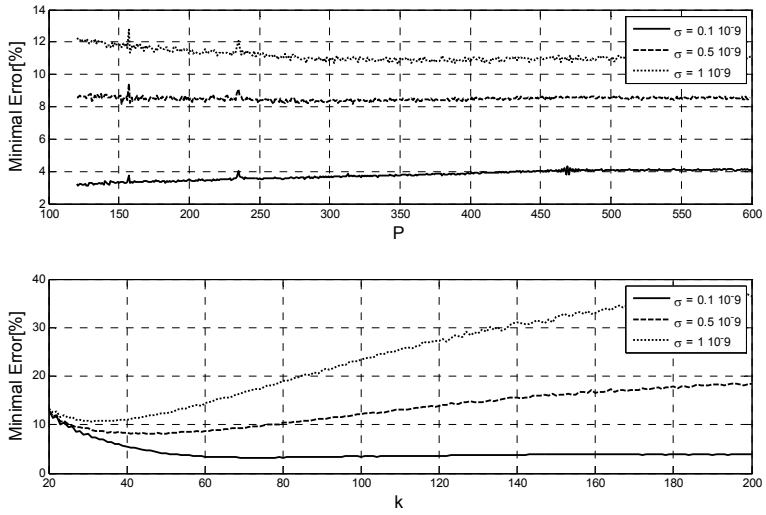

Figure 5-7: Minimum error as a function of the number of radial points P (top) and as a function of the chosen amount of Fourier coefficients k (bottom). The mean error is taken over the interval $r = [0, b/2]$.

Mean RMS error calculation for 'algo 2'

The set of parameters we consider for the second algorithm is (σ,k). Here also we determine the mean RMS error for each level of the standard deviation as a function of k. Results are plotted and compared to 'algo 1' in Figure 5-7, i.e. the evolution of the mean RMS error as a function of the chosen amount k of Fourier coefficients. The issue is no longer to find the minimal error, as now we fix the number of radial points to P = 300 for 'algo 1' and P = N for 'algo 2'.

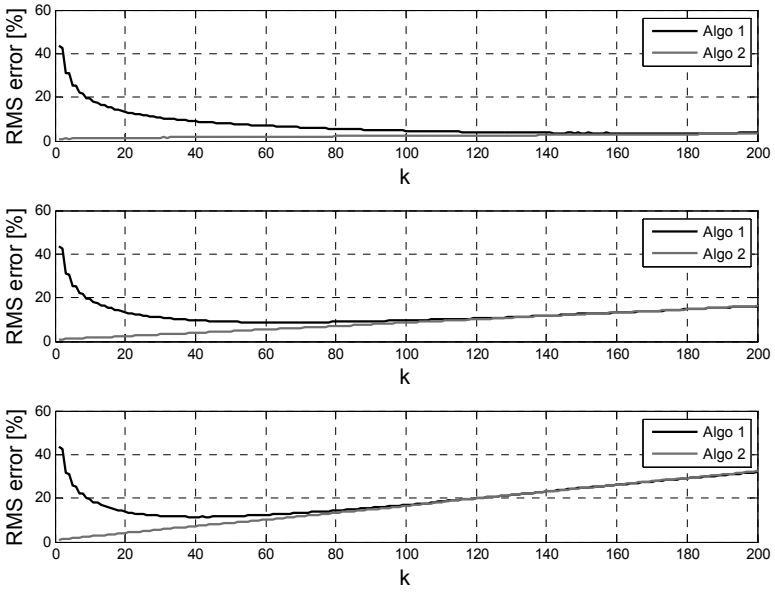

Figure 5-8: RMS error between the analytical value of the inverse Abel transform of the ellipse and the computed Abel transform of the noisy ellipse as a function of the amount of Fourier coefficients k respectively for 'algo 1' and 'algo 2'. The standard deviation of the Gaussian noise added to the signal: $\sigma_1 = 0.1\ 10^{-9}$ for the upper graph; $\sigma_2 = 0.5\ 10^{-9}$ for the central graph and $\sigma_3 = 1\ 10^{-9}$ for the bottom graph.

For a small value of the standard deviation of the noisy ellipse, we demonstrate that a high number of Fourier components leads to a better result. But when the standard deviation of the measured signal increases, the influence of the noise on the inverse Abel transform becomes dominant.

Increasing the number of Fourier coefficients adds substantial oscillations to the resulting profile. Taking a small amount of Fourier coefficients acts as a low-pass filter as it filters out the high-frequency oscillations. We tried to reduce the RMS error by applying filtering and smoothing algorithms. However, these methods barely have an effect on the RMS error, since the appropriate choice of k already acts as a low-pass filter [8–11].

Figure 5-8 evidences that 'Algo 2' is more robust than 'Algo 1' for computing inverse Abel transforms of profiles with a high variance. A minimal error of 12% with 'Algo 1' requires about 40 coefficients, whilst 'Algo 2' achieves much lower errors with a small value of k. For an increasing amount of Fourier coefficients both algorithms tend to behave in the same manner with an increasing RMS error.

Calculation of the parameter sets

To conclude, for 'algo 1' we computed the minimal RMS error for a complete set of simulation parameters and we found the corresponding couple (k, P) for 3 different noise levels. For 'algo 2' the amount of radial points is fixed, and consequently we computed the mean RMS error for the simulation parameter k. The results are summarized in Table 1 for both algorithms. These are mean values since they are computed for the mean RMS errors of several simulations. The ideal values for a specific profile can be slightly different, but will be in the range of the values obtained here. From the evolution of the minimal error profile, we recommend to choose a small k value, as the minimal error increases substantially for higher k values. In the case of 'algo 1', the k values given in Table 5-1 are the maximum values that we recommend.

Variance	0.1×10^{-9}		0.5×10^{-9}		1×10^{-9}	
	k	P	k	P	k	P
'Algo 1'						
min RMS (mean for r ∈ [0,b])	100	216	55	126	45	282
min RMS (mean for r ∈ [0,b/2])	74	128	41	152	31	349
min RMS (mean for r ∈ [0,b/4])	72	122	37	206	29	486
'Algo 2'						
min RMS (mean for r ∈ [0,b/2])	1	470	2	470	2	470

Table 5-1: (k,P) combinations for minimal RMS error on the inverse Abel transform. The parameter P has no influence on the RMS error for 'algo 2' as it is fixed (P = N).

We recall that the analytical expression of E(y) is a constant function and since in 'Algo 2' the constant term of the Fourier expansion a_0 is taken into account in contrast with 'algo 1', only a few Fourier coefficients are needed as shown in Table 5-1. Considering the core/cladding structure of the optical fiber, the retardance will not always be identical to an elliptical shape. An insufficient amount of Fourier coefficients could filter out crucial information from the retardance profile and the corresponding inverse Abel transform.

5.3 Summary

The goal of this Chapter was to analyse the effectiveness of our inverse Abel transform algorithms 'algo 1' and 'algo 2' required to compute the inverse of the retardance in order to recover the photoelastic constant from retardance measurements. Under the hypotheses that our optical fiber is a perfectly uniform cylinder with constant C and with axial stress uniformly distributed over its cross-section, the measured retardance R(y) can be substituted with the shape of a semi-ellipse E(y). The inverse Abel transform of E(y) is a constant that is solely function of the half-long and half-short axes of E(y).

First, we evaluated both numerical inversion algorithms applied to E(y) without added noise. We defined the set of parameters that should be considered to obtain the best possible inverse transform, i.e.:

- k, the amount of Fourier coefficients considered in the numerical inverse transform;

- dt, the integration step;
- P, the number of radial points, but only for ‘algo 1’, since for ‘algo 2’ P=N.

We compared the results of the numerical transforms F_{IAT1} and F_{IAT2} respectively with the constant analytical transform profile F(r) by computing the mean RMS error between the numerical and analytical profiles. From our simulation results, we conclude that if the integration step dt equals to or is smaller than 150 times the radial point spacing, it has no influence on the RMS error. The choice of P has close to no impact on the RMS error, but the choice of k is crucial. For ‘algo 1’ a high value of k is required to minimize the RMS error, whilst with ‘algo 2’ a minimum error is already achieved with a few Fourier coefficients. The main reason is the absence of the constant term a_0 of the Fourier expansion in the numerical expression of $F_{IAT1}(r)$, which is not the case for F_{IAT2} where the term a_0 remains.

We then added Gaussian noise to E(y) to evaluate the robustness of the algorithms when dealing with noisy measured profiles. We chose three levels for the standard deviation corresponding to actual variance values of measured retardance profiles R(y). We evaluate the RMS error for the whole set of parameters (σ, k, P). Although P has limited impact on the RMS error, it should not equal N nor a fraction of N to achieve some noise-filtering effect through the interpolation mechanism. Again the choice of k is crucial to achieve a minimal RMS error. ‘Algo 2’ is more robust than ‘algo 1’ when dealing with noisy profiles as it requires a small amount of k to converge. Both algorithms tend to behave in the same manner with an increasing RMS error for an increasing number of k.

We close by emphasizing that the results discussed above are essentially valid for the inverse Abel transform of half an ellipse. Considering the fabrication methods, and the core/cladding transitions in an actual optical fibre, R(y) is not necessarily shaped as a semi-ellipse. Therefore considering an insufficient amount of Fourier coefficients could inadvertently filter out information from actually measured retardance profiles.

Bibliography

[1] "Matlab." [Online]. Available: https://nl.mathworks.com/products/matlab/.

[2] "Mathworks Documentation." [Online]. Available: http://nl.mathworks.com/help/matlab/.

[3] H. Poritsky, "Analysis of thermal stresses in sealed cylinders and the effect of viscous flow during anneal," *Physics (College. Park. Md).*, vol. 5, pp. 406–411, 1934.

[4] E. W. Hansen and P.-L. Law, "Recursive methods for computing the Abel transform and its inverse," *J. Opt. Soc. Am. A*, vol. 2, no. 4, p. 510, 1985.

[5] E. Simonneau, A. M. Varela, and C. Muñoz-Tuñón, "Spectral inversion of the generalized Abel integral transform," *J. Quant. Spectrosc. Radiat. Transf.*, vol. 49, no. 2, pp. 149–156, 1993.

[6] S. Acheroy, P. Merken, H. Ottevaere, T. Geernaert, H. Thienpont, and F. Berghmans, "Influence of measurement noise on the determination of the radial profile of the photoelastic coefficient in step-index optical fibers.," *Appl. Opt.*, vol. 52, no. 35, pp. 8451–9, 2013.

[7] M. R. Hutsel, "Algorithm performance in the determination of the refractive-index profile of optical fibers," *Appl. Opt.*, vol. 47, no. 6, pp. 760–767, 2008.

[8] R. Piché, "Noise-Filtering Properties of Numerical Methods for the Inverse Abel Transform," *IEEE Trans. Instrum. Meas.*, vol. 41, no. 4, pp. 517–522, 1992.

[9] E. L. Kosarev and E. Pantos, "Optimal smoothing of 'noisy' data by fast Fourier transform," *J. Phys. E.*, vol. 16, no. 6, p. 537, 1983.

[10] J. Dong and R. J. Kearney, "Symmetrizing, filtering and abel inversion using fourier transform techniques," *J. Quant. Spectrosc. Radiat. Transf.*, vol. 46, no. 3, pp. 141–149, 1991.

[11] M. Kalal and K. Nugent, "Abel inversion using fast Fourier transforms," *Appl. Opt.*, vol. 27, no. 10, pp. 1956–1959, 1988.

[12] S. Acheroy, M. Patrick, G. Thomas, H. Ottevaere, H. Thienpont, and F.

Berghmans, “On a possible method to measure the radial profile of the photoelastic constant in step-index optical fiber,” in *SPIE: Optical Sensing and Detection III*, 9141, p. 914115, 2014.

[13] S. Acheroy, P. Merken, T. Geernaert, H. Ottevaere, H. Thienpont, and F. Berghmans, “Algorithms for determining the radial profile of the photoelastic coefficient in glass and polymer optical fibers,” *Opt. Express*, vol. 23, no. 15, p. 18943, 2015.

Chapter 6. Radial profile of the photoelastic coefficient in glass optical fibers

In this Chapter[3], we build on the tools that we have described in the previous Chapters and we report on our actual experimental results of the measurement of the radial profile of the photoelastic coefficient C(r) in silica optical fibers. In the first section, we summarize the characteristics of the optical fibers under test. The experimental mechanical system used to axially stress the fiber under a polarizing microscope is explained in section 6.2. Sections 6.3 and 6.4 deal with the actual measurements and with our approach to determine the analyzer angle giving the minimum intensity in one pixel of the fiber's image as well as the resulting retardance profiles of the fibers. In section 6.5 we first compute the mean photoelastic constant by approximating the measured retardance profile with a semi-elliptical profile. We compute the radial profile of the photoelastic coefficient without any approximation in section 6.6. We summarize our most important findings and we conclude this Chapter in section 6.7.

6.1 Characteristics of the glass optical fibers under test

Several publications have reported on the measurement of the photoelastic coefficient of glass optical fibers [1–3]. In the first publication, the authors measured the photoelastic coefficient on a Ge-doped silica fiber and analyzed the wavelength dependence of C. They obtain a value of C equal to -3.3×10^{-12} Pa^{-1} at a wavelength of 1064 nm. This is slightly lower than the

[3] The results presented in this Chapter have been partly published in [15–18]

value measured on bulk silica. Note that the authors did not mention the mean error value associated to that measured value. In [2] the authors determine C in pure fused silica fiber samples and obtain values of C equal to -3.19×10^{-12} Pa^{-1} at a wavelength of 514 nm. Bertholds et al. [3] obtained $C=-3.65\times10^{-12}$ Pa^{-1} at a wavelength of 633 nm. Both authors of [2,3] report a measurement error of 5%.

As discussed in the previous Chapters, we have developed our own approach to determine the photoelastic coefficient of optical fibers and its radial profile across the fiber. We can now validate our method and the related algorithms 'algo 1' and 'algo 2' using actual measurement data and comparing our results to those available in literature.

We have experimented with commercially available step index singlemode and multimode silica glass fibers with increasing core diameter. The main characteristics of those fibers are summarized in Table 6-1. All the fibers were purchased from the company Thorlabs [4]. The doped fiber portions, i.e. a Ge-doped core in fiber 1 and an F-doped cladding in fiber 2 and 3 to respectively increase the refractive index in the core and lower it in the cladding [5], allow us to investigate whether the doping influences the radial profile of C(r), or not.

Fiber	Type	Guidance	d_{core}	$d_{cladding}$	n_{core}	$n_{cladding}$
1	Ge-doped Silica core	Singlemode	9 µm	125 µm	1,462	1,458
2	F-doped depressed cladding	Multimode	50 µm	125 µm	1,457	1,440*
3	F-doped depressed cladding	Multimode	105 µm	125 µm	1,457	1,440

*Only the refractive index of the depressed portion of the cladding is mentioned

Table 6-1: Main characteristics of the optical fibers used to measure the retardance and to determine the radial profile of the photoelastic coefficient [4].

Before the fibers were placed under the polarizing microscope described in Chapter 4, they were stripped over 15 mm before being immersed in an index matching liquid. The stripped part was carefully

cleaned with alcohol to remove any dust or residual coating particles that would alter the quality of the image. About 300 µm of the stripped part appears in the field of view (FOV) of the microscope. Considering the outer diameter of the silica fibers, the 150 µm thickness of the cover glasses on which the fiber rests and the thickness of about 50 µm of the index matching liquid layer above the fiber, we chose to use the 40X objective for the measurements on the silica fibers. This objective has a 410 µm working distance, which allows for accommodating the total thickness of about 375 µm whilst providing for the largest magnification. The first microscope images recorded with fiber 2 indicate a mismatch between the index matching liquid (IML) and the fiber. Reference [6] indicates that the core of fiber 2 is surrounded with a fluorine-doped cladding and a measurement of the refractive index of this fiber given in [7, 8] indeed shows that this fiber has a depressed inner cladding surrounded by an undoped outer cladding. The use of an IML equal to the refractive index of the core solved the problem.

6.2 Controlled tensile stress system

As explained in Chapter 4, the photoelastic coefficient is the regression coefficient linking the axial stress σ_z to the according inverse Abel transform of the measured retardance R(y). We designed a simple system to apply a pre-defined tensile stress to the fiber while fixed in the microscope arrangement.

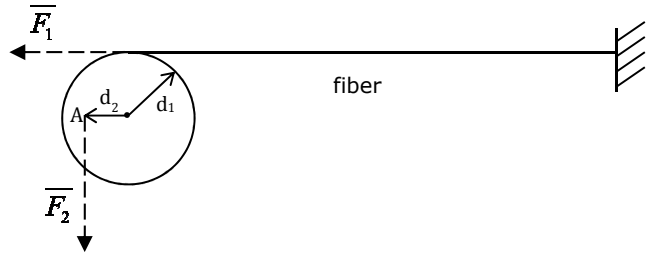

Figure 6-1: Scheme of the loading system for applying a pre-defined tensile stress to the optical fiber under test.

The principle of our loading system is illustrated in Figure 6-1. The fiber is fixed at one end whilst the other is clamped in a pulley that rotates about a frictionless axis. The fiber is submitted to external axial tensile stress by adding weights to a balance fixed to the pulley at location A, as also shown in Figure 6-1. The weights induce a vertical force $\overline{F_2}$ and a horizontal tensile force $\overline{F_1}$ respectively at a distance $d_2 = 6.15$ cm and $d_1 = 10$ cm from the center of the wheel. The relations between the weights w, the magnitudes of the forces $\overline{F_1}$ and $\overline{F_2}$ and the tensile stress σ_z are given in equation (6.1).

$$\begin{aligned} F_2 &= w \times g \\ F_1 &= \frac{F_2 \times d_2}{d_1} \\ \sigma_z &= \frac{F_1}{\pi \times b^2} \end{aligned} \tag{6.1}$$

where g is the gravitational acceleration and b the radius of the fiber. The fiber ends are fixed at a considerable distance, about 20 cm, from the measurement point to ensure a uniform distribution of the tensile stress across the fiber. We assume that the fibers are homogeneous along their length and that variations of the displacement along the fiber can be neglected. According to the manufacturer, the core/cladding concentricity error is below 1 μm [9]. We therefore also assume that we will obtain identical retardance profiles for each longitudinal portion of the fiber. A photograph of the complete setup is shown in Figure 6-2.

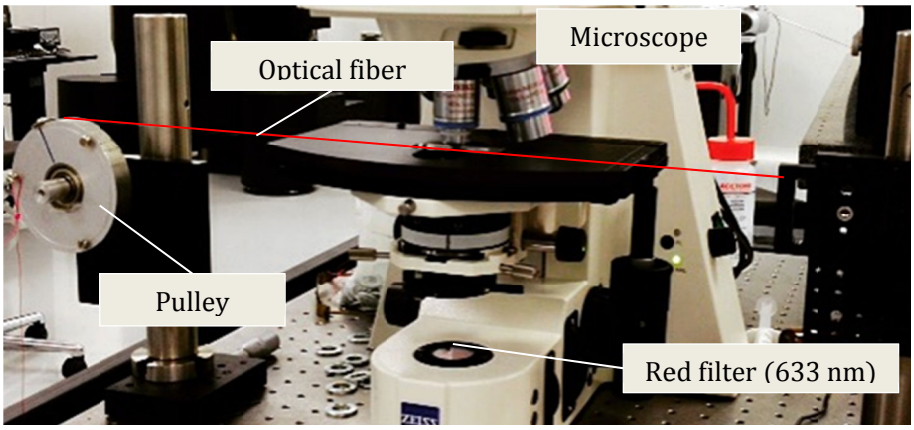

Figure 6-2: Optical fiber placed in the polarizing microscope arrangement with the external axial loading system.

The tensile stress we apply to the fibers increases from 60 MPa to 185 MPa. The interval is chosen in such a way that, on one hand, we have a measurable stress-induced birefringence with an acceptable dynamic range, and on the other hand, we avoid fiber breakage.

6.3 Calculation of the minimum intensity

Once the optical fiber has been placed in the setup described above, we can apply the Sénarmont compensation principle to measure the full field retardance as described in Chapter 4. For the glass fibers a picture is taken every 2° rotation of the analyser in the angular range θ_{ATot}. Figure 6-3(a) shows an image of a fiber taken with the CCD camera for a specific angular position of the analyser giving enough contrast in the image. Figure 6-3(b) shows the image with the same angle of the analyser but without fiber, i.e. an image of the background.

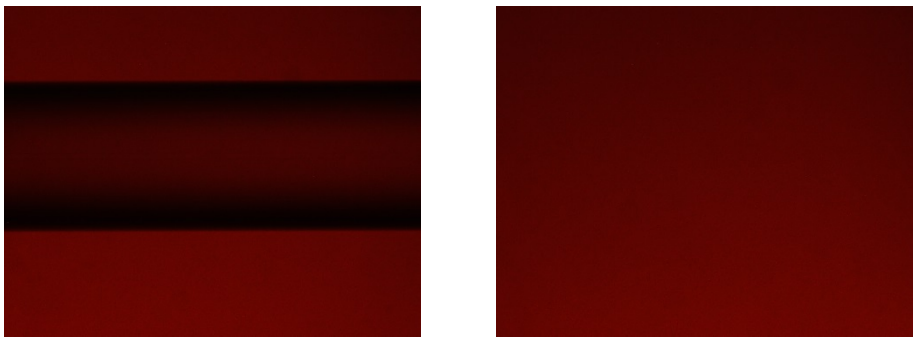

(a) (b)

Figure 6-3: CCD image of the polarizing microscope for a specific angular setting of the analyser. (a) Image with the fiber in the measurement setup. (b) Image of the background.

Examining Figure 6-3 we can make two observations:

The fiber does not fill the entire image.

We want to avoid wasting computation time on pixels that are not part of the fiber image. It does not make sense to determine the retardance in these pixels. To address this issue we programmed an 'Edge Detection Algorithm' that locates the upper and lower boundaries of the fiber in the image. This allows determining the analyser angle θ_{Amin} corresponding to the minimum intensity only for those camera pixels that image the fiber.

The background intensity is not homogenous.

For every pixel in the background image in Figure 6-3(b) extinction occurs for a different analyser angle θ_{Amin} as explained in Chapter 4.. Therefore we also determine the full-field retardance profile of the polarizing microscope without fiber sample, using the same measurement method as described in Chapter 4. By doing so we

obtain the retardance of the background and we can correct for this.

When we have gathered the collection of the fiber images in the range θ_{ATot}, we apply a polynomial fit of the measured intensities to determine the minimum intensity in an accurate manner. Effective fitting requires determining the degree of the polynomial fit L and the number of measured data points taken into consideration. We determined the polynomial fit according to Akaike's information criterion [10, 11], and we took $L = 4$. Increasing the axial stress increases the retardance in the fiber and the angular range of the analyser θ_{ATot} has to be adapted accordingly to obtain extinction for every pixel. In our measurement method the same range is used for every pixel; this means that we obtain asymmetric intensity profiles for some pixels in the field of view, which causes the polynomial fit to be inaccurate.

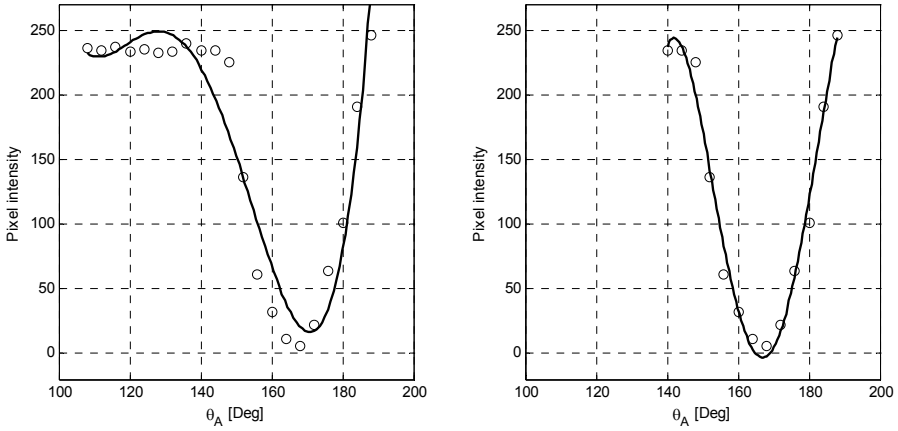

Figure 6-4: Polynomial fitting of the measured intensity profile for one pixel. The left graph is the result of the polynomial fit for all the datapoints in the range of the analyzer θ_{Atot} . The graph on the right side represents the polynomial fit for 13 datapoints around the measured minimum. The polynomial fit degree L is 4.

To cope with this problem we considered 2/3 of the whole amount of collected datapoints around the measured minimum intensity for the

measurements of R(y) and we determined the polynomial fit using only these datapoints [12]. The fraction 2/3 gives us the lowest variance of the minimum intensity computed with the five independent intensity measurements. The estimated value of θ_{Amin} becomes more accurate as illustrated in Figure 6-4. Once we have determined the analyser angle θ_{Amin} that corresponds to the minimum intensity in each pixel under consideration, we proceed to the next step, i.e. determining the full-field retardance.

6.4 Calculation of the retardance

To obtain the retardance profile, we have to apply equation (4.9). We recall this expression here for the sake of clarity (equation (6.2)).

$$R(y) = \frac{\theta_{A\min}}{180}\lambda \tag{6.2}$$

Note that each measurement is repeated five times and hence the resulting retardance profile is the average of the five measurements. The standard deviation of the retardance measurement is below 1 nm. The combination of the polynomial fit and the average of five measurements leads to measurements with reduced variance. This allows dealing with measurement noise. Averaging over more measurements does not decrease the variance of R(y). Finally, the retardance of the background (see previous section) is then subtracted from that result to obtain the final retardance profile of the fiber. The pictures in the left column of Figure 6-5 (a) to (c) depicts the retardance map measured for the three fibers under test for a tensile stress of 115 MPa for fiber 1 and 105 MPa for fibers 2 and 3. The maximum retardance is, respectively, -48.10 nm, -48.29 nm and -52.05 nm. These values correspond approximatively to 1/13-th of the wavelength (λ = 633 nm), which agrees well with values found in the literature for a tensile stress of the same magnitude [13].

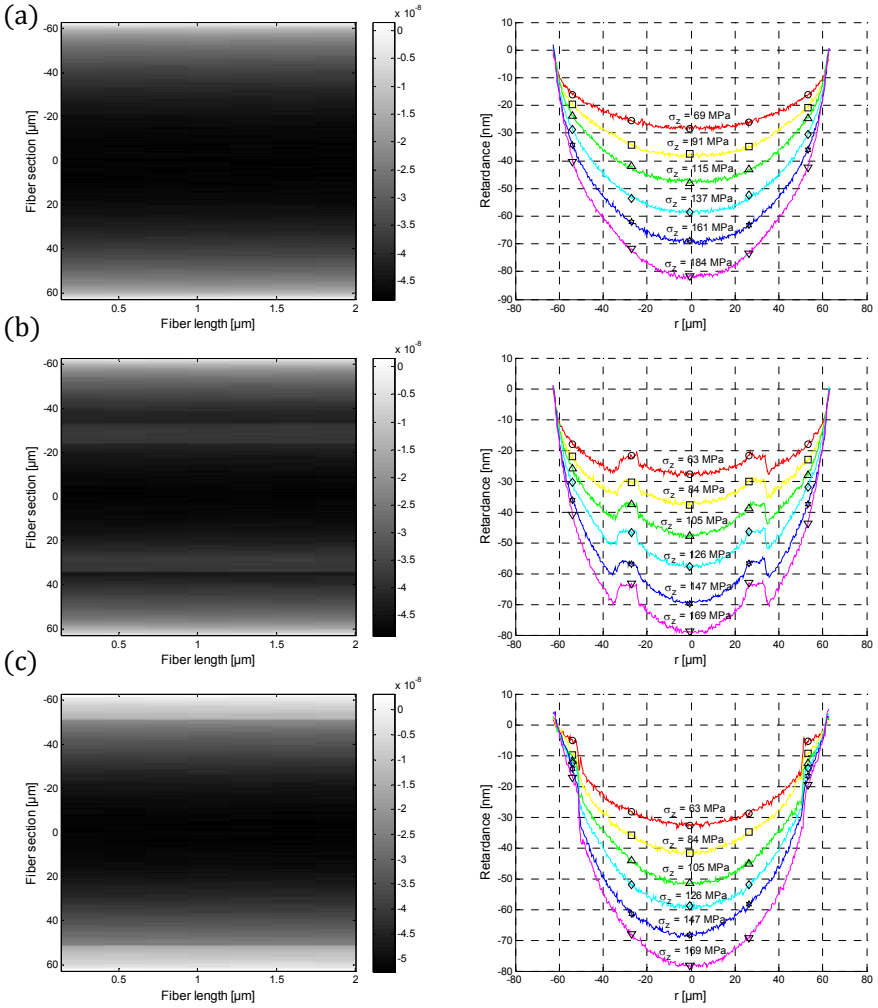

Figure 6-5: Left column: retardance maps measured for the 3 fibers under test for one value of the tensile stress. The scale is in meters. Right column: retardance across the fiber for increasing axial stress. Each profile is computed as an average of five independent measurements. (a) R(y) measured on fiber 1, (b) R(y) measured on fiber 2, (c) R(y) measured on fiber 3.

The graphs in the right column of Figure 6-5 show the retardance profiles for increasing tensile stress in respectively fiber 1, fiber 2 and fiber 3. The shapes of R(y) measured in fiber 1 and fiber 3 are close to a semi-ellipse. This is obviously not the case for the retardance profile of fiber 2. The particular shape of the retardance profile confirms that fiber 2 is a dual clad fiber with depressed inner cladding as we mentioned in section 6.1.

The difference in refractive index between core and cladding for glass fibers 2 and 3 is four times larger compared to fiber 1. This increases the refraction at the boundaries between the two materials and increases the noise on the measured retardance R(y). The average standard deviation of the retardance measurements is small for fiber 1 ($\sigma_1 < 0.5$ nm). For fiber 2 and fiber 3, σ_2 and σ_3 are slightly higher ($0.5 \text{ nm} < \sigma_{2,3} < 1$ nm) as a consequence of the sharper core/cladding transitions. These values will allow us to make a correct choice of the parameters involved in the inverse transform algorithm according to the analysis done in Chapter 5. Now that we have measured the retardance profiles in the fibers, we are able to determine the radial profile of the photoelastic coefficient C(r).

6.5 Determination of the mean photoelastic coefficient

We compare two methods for determining the photoelastic coefficient C. First, we estimate the mean photoelastic constant by relying on the simplifying hypothesis that the retardance can be approximated with an elliptical shape. The second method, which we will describe in section 6.6, determines the radial distribution of the photoelastic constant from the actual measured shape of the retardance without any simplification.

To find the mean value of the photoelastic constant we can approximate the retardance with a semi-ellipse E(y) as described in Chapter 5. Since the inverse Abel transform of E(y) is a constant, as given by equation (5.2), the relation between the axial stress and the retardance becomes (equation (6.3)) :

$$\sigma_z \times C = -\frac{1}{2}\frac{\max(abs(R(y)))}{b} \tag{6.3}$$

where b is the fiber radius, R(y) the measured retardance and σ_z the axial stress. C is the regression coefficient that has to be determined. Note that as a consequence of the particular index profile of fiber 2, the retardance profile over the entire cross-section is not elliptical and hence the elliptical approximation cannot be applied to that particular fiber. The graphs of the product $\sigma_z \times C$ as a function of the applied stress for fiber 1 and fiber 3 are drawn in Figure 6-6.

Using the elliptical approximation we obtain C values of -3.71×10^{-12} Pa^{-1} and -3.74×10^{-12} Pa^{-1} for the silica glass fibers 1 and 3. These values are slightly larger in magnitude than the value measured on bulk fused silica ($C = -3.52\times10^{-12}$ $Pa^{-1} \pm 2\%$) determined in [14]. Our finding is in agreement with the conclusions of [1, 3], i.e. that the absolute value of the photoelastic constant of optical fiber glass is larger than that of bulk silica.

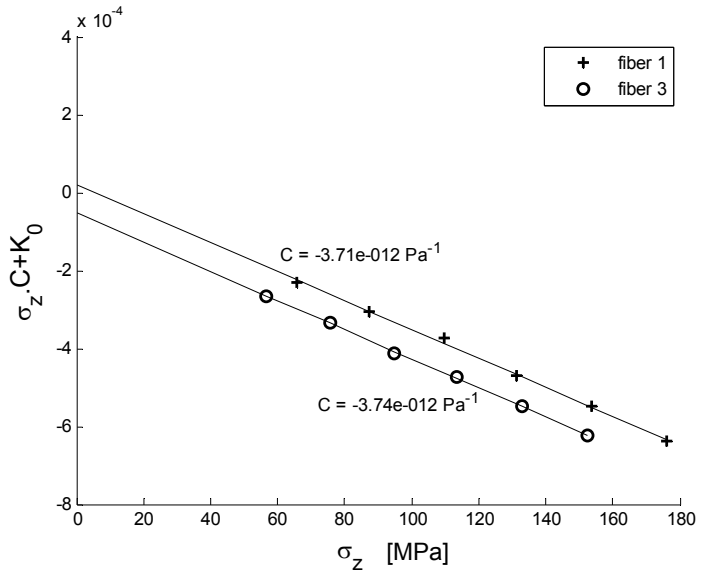

Figure 6-6: . $\sigma_z \times C + K_0$ as a function of the axial stress. The regression coefficient is the photoelastic constant C. K_0 is the residual birefringence. The values of C are indicated in the graph along the respective linear fit. The coefficients of determination of the linear regression for fiber 1 and fiber 3 are respectively $r^2 = 0.999$ and $r^2 = 0.970$.

We can also determine the residual birefringence K_0 in the fiber. It is given by the intersection of the fitted line $\sigma_z \times C$ with the y-axis in the graph of Figure 6-6. K_0 is smaller than 1×10^{-5}. This is of the same order of magnitude as the maximum deviation between the fitted curve and the measurement points. For regular single mode fibers, this value is typically lower. In [12], for example, the authors measured a value of 2.7×10^{-7} on a commercially available single mode fiber. Such low birefringence value means that the associated retardance is very small as well. We mentioned in Chapter 4 that we opted for the Sénarmont compensation method for measuring the retardance and that other methods such as Brace-Köhler or two waveplate compensation would be more adequate for accurately measuring small retardance values. The obtained residual birefringence of 1×10^{-5} illustrates this and we can conclude indeed that our measurement method is not convenient to measure very small retardance values. We can nevertheless estimate the impact of the uncertainty on small retardance values and on K_0 in particular. To do so we carry out the same linear regression but now by considering one fixed additional point at $K_0 = 2.7\times10^{-7}$ for $\sigma_z = 0$ MPa. The linear regression yields $C = -3.77\times10^{-12}$ Pa^{-1} in Fiber 1 instead of the original value of -3.71×10^{-12} Pa^{-1}, which means a deviation of about 6%, which is acceptable. We can therefore still conclude that our measurement method is sufficiently reliable to determine the photoelastic coefficient in silica optical fibers.

6.6 Determination of the radial distribution of the photoelastic coefficient C(r)

In this section, we determine the radial profile C(r) without any simplification. To do so we compute the inverse Abel transform of each measured retardance profile corresponding to a specific tensile stress. We apply 'Algo 1' and 'Algo 2' described in previous Chapters to determine the inverse Abel transform of the retardance profiles. This allows obtaining the relationship $f(r) = \sigma_z \times C(r)$. Calculating the linear regression of $f(r)$ for every point along the radius r finally yields the radial distribution of the photoelastic constant C(r).

We recall that we have to determine the parameter k for our calculations. As we have explained in Chapter 5, the shape of the retardance does not match exactly with that of a semi-ellipse. It is obviously not the case at all for fiber 2 (see Figure 6-5). We therefore have to analyse and compare the profiles obtained for several values of k and decide which value of k gives us the best and most reliable result.

To do so we implemented a process to support an objective decision on the best value for k. First we choose an interval of k around the best value of k as determined in our evaluation of the inverse Abel transform algorithms in Chapter 5. Based on the standard deviation of the retardance profiles and the simulation results on noisy profiles from Chapter 5, we decide to limit our analysis for k in the interval $k \in [1,50]$. For each value of k in that interval we compute the radial profile $C_k(r)$ with 'algo 1' and 'algo 2'. A visual analysis of the profiles $C_k(r)$ leads us to the conclusion that $C(r)$ can be considered constant in the undoped silica portions of the fibers. Therefore we compute the mean standard deviation of $C_k(r)$ in these portions.

Figure 6-7 shows the mean standard deviation $\sigma_1(C(r))$, $\sigma_2(C(r))$ and $\sigma_3(C(r))$ as a function of the parameter k for the three fibers in the undoped silica portions of the fibers according to the method mentioned above. When evaluating the algorithms on the noisy ellipse, 'algo 1' requires a higher amount of Fourier coefficients to converge, which is in line with our conclusions of Chapter 5. Also, the standard deviation does no longer increase at higher values of k. These results agree with those for the noisy ellipse. We do not select blindly that value of k that minimizes the standard deviation of Figure 6-7. Additionally we analyse the shape of $C(r)$ in a small interval of k around that value minimizing the standard deviation to find the amount of Fourier coefficients that decrease the presence of mathematical artefacts in the profile.

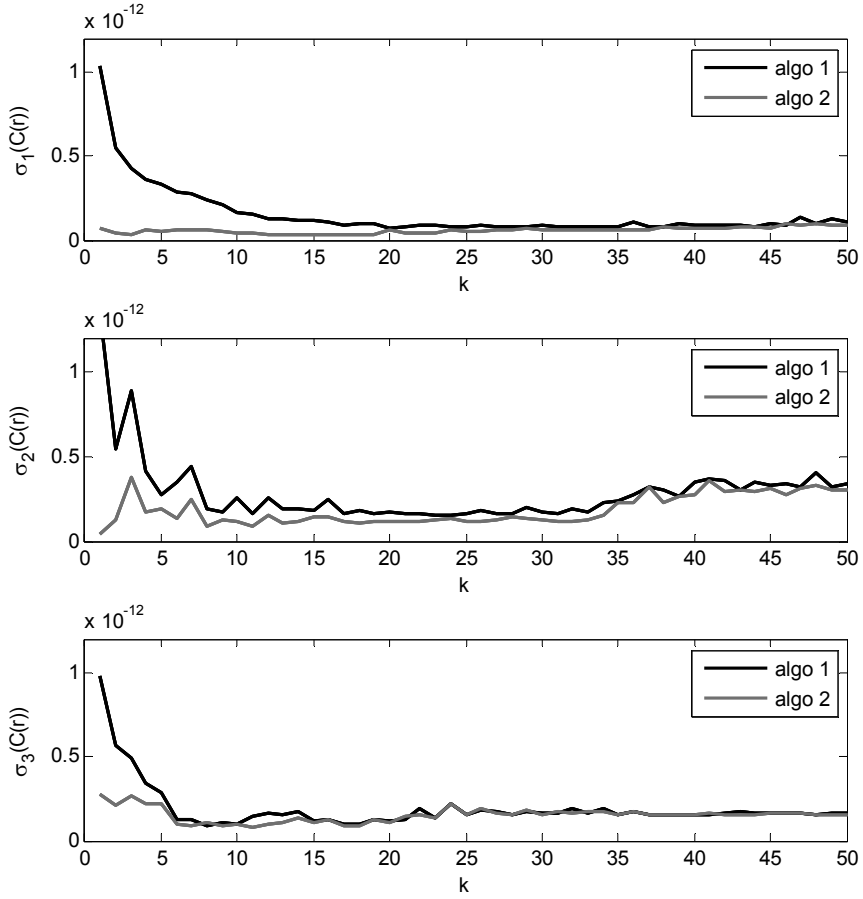

Figure 6-7: Standard deviation $\sigma_1(C(r))$, $\sigma_2(C(r))$ and $\sigma_3(C(r))$ computed for $C_k(r)$ in the undoped silica portions of respectively fiber 1, fiber 2 and fiber 3 for $k \in [1,50]$. $C_k(r)$ is computed with both 'algo 1' and 'algo 2'.

Fiber 1

The shape of R(y) is very close to a semi-ellipse. The evolution of the standard deviation $\sigma_1(C(r))$ is very similar to that obtained with the noisy ellipse for both algorithms. We therefore chose k in accordance with the results of Chapter 5 on the noisy ellipse, i.e. around 30 for 'algo 1' and small, i.e. 10 for 'algo 2'

Fiber 2

R(y) is not elliptical. We take the parameter k in the interval corresponding to a stable portion of the evolution of $\sigma_2(C(r))$ for both algorithms, i.e. $k \in [20,45]$. With these rather high amounts of Fourier coefficients we make sure not to filter out potential abrupt changes of C(r). Furthermore, we choose the value of k from that interval that minimizes the variance in the portions of fiber 2 made of the same material, i.e. in the undoped silica portions.

Fiber 3

R(y) follows an elliptical profile except at the extremities. Based on a similar reasoning as for fiber 2, we first choose $k \in [15,35]$. Next we also determine the value of k in that interval that minimizes the variance in the undoped silica portion of the fiber.

The reasoning above enables us to fix the final values of the parameter k to compute the inverse Abel transform with 'algo 1' and 'algo 2' respectively. The values of k used in the remainder of this Chapter for the three silica fibers are given in Table 6-2.

	Fiber 1	**Fiber 2**	**Fiber 3**
'algo 1'	30	40	30
'algo 2'	10	20	25

Table 6-2: The number of Fourier coefficients k considered to compute the inverse Abel transform with respectively 'algo 1' and 'algo 2'.

The result of the inverse Abel transform of R(y) for increasing tensile load is depicted in Figure 6-8 for the three silica fibers. The graphs in the left column are the result obtained with 'algo 1' while the graphs to the right depict the results achieved with 'algo 2'. The absolute value of the product $\sigma_z \times C(r)$ increases with the load. As one could expect and due to numerical artefacts, the inverse Abel transform produces overshoots in the center of the fiber ($r < 7$ μm) and hence one should disregard the results in that area. The difference in refractive index between core and cladding for glass fibers 2 and 3 is four times larger compared to fiber 1 (cfr Table 6-1). This increases the scattering at the boundaries between the two materials and increases the noise on the measured retardance R(y). As a consequence the inverse Abel transform profiles of fiber 2 and fiber 3 exhibit increasing perturbations at these locations.

At this point we can work out the linear regression of the inverse Abel transform of the retardance, $f(r) = \sigma_z \times C(r)$. As the regression coefficient is the photoelastic constant, we finally obtain the radial distribution of the photoelastic constant C(r). Figure 6-9 shows the radial profiles of the photoelastic constant for the three different glass optical fibers. The standard deviation of the retardance measured for fiber 1 is small, below 1 nm. We obtain similar radial profiles of the photoelastic coefficients of the fiber and these results confirm that both algorithms behave equivalently for profiles with a low noise level.

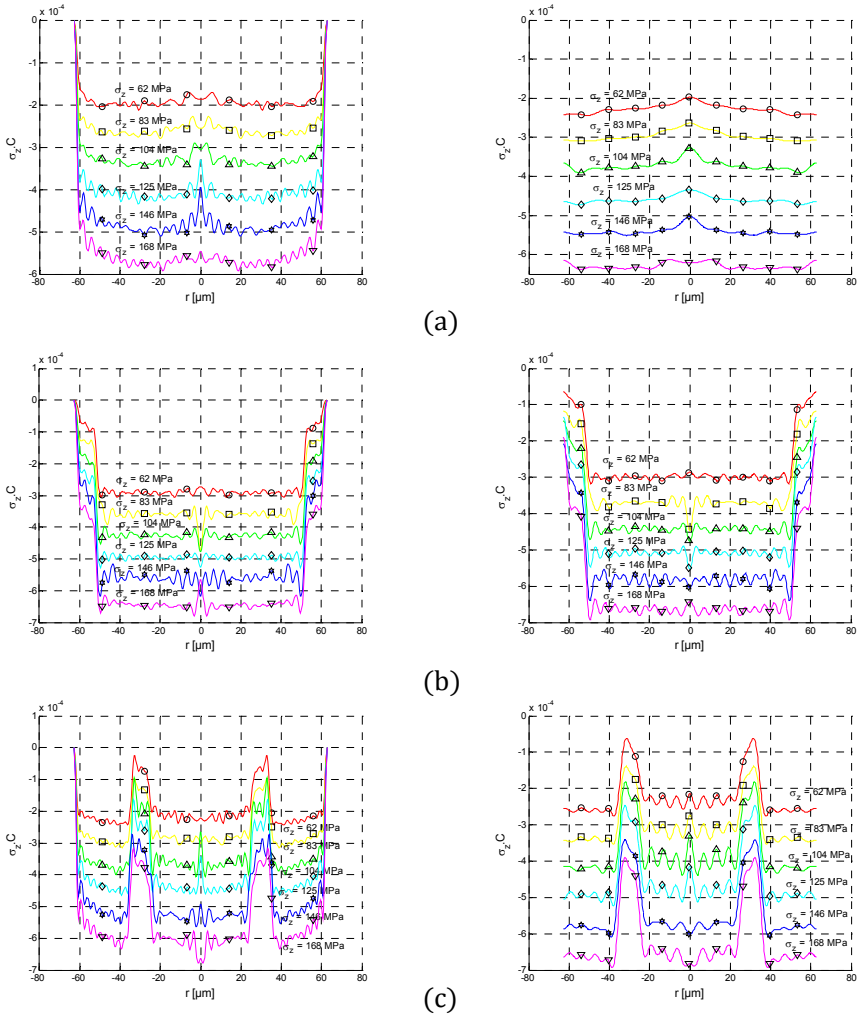

Figure 6-8: Radial distribution of the product $\sigma_z \times C(r)$ in a portion of the fibers as a function of increasing load. Left column: $\sigma_z \times C(r)$ computed with 'algo 1'. Right column: $\sigma_z \times C(r)$ computed with 'algo 2'. (a) $\sigma_z \times C(r)$ in fiber 1; (b) $\sigma_z \times C(r)$ in fiber 2, (c) $\sigma_z \times C(r)$ in fiber 3

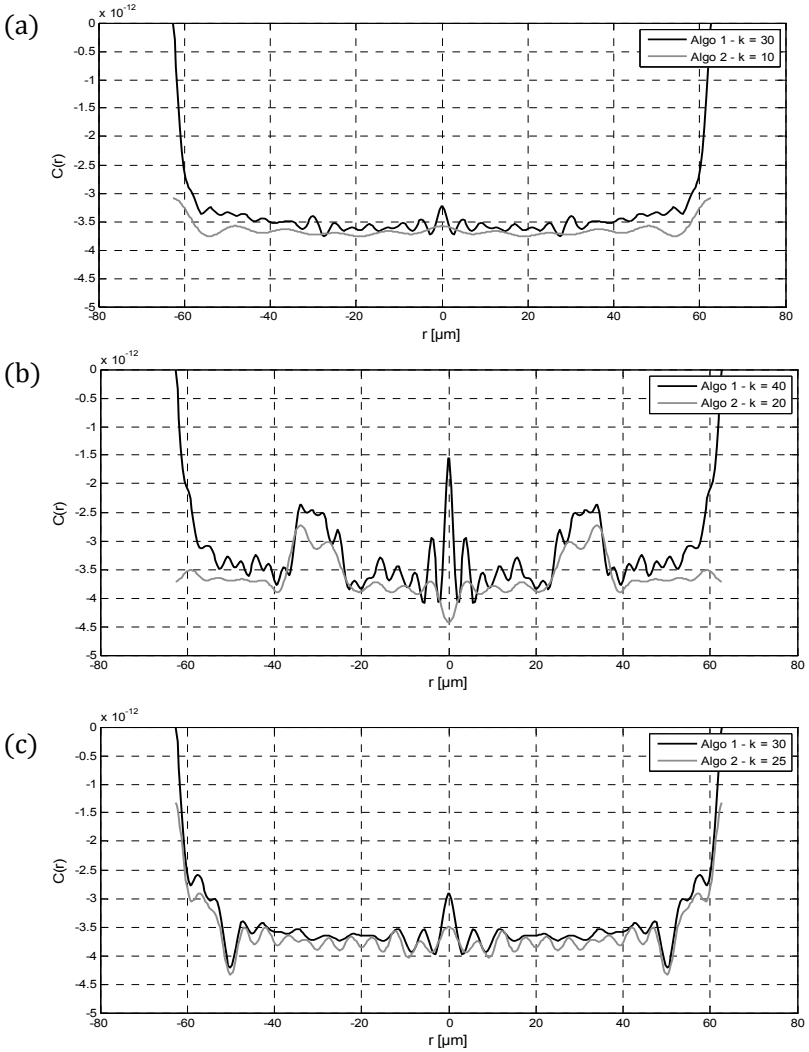

Figure 6-9: Radial distribution of the photoelastic constant C(r) in one fiber section. The profiles are respectively computed with 'algo 1' and 'algo 2'. (a) C(r) in fiber 1, (b) C(r) in fiber 2 and (c) C(r) in fiber 3. The values of k used are mentioned in the graphs as well.

In agreement with the conclusions of Chapter 5, the first algorithm requires a higher number of Fourier coefficients k to achieve a correct profile at the expense of increasing the impact of the measurement noise, which is inherent to the Fourier algorithm. For the second algorithm less Fourier coefficients are needed to achieve a reliable and stable result. The Ge-doped core of fiber 1 does not influence the profile of C(r) and we can conclude from Figure 6-9 (a) that C(r) can be considered constant throughout the cross-section of this fiber. On the other hand, Figure 6-9 (b) and (c) evidence that the value of C(r) in the fluorine-doped cladding portion differs significantly from the value of C(r) in the undoped core of fiber 2 and 3 and from the outer cladding of fiber 2.

We also compute the average value of C(r) in the stable parts of the radial profiles and we obtain respectively -3.73×10^{-12} Pa^{-1}, -3.75×10^{-12} Pa^{-1} and -3.80×10^{-12} Pa^{-1} for glass fiber 1 and for the undoped portions of fibers 2 and 3. The error on C equals approximatively 5%. These figures are comparable with the mean values of the photoelastic constant that we have determined with the elliptical approximation. However, the mean value of C(r) equals -2.75×10^{-12} Pa^{-1} in the fluorinated trenches of the cladding.

To the best of our knowledge this is the first demonstration that one cannot assume the photoelastic coefficient to be constant throughout the fiber section for certain types of fibers.

Our results show that the fluorine doping decreases the absolute value of C with about 27% compared to pure silica or Ge-doped silica glass fibers. Table 6-3 summarizes the values we obtain for the photoelastic coefficients with both methods.

With respect to the radial distribution of C(r), we conclude that the photoelastic coefficient can be considered constant throughout the fiber section for silica fibers that only include a Ge-doped core. The absolute value of the average of C(r) computed in these parts confirms our findings with the elliptical approximation, i.e. the photoelastic coefficient in silica fibers is slightly higher than in bulk silica.

	Fiber 1	Fiber 2		Fiber 3	
	(Ge) Si	*Undoped Si*	*Fluorinated Si*	*Undoped Si*	*Fluorinated Si*
Elliptical approximation [$\times 10^{-12}$ MPa^{-1}]	-3.71	-	-	-3.74	-
Average C(r) [$\times 10^{-12}$ MPa^{-1}]	-3.83	-3.75	-2.75	-3.80	-2.75

Table 6-3: Summary of the results for the photoelastic constant measured on the three silica fibers. Comparison of the values obtained with the elliptical approximation and the average values in the stable parts of the radial profile C(r).

On the contrary, the hypothesis that C(r) is constant throughout the fiber section does not hold in silica glass fibers containing a fluorine-doped depressed cladding.

6.7 Summary and conclusion

The goal of this Chapter was to validate our measurement method and our algorithms to determine the radial profile of the photoelastic coefficient based on actual measurements on glass optical fibers. We measured three commercially available fibers with increasing core diameter.

First, we described the mechanical system used to apply tensile stress to the fiber under test in the polarizing microscope arrangement. We measured the retardance with the Sénarmont compensation technique for increasing tensile stress. To accurately determine the analyzer angle that corresponds to the minimum intensity in a particular pixel of the fiber image we have to use a polynomial fit of the intensity profiles.

Second, we determined the value of the photoelastic coefficient using two methods. Using an elliptical approximation of the retardance profile for fiber 1 and fiber 3 we found a mean value of C to be respectively -3.71×10^{-12} Pa^{-1} and -3.74×10^{-12} Pa^{-1}, close to the values found in the literature. We also determined the radial distribution of C(r) in the fibers using both algorithms. The mean value of C determined with the elliptical approximation and the average value of C(r) in the stable parts of the

profiles are equivalent. This essentially validates our technique and confirms that the absolute value of C is larger in an optical fiber than in bulk silica. For silica glass fibers the mean value of C computed for the three fibers under test equals -3.78×10^{-12} Pa^{-1} in the undoped and Ge-doped portions of the cross-sections. The average value of C in the fluorine-doped part of the cladding region is 27% smaller.

Therefore and with respect to the radial distribution of C(r), we conclude that the photoelastic coefficient can be considered constant throughout the fiber section for silica fibers that only include a Ge-doped core. This is no longer the case in silica glass fibers containing a fluorine-doped depressed cladding. We can most likely extend this conclusion to other optical fibers that possess more complex doping profiles.

Bibliography

[1] A. J. Barlow and D. N. Payne, "The stress-optic effect in optical fibers," *IEEE J. Quantum Electron.*, vol. QE-19, no. 5, pp. 834–839, 1983.

[2] N. Lagakos and R. Mohr, "Stress optic coefficient and stress profile in optical fibers," *Appl. Opt.*, vol. 20, no. 13, pp. 2309–2313, 1981.

[3] A. Bertholds and B. Dändliker, "Determination of the individual strain-optic coefficients in single-mode optical fibers," *J. Light. Technol.*, vol. 6, no. n°1, pp. 17–20, 1988.

[4] "www.thorlabs.de." .

[5] J. W. Fleming and D. L. Wood, "Refractive index dispersion and related properties in fluorine doped silica.," *Appl. Opt.*, vol. 22, p. 3102, 1983.

[6] "http://fiberguide.com/wp-content/uploads/2013/03/All_Silica_Fiber_0301131.pdf." .

[7] T. Z. N. Sokkar, W. A. Ramadan, M. A. Shams El-Din, H. H. Wahba, and S. S. Aboleneen, "Bent induced refractive index profile variation and mode field distribution of step-index multimode optical fiber," *Opt. Lasers Eng.*, vol. 53, pp. 133–141, 2014.

[8] F.-W. Sheu and H.-J. Jhang, "Capturing a reflective cross-sectional image of an optical fiber with partially coherent laser light to measure the refractive index profile of a multimode optical fiber," *Opt. Express*, vol. 21, no. 2, p. 2408, 2013.

[9] "http://www.thorlabs.de/Thorcat/12600/SM600-SpecSheet.pdf." .

[10] Hamparsum and Bozdogan, "Akaike's information criterion and recent developments in information complexity," *J. Math. Psychol.*, no. 44, pp. 62–91, 2000.

[11] G. Damien, "http://www.biomecardio.com/matlab/polydeg.html." .

[12] S. Acheroy, P. Merken, T. Geernaert, H. Ottevaere, H. Thienpont, and F. Berghmans, "Algorithms for determining the radial profile of the photoelastic coefficient in glass and polymer optical fibers," *Opt. Express*, vol. 23, no. 15, p. 18943, 2015.

[13] M. C. Szczurowski, T. Martynkien, G. Statkiewicz-Barabach, L. Khan, D. J.

Webb, C. Ye, J. Dulieu-Barton, and W. Urbanzyck, “Measurements of stress-optic coefficient and Young’s modulus in PMMA fibers drawn under different conditions,” in *SPIE Photonic Crystal Fibers IV Vol 7714* , pp. 1–8, 2010.

[14] W. Primak, “Photoelastic constants of vitreous Silica and its elastic coefficient of refractive index,” *J. Appl. Phys.*, vol. 30, no. 5, pp. 779–788, 1959.

[15] S. Acheroy, P. Merken, H. Ottevaere, T. Geernaert, H. Thienpont, and F. Berghmans, “Influence of measurement noise on the determination of the radial profile of the photoelastic coefficient in step-index optical fibers.,” *Appl. Opt.*, vol. 52, no. 35, pp. 8451–9, 2013.

[16] S. Acheroy, M. Patrick, G. Thomas, H. Ottevaere, H. Thienpont, and F. Berghmans, “On a possible method to measure the radial profile of the photoelastic constant in step-index optical fiber,” in *SPIE: Optical Sensing and Detection III*, 9141, p. 914115, 2014.

[17] S. Acheroy, P. Merken, T. Geernaert, H. Ottevaere, H. Thienpont, and F. Berghmans, “Algorithms for determining the radial profile of the photoelastic coefficient in glass and polymer optical fibers,” *Opt. Express*, vol. 23, no. 15, p. 18943, 2015.

[18] S. Acheroy, P. Merken, T. Geernaert, H. Ottevaere, H. Thienpont, and F. Berghmans, “Inverse Abel transform algorithms to determine the radial profile of the photoelastic coefficient of glass optical fibers,” in *Optical Sensing an Detection IV*, 9899, UNSP 98992F, 2016.

Chapter 7. Photoelastic coefficient in polymer optical fibers

Following the measurements on silica fibers dealt with in the previous chapter, we now turn to the characterization of the photoelastic coefficient in polymer optical fibers (POFs). The fibers under test are essentially composed of polymethyl methacrylate (PMMA). We characterized five POFs that have been produced using a regular fiber drawing process and one POF fabricated using an extrusion process. The first section recalls some of the peculiarities of POFs in view of their potential application in optical fiber based sensors. It also summarizes the main characteristics of the fibers that we have experimented with. We also pay particular attention to the thermal annealing treatment that the fibers have received, as this appears to have a major influence on our measurements. In section 7.2 we present the results of the retardance measurement on the polymer fibers. Section 7.3 deals with the mean value of the photoelastic coefficient C that we have computed using the elliptical approximation. We also analyze the impact of the annealing process on C. Finally we look into the radial profile of the photoelastic coefficient in both pristine and annealed fiber samples in section 7.4. We summarize and conclude on our findings in section 7.5.

7.1 Characteristics of the polymer fibers under test

7.1.1 Particular aspects of polymer optical fiber sensors

Polymer optical fiber based sensors have emerged in the last decade [1]. In addition to the regular advantages of silica optical fiber based sensors, POF sensors provide for a higher elastic strain limit and better fracture toughness, they are more flexible and they can also be made biocompatible. As polymer fibers are more flexible and mechanically compliant, they are more adequate for monitoring deformations in flexible material compared

to silica fibers [2]. Furthermore, polymers are organic materials and hence their composition can be modified with different organic chemistry techniques to provide sensitivities to specific chemical or biological agents [1, 3]. For example, in [4], the authors have proposed multi-antibody biosensing with TOPAS® [5] microstructured polymer optical fibers (MPOF).

Given the long list of advantages, the development of specialty POF based sensors has become a hot research topic. However, working with polymers instead of glass also brings additional challenges. They respond in a different manner to thermal treatments compared to their glass counterparts, they display visco-elastic behavior and they have other photosensitivity characteristics than glass, which makes the fabrication of stable fiber Bragg gratings in such fibers less straightforward than in silica fibers. Furthermore, slight changes in polymer composition and differences in starting material can lead to optical fibers with different characteristics [6, 7]. When dealing with mechanical sensors, this can lead to a major challenge for the design of specialty polymer fiber sensors, i.e. the lack of accurate knowledge of the fiber material parameters and the dependence of these parameters on the thermal treatment history of the fibers. This also pertains to the photoelastic constant, which is the material parameter on which we focus in this thesis.

To set the scene we take a look at values of the photoelastic constant of polymethyl methacrylate (PMMA), which is the most popular base material to fabricate POF. These values have been measured, for example, using PMMA plates and thin films [8, 9]. Reported values of C measured on bulk and thin film polymethyl methacrylate (PMMA) range from -1.08×10^{-10} Pa^{-1} to 5.3×10^{-12} $Pa^{-}1$. In [10] the authors demonstrate that the photoelastic constant in PMMA also depends on the presence and concentration of dopants in the polymer. In [11] C has been measured in PMMA fibers and its value has been found to depend on the drawing conditions of the fiber. The values obtained are between 1.5 and 4.5×10^{-12} Pa^{-1}. Note that the authors did not mention the measurement error. These values are disparate and it is difficult to propose one single value that would appear appropriate for precise design purposes. Moreover, the initial birefringence of standard step-index POFs is also found to be dependent on the drawing process and

the dopants included in the primary polymer material [12–15]. These points add to the necessity to measure C for every different type of POF.

7.1.2 Description of the tested polymer fibers

The essential characteristics of the POFs that we have characterized are summarized in Table 7-1. All POFs were made, for the largest part, from PMMA.

	Fiber 1	*Fiber 2*	*Fiber 3*	*Fiber 4*	*Fiber 5*	*Fiber 6*
Diameter [µm]	250	110	133	260	110	210
Draw Tension D_T	NA	<< 1N	<< 1N	<<1N	*	0,5 < D_T < 1N
Draw ratio [mm/mm]	NA	16/0,11	16/0,133	16/0,26	*	11/0,21

* The draw tension and draw ratio for fiber 5 have not been communicated by the manufacturer.

Table 7-1: Main characteristics of the PMMA optical fibers used to measure the retardance and to determine the radial profile of the photoelastic coefficient. NA means Not Applicable.

Fiber 1 is a multimode fiber fabricated with an extrusion process. This large-core fiber is surrounded with a fluorinated cladding. The core/cladding dimension of fiber 1 is 245/250 µm. Fibers 2 to 6 are single mode PMMA fibers manufactured with a thermal drawing process. The fibers labeled Fiber 2 to Fiber 4 are three similar single mode step-index polymer optical fibers, drawn in the same facility with similar drawing conditions [16–18]. The draw tension for all 3 fibers was below 1N. The core and cladding dimensions of the fibers are respectively 10µm/110µm, 10µm/133µm and 12µm/260µm. The core of these fibers is composed of poly-ethyl methacrylate and poly-benzyl methacrylate (PEMA/PBzMA) [19], while the cladding is made of poly-methyl methacrylate (PMMA). Variations in drawing conditions can for example lead to core/cladding ratio differences resulting from fluctuating fluid dynamic responses of the two polymers (PMMA and PEMA/PBzMA), yet the largest part of the fiber consists of PMMA considering the small dimensions of the core. Fiber 2 and Fiber 3 are fabricated from the same preform, whilst fiber 4 was obtained

from a second preform. The preforms were obtained following thermal curing of the polymer. For the first preform the temperature was increased from 45°C to 75°C within 4 days. The second preform was obtained after heating from 36°C to 88°C within 4.5 days until solidification. The preforms were then heat-drawn into optical fibers at respectively 220°C and 225°C.

The fiber labeled Fiber 5 has a PMMA core doped with 5% polystyrene, and a cladding composed of pure PMMA [20, 21]. The core/cladding dimensions of Fiber 5 is 9µm/110µm. Fiber 6 also has a PMMA cladding and a core composed of PMMA doped with 2,4,6-trichlorophenil methacrylate. The preform of Fiber 6 was annealed for 2 weeks at 80°C before the fiber was heat-drawn at 290°C with a draw tension below 1N. The core/cladding dimensions of this fiber is 4µm/210µm.

7.1.3 Annealing the fibers

The drawn optical polymer fibers can be considered structurally anisotropic because of the fiber drawing process. The drawing tension induces an axial stress which preferentially aligns the long polymer chains along the fiber axis [3, 22]. Annealing allows the molecules to relax back towards a more isotropic configuration. Consequently, annealing is considered to mitigate the anisotropic effect in PMMA optical fibers and to relieve the frozen-in stresses created by the drawing process of the optical fiber [23, 24]. Moreover, several authors show that the annealing treatment of PMMA optical fibers enhances their sensing performances. The linear range of the POFFBG sensors is extended and more stable. Additionally, the operation range without hysteresis is expanded and their tensile properties are enhanced [25–27].

These results motivated us to measure the impact of an annealing process on the photoelastic coefficient profile in the POFs. We first determine both the mean value of C and C(r) for the pristine samples, i.e. the unannealed samples. We then anneal the samples for 8 hours at respectively 40°C, 60°C and 80°C and we determine the mean value of C and C(r) following each annealing step. 40°C and 60°C are chosen to evaluate the influence of low annealing temperatures on the C(r) profile in the PMMA POFs. From the publications cited in section 7.1.2 it appears that generally the fibers are annealed at 80°C. Annealing at higher temperatures

destroys the fibers irreversibly. PMMA based POFs are well known to be sensitive to humidity [28–30]. Whilst we could not control the history in terms of exposure to environmental temperature and humidity changes between their fabrication and arrival in our laboratories, we emphasize that in between the annealing steps we carried out in our labs, all fiber samples were stored and measured in a controlled cleanroom with the same temperature (20°C) and relative humidity (50%) and therefore in the same environmental conditions. We note upfront that to ensure that the fibers were uniform along their length, we have carried out measurements on several fiber portions taken from a single fiber length. We obtained similar results in terms of value of C, which confirms the axial uniformity of the measured fibers.

7.2 Determination of the retardance

We use the same tensile loading system described in chapter 6 to apply tensile stress to the POF samples for determining the retardance. The axial stress σ_z ranges from 10 MPa to 60 MPa. These values are much smaller compared to the tensile stress applied to the silica optical fibers (cfr section 6.2). The purpose was to avoid exceeding the elastic limit of the fiber. Exceeding that limit would bring permanent deformation in the fiber. We now configured the polarizing microscope with the 20X objective, instead of the 40X objective used for glass fibers, for two main reasons. First, the working distance of 410 µm with the 40X objective is too short to allow measuring Fiber 1, Fiber 4 and Fiber 6. The working distance of the 20X objective is 2 mm [31], and it allows measuring all the fibers without any problem. Second, the measurements of the polymer fibers are time consuming, as each fiber has to be measured again after each annealing process. The fiber-end is clamped in the tensile loading system setup. This action weakens the extremities of the fibers. We aimed to reduce the duration of each measurement set to avoid the fiber ends to break, as this would force us to carry out the whole measurement set again with a new piece of fiber, whilst we only had a few samples of Fibers 2, 3, 4 and 6. With the 20X objective, an exposure time of 750 µs is sufficient to acquire images with adequate intensities within the whole angular range of the analyzer θ_{Atot}. With the 40X objective, an exposure time of at least 4s is necessary to

record an exploitable set of intensity images in the range θ_{Atot}. This considerably lengthens the measurement time and increases the risk of fiber breakage in each measurement set.

The process and calculations to determine the retardance in the POFs are identical to what is described in chapter 6 for the silica fibers. Since we measure with a new objective, we first determined the background retardance of the polarizing microscope with this new objective but without sample. As explained in the previous chapter, the retardance of the background will be subtracted from the retardance measured on the POFs to obtain the final retardance. Figure 7-1 (a) to (f) compares the retardance obtained with identical tensile stress for the pristine fiber samples and after each annealing step. This evidences the impact of the annealing process on the retardance profile.

The graphs show that the maximum retardance decreases with the annealing temperature for identical tensile stress, indicating a reduction of the birefringence in the fiber. Table 7-2 summarizes the maximum measured retardance for the unannealed fibers and the fibers annealed at 80°C in fractions of the wavelength $\lambda = 633$ nm.

Fiber	Max(R(y)) without annealing (fraction of λ)	Max(R(y)) annealing at 80°C (fraction of λ)
1	$0.36 \times \lambda$	$0.19 \times \lambda$
2	$0.048 \times \lambda$	$0.044 \times \lambda$
3	$0.25 \times \lambda$	$0.17 \times \lambda$
4	$0.27 \times \lambda$	$0.17 \times \lambda$
5	$0.17 \times \lambda$	$0.07 \times \lambda$
6	$0.09 \times \lambda$	$0.055 \times \lambda$

Table 7-2: Maximum value of R(y) of the measured retardance profile on the pristine fibers and after annealing at 80°C for an identical tensile stress σ_z.

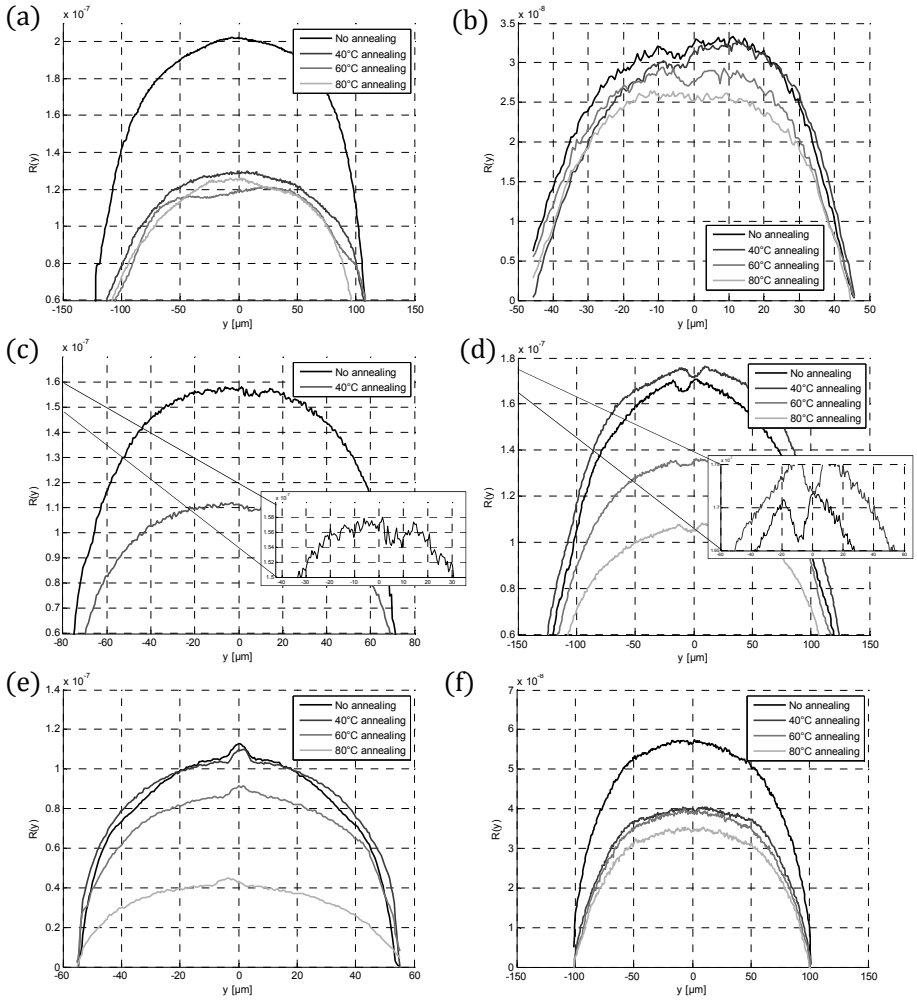

Figure 7-1: Retardance R(y) across the fiber section for increasing annealing temperature with constant tensile stress σ_z . (a) Fiber 1 with $\sigma_z = 24$ MPa, (b) Fiber 2 with $\sigma_z = 13{,}4$ MPa, (c) Fiber 3 with $\sigma_z = 11{,}7$ MPa, the inset shows the portion $R(y) \in [1.7\times10^{-7};1.8\times10^{-7}]$ (d) Fiber 4 with $\sigma_z = 10{,}4$ MPa. The inset shows the portion $R(y) \in [1.65\times10^{-7};1.75\times10^{-7}]$, (e) Fiber 5 with $\sigma_z = 24$ MPa, (f) Fiber 6 with $\sigma_z = 18$ MPa

In addition to decreasing the retardance, annealing also appears to smoothen the shape of the retardance profile, except for the extruded multimode Fiber 1. Fiber 1 did not support the annealing process at 80°C, as every annealed sample was damaged. The quality of the fiber degraded and the axial symmetry disappeared.

The first sample of Fiber 3 degraded after the first annealing process. The shape of the retardance profile did not allow us to draw any conclusion. Therefore, we show the results of the second sample. We did not anneal this fiber at 40°C and 60°C to avoid destroying our last sample of Fiber 3 before annealing at 80°C.

From the measured retardance profiles, we are now able to determine the mean value of the photoelastic coefficient and the radial distribution C(r) and to further analyse the impact of the annealing process on C.

7.3 Determination of the mean photoelastic coefficient

As described in Chapter 6, we first approximate the measured retardance profiles with an elliptical shape to determine the mean value of the photoelastic coefficient. For the sake of clarity, we recall the relation between the axial tensile stress and the measured retardance in the specific case of the elliptical shape approximation (equation (7.1)):

$$\sigma_z \times C = -\frac{1}{2}\frac{\max(abs(R(y)))}{b} \tag{7.1}$$

where b is the fiber radius, R(y) the measured retardance and σ_z the axial stress. C is the regression coefficient that has to be determined. The graphs of the products $\sigma_z \times C$ are shown in Figure 7-2 (a) to (f). As we also did for the silica fibers in chapter 6, we determine the residual birefringence K_0 given by the intersection of the fitted line with the y-axis. Table 7-3 summarizes the values of C and the constant K_0 that we obtained with the six fibers for increasing annealing temperature.

	Annealing Temperature	*Fiber 1*	*Fiber 2*	*Fiber 3*	*Fiber 4*	*Fiber 5*	*Fiber 6*
C [$\times 10^{-12}$ Pa^{-1}]	No	5.40	0.047	-0.93	0.75	-0.15	3.85
	40°C	3.49	0.089	-	0.37	-0.124	4.08
	60°C	4.66	0.218	-	1.11	-0.099	3.83
	80°C	-	1.230	1.50	1.43	1.540	3.94
K_0 [$\times 10^{-4}$]	No	1.51	11	11	6.0	10	2.3
	40°C	1.12	11	-	6.1	9	2.3
	60°C	0.75	10	-	5.8	8	2.3
	80°C	-	7.4	7.2	4.8	6	2.1

Table 7-3: Measured mean photoelastic coefficient C and residual birefringence K_0 measured on POFs at different annealing temperatures.

Note that for the measurements on the POFs the maximum error between the fitted curve and the measurement points is below $1x10^{-5}$, which is approximatively the same magnitude as for the measurements on the silica fibers. Consequently, we can assume that the maximum deviation on K_0 also equals 1×10^{-5}. This corresponds to a maximum error of 10% on the values of K_0 in Table 7-3. We conclude that these values give us a reliable image of the evolution of the residual birefringence in the POFs when they are subjected to an annealing treatment.

Extruded Fiber 1

Analyzing the result on the extruded Fiber 1, annealing does not impact the value of C but reduces the residual birefringence K_0 with 50% after annealing the fiber at 60°C. The annealing steps do not affect the mean value of the photoelastic coefficient and it remains approximatively equal to 4.0×10^{-12} Pa^{-1}. The results are not shown after annealing at 80°C. Since the fiber was damaged after that process, we could not measure any reliable retardance profile and consequently we were not able to calculate the photoelastic constant from R(y).

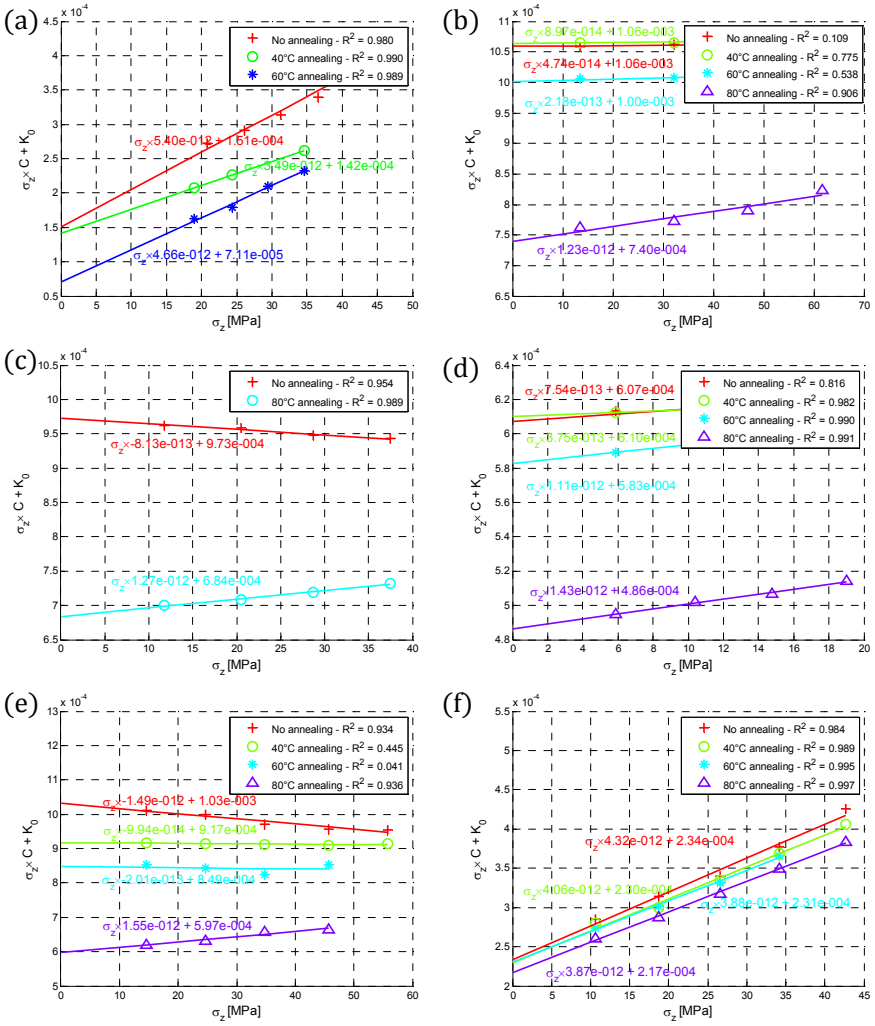

Figure 7-2: $\sigma_z \times C + K_0$ as a function of the axial stress for increasing annealing temperature. The regression coefficient is the mean photoelastic constant C. K_0 is the residual birefringence. The coefficients of determination of each regression are mentioned in the graphs. (a) $\sigma_z \times C + K_0$ in Fiber 1, (b) $\sigma_z \times C + K_0$ in Fiber 2, (c) $\sigma_z \times C + K_0$ in Fiber 3, (d) $\sigma_z \times C + K_0$ in Fiber 4, (e) $\sigma_z \times C + K_0$ in Fiber 5, (f) $\sigma_z \times C + K_0$ in Fiber 6.

Drawn Fibers 2 to 6

Here again, only the results without annealing and with annealing at 80°C are shown for Fiber 3 due to the unsatisfactory measurement results on the first sample. The constant K_0 clearly decreases with increasing annealing temperatures, indicating the decrease of the residual birefringence and hence of the residual stress in these samples. K_0 in the samples annealed at 80°C is consistently lowered by 36% for Fiber 2, Fiber 3 and fiber 5, and by 17% for Fiber 4, compared to the pristine samples.

On the other hand, the annealing process increases the value of the mean photoelastic constant. After annealing at 80°C, the mean value of C tends to reach comparable values between 1.2×10^{-12} Pa^{-1} to 1.6×10^{-12} Pa^{-1} for the three fibers manufactured in the same facility (Fibers 2, 3, 4), as well as for the commercially available Fiber 5. In Fiber 6, which was made from a preform that has been annealed for 2 weeks at 80°C prior to drawing, the decrease of K_0 is less pronounced (7.7%) The mean value of C, which equals $3.9\times10^{-12}Pa^{-1}$, remains almost constant, regardless of the subsequent annealing steps.

7.4 Determination of the radial distribution of the photoelastic coefficient C(r)

We have shown in chapters 5 and 6 that the two algorithms that we use to compute the inverse Abel transform are fully equivalent, with that difference that 'algo 2' converges faster than 'algo 1'. Therefore, we only apply 'algo 2' to compute the inverse Abel transform of the retardance to obtain the radial profile of the photoelastic coefficient in the POFs.

The radial profile C(r) of the pristine fiber samples and these of the samples annealed at 40°C and 60°C are comparable. After annealing at 80°C however, the effect of the higher temperature is clearly visible. Therefore and for the sake of clarity we only compare the C(r) profiles before annealing and after annealing at 80°C in Figure 7-3. We summarize the average value of C(r) computed in the stable parts in Table 7-4.

	Temp	*Fiber 1*	*Fiber 2*	*Fiber 3*	*Fiber 4*	*Fiber 5*	*Fiber 6*
C [$\times 10^{-12}$ Pa^{-1}]	No	5.52	0.003	0.10	0.60	0.07	4.10
	80°C	-	1.33	1.53	1.69	1.83	3.88

Table 7-4: Average value of C(r) computed in the POFs under test without annealing and after annealing at 80°C for 8 hours.

Extruded Fiber 1

As we mentioned before, the radial profile C(r) of Fiber 1 cannot be determined after the annealing process as its quality degrades with the annealing process at a temperature of 80°C. From the graph in Figure 7-3 (a) one can conclude that C(r) is constant throughout the fiber section The average value of C(r) equals $5.52\times10^{-12}Pa^{-1}$, which agrees with the mean value of C determined according the elliptical approximation in section 7.3.

Drawn Fibers 2 to 6

1. **Fibers 2 to Fiber 5**
   The fluctuations of the retardance measurements of fiber 3 and 4 without annealing are slightly higher than in fiber 2. This is illustrated in the insets of the graphs in Figure 7-1 (c) and (d). The retardance profiles of Fiber 3 and 4 are magnified in a portion around the maximum value of R(y) with a scale corresponding to the scale of the retardance profile of Fiber 2. These fluctuations have a direct impact on the calculation and result of the inverse Abel transform of the retardance. Our results nevertheless clearly show the effect of annealing the POFs at a higher temperature. The variance decreases in the 3 fibers, which explains a smoother and more constant C(r) profile throughout the fiber cross-section.

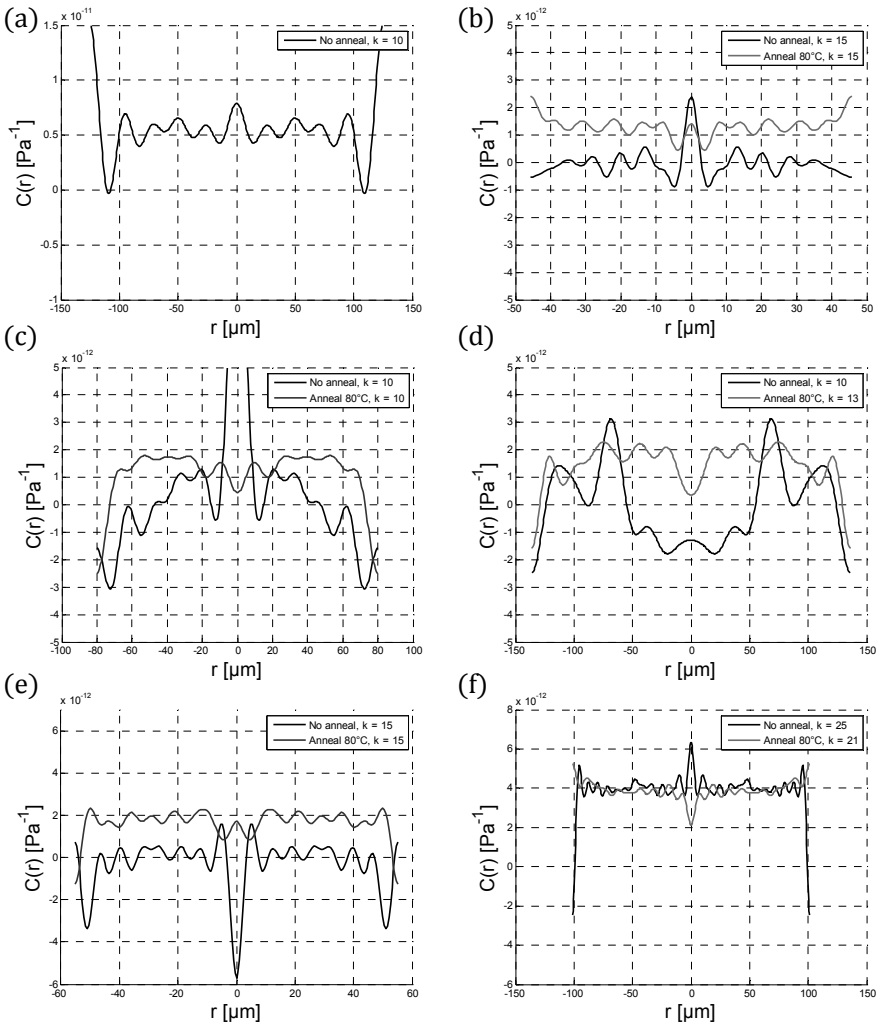

Figure 7-3: Comparison of the radial distribution of the photoelastic coefficient C(r) of the POFs under test without annealing and with 8 hours annealing at 80°C in (a) Fiber 1, (b) Fiber 2, (c) Fiber 3, (d) Fiber 4, (e) Fiber 5 and (f) Fiber 6.

Despite Fiber 5 has been drawn in another independent facility, the measurement results show the same tendency with respect to the evolution of the photoelastic coefficient after the annealing process at 80°C. The shape of C(r) is smoother, indicating a more isotropic behaviour of the fiber, and tends towards the same average value of C(r) of 1.2×10^{-12} Pa^{-1} as shown in Table 7-4. Note that the overshoot at $r = 0$, i.e. in the center of the fibers, stems from a numerical artefact of the inverse Abel transform.
The height of the overshoot depends on the amount of Fourier coefficients considered in the expansion of the inverse Abel transform, as we explained in details in chapter 5, and cannot be related to an actual property of the optical fiber.

2. **Fiber 6**
As shown in the graph of Figure 7-3 (f), the radial profile of C(r) is very stable and its profile is not modified following annealing at 80°C. Annealing has no impact on the average value of C(r) that equals 3.9×10^{-12} Pa^{-1}. Annealing the preform prior to drawing appears to increase the mean value of the drawn fiber and to reduce significantly the residual stress K_0, which is five times smaller compared to the other drawn fibers. On the other hand the higher value of C implies a higher sensitivity of the fiber to stress-induced birefringence. This means that the more the unstressed PMMA fiber is isotropic, the more the stress-induced birefringence is important when the fiber is loaded.

7.5 Summary and conclusion

The aim of this chapter was to measure C(r) in polymer optical fibers and to look into the stability of the photoelastic constant following thermal annealing of the fibers. We characterised one large-core extruded POF and five heat-drawn single mode POFs, of which one has been fabricated from a preform that was thermally annealed prior to drawing.

First, we exposed our motivation to measure the photoelastic coefficient before and after annealing the fiber samples. Annealing has an impact on the retardance profile measured with an identical tensile stress. In all the POFs the retardance decreases, indicating a lower residual stress level in

the annealed fiber samples. Annealing also smoothens the retardance profiles of the drawn POFs, which also indicates a more isotropic nature of the fibers.

Second, we determined the mean photoelastic coefficient of the POFs using the elliptical approximation. C equals 5.4×10^{-12} Pa^{-1} in the extruded fiber, far above the value measured on the heat-drawn fibers with exception of the fiber drawn from a pre-annealed preform. The mean value of C in the latter equals 3.8×10^{-12} Pa^{-1}. Annealing the other heat-drawn POFs for 8 hours at 80°C considerably decreases the value of the residual birefringence K_0 from 17% to 36% on one hand and increases the photoelastic coefficient towards comparable values around 1.2×10^{-12} Pa^{-1}. Note that this may explain the findings reported in [28], i.e. the higher sensitivity to stress and strain, but a lower cross-sensitivity to strain and temperature of an annealed POF. Post-annealing the fiber fabricated from the pre-annealed preform slightly reduces the birefringence, but has no significant impact on the mean value of the photoelastic coefficient.

Third, we determined the radial profile of the photoelastic constant. We can conclude from our results that C(r) in the extruded fiber can be considered constant over the fiber section. The average value of C(r) agrees with the mean value obtained with the elliptical approximation. With exception of the fiber fabricated from the pre-annealed preform, C(r) fluctuates significantly in the unannealed drawn fiber samples. Moreover, its average value is very small, indicating a lower response of the stress-induced birefringence to the applied load. Annealing the fibers for 8 hours at 80°C has definitively a positive effect on C(r). The profile is more regular and constant. The average value of C(r) in all these fibers reaches approximatively 1.2×10^{-12} Pa^{-1}, in agreement with the mean value of C. The annealing process has no impact on the photoelastic coefficient profile of the fiber fabricated from the pre-annealed preform. The radial distribution and the average value of C(r) remain similar compared to the results of the unannealed sample.

We conclude that for drawn PMMA POFs the annealing process of the fiber samples is recommended as it decreases the residual birefringence on one hand, and increases C on the other hand, while making C(r) more uniform across the fiber. Pre-annealing the preform prior to the drawing

process considerably increases the value of C and decreases the anisotropic effects in the PMMA POF. With respect to the profile evolution of C(r) we can conclude that C is constant throughout the fiber section in all the PMMA POFs that we have characterised.

While the order of magnitude of the photoelastic coefficient in silica optical fibers is comparable with the value measured in bulk silica and we measured the same value in different glass fibers, the comparison of C in bulk polymer material and POF is not relevant. Also the value of C in PMMA POFs depends on the annealing history of the fiber. Our results point out that, in contrast to glass fibers, C cannot be approximated by any 'standard' value and that it has to be measured for every POF.

Bibliography

[1] F. Berghmans and H. Thienpont, "Plastic Optical Fibers for Sensing Applications," *OFC*, pp. 3–5, 2014.

[2] S. Kiesel, K. Peters, T. Hassan, and M. Kowalsky, "Behaviour of intrinsic polymer optical fibre sensor for large-strain applications," *Meas. Sci. Technol.*, vol. 18, no. 10, pp. 3144–3154, 2007.

[3] D. J. Webb, "Fibre Bragg grating sensors in polymer optical fibres," *Meas. Sci. Technol.*, vol. 26, no. 92004, 2015.

[4] G. Emiliyanov, P. E. Høiby, L. H. Pedersen, and O. Bang, "Selective serial multi-antibody biosensing with TOPAS microstructured polymer optical fibers," *Sensors (Switzerland)*, vol. 13, no. 3, pp. 3242–3251, 2013.

[5] "TOPAS." [Online]. Available: http://www.topas.com/.

[6] D. J. Webb and K. Kali, "Polymer fiber Bragg gratings," in *Fibre Bragg Grating Sensors: Recent Advancements, Industrial Applications and Market Exploitation*, A. Cusano, A. Cutolo, and J. Albert, Eds. Bentham Science Publishers, pp. 292–212, 2011.

[7] D. J. Webb, "Fibre Bragg grating sensors in polymer optical fibres," *Meas. Sci. Technol.*, vol. 26, no. 9, p. 92004, 2015.

[8] M. Tsukiji, H. Kowa, K. Muraki, N. Umeda, K. Imoto, M. Kanasaki, K. Tahara, K. Morii, and Y. Tajitsu, "Measurement System for Very Small Photoelastic Constant of Polymer Films," *Macromol. Symp.*, vol. 242, no. 1, pp. 235–240, 2006.

[9] T. Kihara, "A Measurement Method for Birefringent Plate using Elliptically Polarized Light," pp. 255–263, 2006.

[10] H. Ohkita, K. Ishibashi, D. Tsurumoto, A. Tagaya, and Y. Koike, "Compensation of the photoelastic birefringence of a polymer by doping with an anisotropic molecule," *Appl. Phys. A*, vol. 81, pp. 617–620, 2005.

[11] M. C. Szczurowski, T. Martynkien, G. Statkiewicz-Barabach, L. Khan, D. J. Webb, C. Ye, J. Dulieu-Barton, and W. Urbanzyck, "Measurements of stress-optic coefficient and Young's modulus in PMMA fibers drawn under different conditions," in *SPIE Photonic Crystal Fibers IV Vol 7714*, pp. 1–8, 2010.

[12] M. G. Kuzyk, *Polymer fiber optics: materials, physics, and applications*. CRC Press, 2006.

[13] S. Iwata, H. Tsukahara, E. Nihei, and Y. Koike, "Transparent zero-birefringence copolymer and its optical properties.," *Appl. Opt.*, vol. 36, no. 19, pp. 4549–55, 1997.

[14] A. Tagaya, L. Lou, Y. Ide, Y. Koike, and Y. Okamoto, "Improvement of the physical properties of poly(methyl methacrylate) by copolymerization with N-pentafluorophenyl maleimide; zero-orientational and photoelastic birefringence polymers with high glass transition temperatures," *Sci. China Chem.*, vol. 55, no. 5, pp. 850–853, 2012.

[15] A. Tagaya, H. Ohkita, T. Harada, K. Ishibashi, and Y. Koike, "Zero-birefringence optical polymers," *Macromolecules*, vol. 39, pp. 3019–3023, 2006.

[16] H. Y. Liu, G. D. Peng, and P. L. Chu, "Polymer fiber Bragg gratings with 28-dB Transmission Rejection," *IEEE Photonics Technol. Lett.*, vol. 14, no. 7, pp. 935–937, 2002.

[17] Y. Luo, B. Yan, M. Li, X. Zhang, W. Wu, Q. Zhang, and G.-D. Peng, "Analysis of multimode POF gratings in stress and strain sensing applications," *Opt. Fiber Technol.*, vol. 17, no. 3, pp. 201–209, 2011.

[18] W. Wu, Y. Luo, X. Cheng, X. Tian, W. Qiu, B. Zhu, G. Peng, and Q. Zhang, "Design and fabrication of single mode polymer optical fiber gratings," vol. 12, no. 8, pp. 1652–1659, 2010.

[19] H. Y. Liu, G. D. Peng, and P. L. Chu, "Thermal tuning of polymer optical fiber Bragg gratings," *IEEE Photonics Technol. Lett.*, vol. 13, no. 8, pp. 824–826, 2001.

[20] "http://www.paradigmoptics.com/." .

[21] C. A. F. Marques, L. B. Birlo, N. J. Alberto, D. J. Webb, and R. N. Nogueira, "Narrow bandwidth Bragg gratings imprinted in polymer optical fibers for different spectral windows," *Opt. Commun.*, vol. 307, pp. 57–61, 2013.

[22] K. Peters, "Polymer optical fiber sensors—a review," *Smart Mater. Struct.*, vol. 20, no. 1, p. 13002, 2011.

[23] W. Zhang and D. J. Webb, “Factors influencing the temperature sensitivity of PMMA based optical fiber Bragg gratings,” Proc. SPIE, vol. 9128, p. 91280M, 2014.

[24] C. Jiang, M. G. Kuzyk, J.-L. Ding, W. E. Johns, and D. J. Welker, “Fabrication and mechanical behavior of dye-doped polymer optical fiber,” *J. Appl. Phys.*, vol. 92, no. 1, pp. 4–12, 2002.

[25] K. E. Carroll, C. Zhang, D. J. Webb, K. Kalli, A. Argyros, and M. C. Large, “Thermal response of Bragg gratings in PMMA microstructured optical fibers.,” *Opt. Express*, vol. 15, no. 14, pp. 8844–8850, 2007.

[26] W. Yuan, A. Stefani, M. Bache, T. Jacobsen, B. Rose, N. Herholdt-Rasmussen, F. K. Nielsen, S. Andresen, O. B. Sørensen, K. S. Hansen, and O. Bang, “Improved thermal and strain performance of annealed polymer optical fiber Bragg gratings,” *Opt. Commun.*, vol. 284, no. 1, pp. 176–182, 2011.

[27] R. Oliveira, C. A. F. Marques, L. Bilro, and R. N. Nogueira, “Production and characterization of Bragg gratings in polymer optical fibers for sensors and optical communications,” *23rd Int. Conf. Opt. Fibre Sensors*, vol. 9157, no. MM, pp. 9–12, 2014.

[28] G. Woyessa, A. Fasano, A. Stefani, C. Markos, K. Nielsen, H. K. Rasmussen, and O. Bang, “Single mode step-index polymer optical fiber for humidity insensitive high temperature fiber Bragg grating sensors,” *Opt. Express*, vol. 24, no. 2, p. 1253, 2016.

[29] G. Woyessa, K. Nielsen, A. Stefani, C. Markos, and O. Bang, “Temperature insensitive hysteresis free highly sensitive polymer optical fiber Bragg grating humidity sensor,” *Opt. Express*, vol. 46, no. 9, pp. 643–644, 2011.

[30] P. Stajanca, O. Cetinkaya, M. Schukar, P. Mergo, D. J. Webb, and K. Krebber, “Molecular alignment relaxation in polymer optical fibers for sensing applications,” *Opt. Fiber Technol.*, vol. 28, pp. 11–17, 2016.

[31] “Zeiss microscope characteristics.” [Online]. Available: https://www.micro-shop.zeiss.com/?s=593107750117ec&l=en&p=us&f=o&a=l&m=s.

Chapter 8. Summary and conclusions

The transduction mechanism exploited in many mechanical optical fiber sensors uses the principles of photoelasticity, which relate an applied mechanical load to stress-induced birefringence in a transparent material. The photoelastic coefficient is the material parameter that characterizes the amount of birefringence created by a given mechanical load. The design of specialty fibers tailored to specific sensor applications requires conducting simulations of the anticipated sensor behavior prior to manufacturing the fibers and sensors made thereof. This calls for accurate knowledge of the material parameters involved, and of the photoelastic constant C in particular. This coefficient C has already been extensively documented for bulk materials, including glass and polymers, from which the optical fibers can be fabricated. However, the particular fabrication of optical fibers and optical fiber sensors involves processing these materials, which is likely to modify the value of C compared to its value in bulk material. Therefore, this photoelastic coefficient, as any other refractive property, should preferably be measured directly on the fiber. Furthermore, the particular structure of an optical fiber may lead to variations of the value of C in its cross-section, and therefore one should also consider the profile C(r) in the fiber cross-section.

This triggered the definition of the grand objective of this PhD, i.e. to develop a method that allows measuring the photoelastic coefficient C and its radial profile directly on both glass and polymer optical fibers. To address this objective, we had to tackle the following challenges;

- to build an experimental setup that allows accurately measuring stress-induced birefringence in an optical fiber submitted to a controlled mechanical load, in such a way that the value of C can be subsequently determined with micron-level spatial resolution in the fiber cross-section;

- to develop effective algorithms that allow calculating the value of C relating the local birefringence values to the applied mechanical load, based on the measured data, with sufficient accuracy, i.e. with a standard deviation value below 10% of the mean value ;

- to validate our method and to apply it to photoelastic coefficient characterizations of both silica and polymer fibers.

8.1 Summary of the results and contributions

The first main achievement of this thesis is the development of the theoretical basis that supports our measurement method to enable determining the radial profile of the photoelastic coefficient of the optical fibers directly on the optical fiber, both for silica and polymer fibers. Our method exploits the stress-induced birefringence in the fibers. First, we showed how the stress-induced projected retardance of a laterally illuminated optical fiber can be used to derive the radial profile of the photoelastic coefficient using an adequate inversion algorithm, known as the inverse Abel transform. We demonstrate that a linear regression in each point along the fiber radius of the inverse Abel transform of the retardance measured for increasing known tensile stress yields the radial distribution of the photoelastic coefficient of the optical fiber. To the best of our knowledge, it is the first time that a full-field measurement approach is developed to determine the photoelastic coefficient of an optical fiber with sub-micron spatial resolution.

The second achievement of our work is the translation of our measurement model into an exploitable measurement setup, which returns measurement data that can be processed using adequate algorithms for computing the inverse Abel transform. The actual measurements rely on the Sénarmont compensation method to characterize the retardance in the laterally illuminated fiber. We developed two algorithms based on Fourier theory to compute the numerical inverse Abel transform of the measured retardance. We tested these algorithms on a known analytical profile to demonstrate their effectiveness and their robustness when dealing with noisy measurement data. This analysis also allowed identifying the optimal set of computational parameters that returns the most effective inverse

Abel transform. Our original contribution is the implementation and detailed analysis of the two Fourier based algorithms to compute the inverse Abel transform. The algorithms and related results can easily be extended to perform the integral inversion of other projected functions, e.g. to compute accurately the residual birefringence in an optical fiber.

The application of our measurement method to determine the radial profile of the photoelastic coefficient in glass fibers forms our third main achievement. We demonstrated that C is slightly higher in silica glass fibers compared to their bulk silica counterpart. This confirms measurement results published in literature. Our measurement results also revealed that C can be considered constant in the cross-section of undoped and in the Ge-doped portions of silica fibers. We measured a mean value of $C = -3.78\times10^{-12}$ Pa^{-1} in these portions of the fibers. However, the value of the photoelastic coefficient changes in fluorinated portions of the glass fibers. The mean value in these locations was 27% lower in absolute value. This is a major achievement of our research work in the sense that we are able to demonstrate that the photoelastic coefficient of an optical fiber is not always constant over the fiber cross-section and consequently we evidenced the added value to measure the radial profile of C of the optical fiber. The results on the silica fibers validate our technique, which was a pre-requisite before experimenting with polymer optical fibers.

This brings us to the fourth and last main achievement of our PhD research. We have shown that the value of C for bulk polymethyl methacrylate (PMMA) and for optical fibers made from such material greatly differs. Furthermore, we have shown that the value of C differs from one PMMA fiber to another. It is the first time, again to the best of our knowledge, that the radial profile of the photoelastic coefficient in polymer optical fiber is determined. We have also evidenced that the thermal history of the polymer fibers has a crucial impact on the value of the photoelastic coefficient and thus on the sensing sensitivity of the polymer fibers. For an extruded polymer optical fiber, annealing - in the same conditions as heat-drawn fibers - deteriorates the fiber samples and therefore does not appear to have any beneficial effect. However, an optical fiber heat-drawn from a preform which received a specific annealing treatment prior to drawing exhibits less residual birefringence, whilst the sensitivity of the fiber to

stress-induced birefringence was significantly higher. The mean value of C equals 3.8×10^{-12} Pa^{-1}, which is more than ten times higher compared to other heat-drawn fibers with no specific annealing treatment of the preform. We have also evidenced that annealing the latter fibers for 8 hours at 80°C has a beneficial effect on C(r). The average value of C(r) in all fibers increases and reaches comparable values around 1.2×10^{-12} Pa^{-1}. Additionally, the residual birefringence decreases and the profile C(r) gets smoother. These findings do not only show that the photoelastic coefficient should be measured for every different polymer optical fiber, but may also explain the reports in open literature on modified sensitivities of polymer optical fiber based sensors following thermal treatment. We can therefore also recommend annealing of drawn polymer fibers prior to their use as mechanical optical sensors.

8.2 Perspectives

The method that we have developed enables characterizing the photoelastic coefficients in a wide variety of regular glass and polymer optical fibers and therefore allows working with the correct value of these coefficients in view of designing tailored optical fiber sensors. Several challenges however remain in order to further increase the accuracy with which the photoelastic properties of optical fibers can be assessed.

First, there is room for improving the experimental setup to determine the retardance, essentially to allow for a higher measurement throughput and to increase the accuracy of the measured retardance. This could be tackled as follows:

- by installing a motorized analyzer synchronized with an automatic frame-grabber. Currently the analyzer is rotated manually and a mouse-click is necessary to take a picture after each rotation of the analyzer. An automated system would accelerate the measurements and most likely improve the accuracy.

- By installing a tensile stress-system with easy and solid fiber end fixations, together with a computer-controlled system to axially stress the fiber.

Second, the results that we have achieved with silica fibers demonstrate that the value of C depends on the usage of dopants in the fiber structure. Therefore, extending our analysis to a systematic study of the influence of the dopant type and concentration on the value of the photoelastic coefficient would be beneficial. Characterizing fibers with well-known specific doping profiles would allow further optimizing our measurement method. This may hypothetically also lead to the development of specialty optical fibers with a tailored mean value or radial profile of C. Another extension of our analysis that would be interesting to address is the study of the wavelength dependence of C.

Third, our results on polymer optical fibers point to the need to conduct a more extended investigation of the impact of annealing or other post-processing of such fibers. For instance, for fibers drawn from a preform with no special thermal pre-treatment, we could examine if annealing for periods longer than 8 hours increases the measured value of the photoelastic coefficient of these fibers. It would allow concluding more firmly on whether C and thus the sensitivity of polymer fiber based sensors converges towards a stable value after a given annealing time. This should also be extended to optical fibers drawn from doped PMMA or from other polymers. Furthermore, it would be of great interest to combine the measurements with organic chemistry analyses of the fiber samples to relate the observed changes in C to the structure of the polymers. Finally, we could also conduct our analysis on polymer fiber samples exposed to UV light in order to assess the influence of fiber Bragg grating inscription on the photoelastic coefficient.

Finally, we look forward to confronting our measurement results with actually simulated and characterized responses of fiber sensors made from both silica and PMMA fibers. An interesting exercise would consist, for example, in looking at responses of PMMA fiber based sensors made from an optical fiber drawn from the same preform that have been exposed to different annealing treatments. From our measurements, we expect that annealing will enhance the sensitivity of the fiber sensors, which would confirm that the value of the photoelastic coefficient increases in annealed PMMA fibers.

8.3 Final statement

We developed a method that enables the characterization of the photoelastic coefficient of any type of optical fiber, provided the fiber is axisymmetric. This photoelastic coefficient is an important quantity that impacts the operation of many optical fiber based sensors. We therefore hope that our characterization work of the photoelastic properties of optical fibers will positively contribute to further developments in the fields of specialty optical fiber and optical fiber sensor design and applications.

Publication list

Publications in Web of Science Core Collection indexed journal papers

[1] S. Acheroy, P. Merken, H. Ottevaere, T. Geernaert, H. Thienpont, and F. Berghmans, "Influence of measurement noise on the determination of the radial profile of the photoelastic coefficient in step-index optical fibers.," Appl. Opt., vol. 52, no. 35, pp. 8451–9, 2013.

[2] S. Acheroy, P. Merken, T. Geernaert, H. Ottevaere, H. Thienpont, and F. Berghmans, "Algorithms for determining the radial profile of the photoelastic coefficient in glass and polymer optical fibers," Opt. Express, vol. 23, no. 15, p. 18943, 2015.

[3] S. Acheroy, P. Merken, H. Ottevaere, T. Geernaert, H. Thienpont, C. A. F. Marques, D. J. Webb, P. Gang-Ding, M. Pawel, and F. Berghmans, "Thermal effects on the photoelastic coefficient of polymer optical fibers," Opt. Lett., vol. 41, no. 11, pp. 2517–2520, 2016.

Publications in conference proceedings

[1] S. Acheroy, M. Patrick, G. Thomas, H. Ottevaere, H. Thienpont, and F. Berghmans, "On a possible method to measure the radial profile of the photoelastic constant in step-index optical fiber," in Optical Sensing and Detection III, Vol. 9141, p. 914115 (Proc SPIE 2014).

[2] S. Acheroy, P. Merken, T. Geernaert, H. Ottevaere, H. Thienpont, and F. Berghmans, "Determination of the radial profile of the photoelastic coefficient of polymer optical fibers," in Micro-Structured and Specialty Optical Fibres IV, Vol. 9886, 7p. 98861K (Proc SPIE 2016).

[3] S. Acheroy, P. Merken, T. Geernaert, H. Ottevaere, H. Thienpont, and F. Berghmans, "Inverse Abel transform algorithms to determine the radial profile of the photoelastic coefficient of glass optical fibers," in Optical Sensing an Detection IV, Vol. 9899, 8 p. UNSP 98992F (Proc SPIE 2016).

[4] S. Acheroy, T. Geernaert, H. Ottevaere, H. Thienpont, D. J. Webb, and C. A. F. Marques, “Determination of the radial profile of the photoelastic coefficient of plastic optical fibers,” in 25th International conference on POF (Aston 2016).